

POLITECNICO DI TORINO

Faculty of Automotive Engineering

Master Thesis

**PREDICTION OF AIRFLOW FOR AUTOMOTIVE COOLING APPLICATIONS**

**USING OPENFOAM**



**Advisor:**

**Renzo Arina**

**Candidate:**

**Sitong Ye**

September 2018

## DECLARATION OF ORIGINALITY

I hereby certify that I am the sole author of this thesis and that no part of this thesis has been published or submitted for publication.

I certify that, to the best of my knowledge, my thesis does not infringe upon anyone's copyright nor violate any proprietary rights and that any ideas, techniques, quotations, or any other material from the work of other people included in my thesis, published or otherwise, are fully acknowledged in accordance with the standard referencing practices. Furthermore, to the extent that I have included copyrighted material that surpasses the bounds of fair dealing within the meaning of the Canada Copyright Act, I certify that I have obtained a written permission from the copyright owner(s) to include such material(s) in my thesis and have included copies of such copyright clearances to my appendix.

I declare that this is a true copy of my thesis, including any final revisions, as approved by my thesis committee and the Graduate Studies office, and that this thesis has not been submitted for a higher degree to any other University or Institution.

## ABSTRACT

This research focuses on studying OpenFOAM's capability of underhood thermal simulations and investigating the performance of various fan modeling techniques in comparison to other commercial software packages.

An isolated fan is modeled in OpenFOAM using Moving Reference Frame (MRF) and Actuator Disk techniques. To evaluate their performances, the simulation results are compared to the experimental data which was provided by a fan testing facility and the available simulation results from Star-CCM+ and ACE+. The pressure rise is the main parameter that is used for comparisons. To further investigate OpenFOAM's capabilities, a full vehicle model using MRF technique is studied and the airflow rate across the radiator from simulation results was compared to experimental data and ACE+.

The simulation results showed that OpenFOAM has a promising performance on solving the pressure rise across an isolated fan using MRF and Actuator Disk Model. Both fan modeling techniques in OpenFOAM gave more accurate results than Star-CCM+ and ACE+, while the Actuator Disk Model predicted the pressure rise more precisely than the MRF model. By modeling the fan using MRF technique in a full vehicle simulation, the predicted airflow rate across the radiator in OpenFOAM was less accurate than ACE+.

## DEDICATION

*To my parents and grandparents  
who have always loved and supported me unconditionally*

## ACKNOWLEDGEMENTS

I would like to express my profound gratitude to my academic advisors Dr. J. Johrendt, Dr. Renzo Arina and Dr. R. Carriveau for their guidance and continuous support throughout this two-year international master program. My sincere thanks also go to my committee members, Dr. R. M. Barron and Dr.D.S-K.Ting, for all the insightful advice and expertise that greatly assisted my research.

This project could not be completed without the immense assistance of my industrial advisor Dr. E. Farbar, who has patiently guided me through the entire project and widened my research from various perspectives. I am deeply grateful for her quick response whenever I am in need. I could not ask for a better advisor. I would also like to sincerely thank Mr. M. Malik and Ms. M. Mills for their support during the whole project and for their tremendous efforts to make this program happen. Besides, special thanks to all my supervisors and colleagues in FCA Canada and Italy, Dr. K. Srinivasan, Mr. M. Gautero, Ms. L. Loreface, Mr. L. Miretti and Mr. N. Paola, for their genuine interests towards my research and their valuable guidance along the way.

I am incredibly grateful to FCA Canada/University of Windsor Automotive Research and Development Centre (ARDC) and Centro Ricerche Fiat (CRF) for generously sharing their computational and industrial resources with me. Special thanks go to Mr. D. JosephShears who has helped me tremendously whenever I have encountered technical problems even when I am 7000 kilometers away! He has always resolved the issues so quickly and patiently!

Finally, I would like to thank all my family members that I owe everything to. They have always loved me and supported me unconditionally and believed me throughout my entire study career.

## TABLE OF CONTENTS

DECLARATION OF ORIGINALITY .....	ii
ABSTRACT.....	iii
DEDICATION.....	iv
ACKNOWLEDGEMENTS.....	v
LIST OF TABLES.....	viii
LIST OF FIGURE.....	ix
NOMENCLATURE .....	xii
CHAPTER 1 INTRODUCTION .....	1
1.1 Background .....	1
1.2 Motivation .....	2
1.3 Scope of Study .....	3
CHAPTER 2 LITERATURE REVIEW .....	4
2.1 Introduction to Fan Modeling .....	4
2.2 Moving Reference Frame.....	6
2.3 Actuator Disk .....	9
2.4 Experimental Setup .....	10
CHAPTER 3 MOVING REFERENCE FRAME .....	12
3.1 Theory .....	12
3.1.1 Governing Equations .....	12
3.1.2 Moving Reference Frame .....	14
3.2 Mesh Generation .....	16
3.2.1 Refinement Settings.....	16
3.2.2 Boundary Layer .....	20
3.3 Boundary Conditions.....	23
3.4 Solver Settings.....	24
3.5 Results & Discussions.....	30
3.5.1 Changing MRF Domain .....	37

3.5.2 Changing Upstream Boundary Condition .....	40
3.5.3 Changing the Upstream Volume .....	42
CHAPTER 4 FULL VEHICLE MODELING .....	45
4.1 Background .....	45
4.2 Heat Exchangers.....	48
4.3 Simulation Settings .....	52
4.2 Results & Discussions .....	55
CHAPTER 5 ACTUATOR DISK MODEL .....	65
5.1 Background .....	65
5.2 Simulation Setup .....	66
5.3 Results & Discussions.....	69
CHAPTER 6 CONCLUSIONS AND FUTURE WORK.....	77
6.1 Conclusions .....	77
6.2 Future Work .....	78
REFERENCES/BIBLIOGRAPHY.....	79
VITA AUCTORIS .....	81

## LIST OF TABLES

Table 3.1: Mesh settings for MRF model .....	18
Table 3.2 Dimensions and mesh sizes of volume refinement objects .....	19
Table 3.3: RANS turbulence models .....	28
Table 3.4: Grid independence study .....	31
Table 3.5: Pressure rise comparison between test data and OpenFOAM simulation results .....	33
Table 3.6: Percentage error between different domains from test data .....	39
Table 3.7: Normalized pressure rise data of no-slip and slip upstream boundary conditions .....	41
Table 3.8: Pressure rise of different domains .....	44
Table 4.1: Porous medium coefficients for heat exchangers .....	51
Table 4.2: Mesh settings for major full vehicle components .....	52
Table 4.3: Mesh settings for volume refinement boxes .....	54
Table 4.4: Simulation results and percentage errors .....	57
Table 5.1: Mesh size of all components in Actuator Disk Model .....	68
Table 5.2: Boundary conditions of all components in Actuator Disk Model .....	68
Table 5.3: Pressure rise results from Actuator Disk Model.....	70

## LIST OF FIGURE

Figure 2.1: Normalized pressure rise comparisons of various CFD simulation results and test results.....	6
Figure 2.2: Fan testing setup configuration .....	11
Figure 3.1: Geometry setup.....	16
Figure 3.2: Refinement levels in helixHexMesh .....	17
Figure 3.3: Volume refinement objects .....	19
Figure 3.4: MRF domain.....	20
Figure 3.5: Boundary layer parameter definitions .....	21
Figure 3.6: $y^+$ distribution on fan blade.....	23
Figure 3.7: MRF fvOptions Settings.....	24
Figure 3.8: Comparisons of DNS, LES and RANS .....	27
Figure 3.9 Measuring planes from surface reports .....	30
Figure 3.10: Plots for comparison between pressure rise vs. volumetric flow rate between test data and OpenFOAM .....	33
Figure 3.11: Plots for comparisons between OpenFOAM and other commercial software .....	34
Figure 3.12: Cut plane at 100mm upstream from the fan .....	35
Figure 3.13: Cut plane at 25mm downstream from the fan .....	36
Figure 3.14: Pressure distribution on the fan; velocity distribution in x-axis on the fan..	36
Figure 3.15: Velocity distribution in y-axis and z-axis on the fan.....	37
Figure 3.16: Original geometry of MRF domain.....	38
Figure 3.17: Illustrations of domain B, original and domain A geometries .....	38
Figure 3.18: MRF pressure rise vs. volumetric flow rate comparisons of various domains .....	39
Figure 3.19: Upstream box and downstream tunnel illustration.....	41
Figure 3.20: Pressure rise vs. volumetric flow rate between no-slip and slip upstream boundary conditions.....	41
Figure 3.21: Velocity distribution on a cut plane upstream between slip and no-slip boundary conditions .....	42
Figure 3.22: Domain C (larger domain) & Domain D (smaller domain) .....	43
Figure 3.23: Comparisons of three domains in y-z plane; Domain E.....	43
Figure 4.1: Experimental setup illustration.....	45
Figure 4.2: Fan blade model mathematical simplified configuration .....	46
Figure 4.3: Full vehicle simulation results (airflow rate across radiator) between test and CFD.....	47

Figure 4.4: Heat exchangers .....	49
Figure 4.5: Radiator characteristic curve .....	51
Figure 4.6: Volume refinement boxes: front box & grill box .....	53
Figure 4.7 Volume refinement boxes: heat exchanger box & engine box .....	53
Figure 4.8: Volume refinement boxes: car box, ground box & global box .....	54
Figure 4.9: Comparisons among OpenFOAM, Test and ACE+ simulation results.....	56
Figure 4.10: Front-end vehicle configuration .....	58
Figure 4.11: Velocity in x-axis direction distribution at a cut plane in front of TOC .....	58
Figure 4.12: Pressure distribution at a cut plain in front of TOC .....	59
Figure 4.13: Pressure distribution at a cut plane between TOC and condenser.....	59
Figure 4.14: Pressure distribution at a cut plane between condenser and radiator .....	60
Figure 4.15: Pressure distribution at a cut plane between radiator and the fan .....	60
Figure 4.16: Velocity distribution in y-axis .....	61
Figure 4.17: Pressure drop across condenser, TOC and radiator .....	61
Figure 4.18: Volumetric flow rate across condenser, TOC and radiator .....	62
Figure 4.19: Geometry of original MRF domain and modified MRF domain .....	63
Figure 4.20: Pressure drop comparisons between original MRF domain and modified MRF domain across each heat exchanger .....	63
Figure 4.21: Volumetric flow rate comparisons between original MRF domain and modified MRF domain across each heat exchanger .....	64
Figure 5.1: Correlation between pressure rise and airflow velocity for isolated fan blades .....	67
Figure 5.2: Correlation between pressure rise and volumetric flow rate of MRF, Actuator Disk Model and experimental data .....	70
Figure 5.3: Pressure distribution across the fan of MRF model .....	71
Figure 5.4: Pressure distribution across the fan of Actuator Disk Model.....	71
Figure 5.5: Velocity distribution across the fan in MRF model .....	72
Figure 5.6: Velocity distribution across the fan in Actuator Disk Model.....	72
Figure 5.7: Velocity distribution (Magnitude) on a cut plane 25mm downstream of the fan in MRF model.....	73
Figure 5.8: Velocity distribution (Magnitude) on a cut plane 25mm downstream of the fan in Actuator Disk Model .....	74
Figure 5.9: Axial velocity characteristics on a cut plane 25mm downstream of the fan in MRF model .....	74
Figure 5.10: Axial velocity characteristics on a cut plane 25mm downstream of the fan in Actuator Disk Model.....	75
Figure 5.11: Tangential velocity distribution on a cut plane 25mm downstream of the fan in MRF model.....	75

Figure 5.12: Tangential velocity distribution on a cut plane 25mm downstream of the fan  
in Actuator Disk Model ..... 76

## NOMENCLATURE

$A_b$	Blade area (m <sup>2</sup> )
$C_f$	Skin friction coefficient
$C_v$	Specific heat in constant volume
$C_p$	Specific heat in constant pressure
$D_{ij}$	Porous media tensors
$d$	Viscous loss coefficient (1/m <sup>2</sup> )
$e$	Enthalpy (J)
$E$	Internal energy (J)
$e_t$	Total energy (J)
$f$	Inertial loss coefficient (1/m)
$F_n$	Normal force component (N)
$F_x$	Axial force component (N)
$\vec{F}_c$	Coriolis force per unit mass (N/kg)
$\vec{f}_c$	Centrifugal force per unit mass (N/kg)
$F_\theta$	Circumferential force (N)
$K$	Kinetic energy (J)
$k'$	Turbulent kinetic energy (J)
$k$	Instantaneous energy (J)
$p$	Pressure (Pascal)
$\vec{q}$	Heat flux vector
$Q$	Amount of heat that is applied to the system (J)
$R$	Gas constant (J/kg·K)
$Re$	Reynolds number
$r_{hub}$	Hub radius (m)

$r_{fan}$	Fan radius (m)
$\Delta s$	Surface mesh size (m)
$s_{ij}$	Deformation rate
$S_{ij}$	Mean deformation rate
$s'_{ij}$	Fluctuating deformation rate
$T$	Temperature (K)
$t$	Time
$U_{\infty}$	Freestream velocity (m/s)
$U_{fric}$	Friction velocity (m/s)
$U_d$	Downstream velocity (m/s)
$U_u$	Upstream velocity (m/s)
$\Delta U_c$	Circumferential velocity jump (m/s)
$U_n$	Axial velocity (m/s)
$\vec{u}$	Velocity vector
$V_{bn}$	Blade velocity in blades' orthogonal direction (m/s)
$V_{fn}$	Airflow velocity in blades' orthogonal direction (m/s)
$\nu$	Kinematic viscosity of the fluid (m <sup>2</sup> /s)
$W$	Amount of heat that is done to the surroundings by the system (J)
$\vec{w}$	Relative velocity to the rotating system (m/s)
$\rho$	Density (kg/m <sup>3</sup> )
$\alpha$	Blade angle (degree)
$\mu$	Dynamics viscosity of the fluid (Pa·s)
$\delta$	Boundary layer thickness (m)
$\bar{\tau}$	Stress tensor
$\kappa$	Coefficient of thermal conductivity (W/(m·K))
$\tau_{wall}$	Wall shear stress (N/m <sup>2</sup> )
$\vec{\omega}$	Angular velocity vector of the rotating system (rad/s)

$\gamma$  Reynolds Stress

# CHAPTER 1

## INTRODUCTION

### 1.1 Background

Resulting from the huge environmental impacts from automobiles, growing attention has been concentrated on improving fuel efficiency and reducing engine emission. In the underhood compartment, a more compact and efficient architectural arrangement of electrical and mechanical components is in high demand. Hence it is of vital importance to investigate the airflow behaviour in the underhood region in order to maximize the engine's cooling effect. The high cost and inefficiency of building prototypes and testing have motivated the automotive design departments to utilize Computational Fluid Dynamics (CFD) simulation to predict the airflow behaviour in advance of physical prototype development in order to aid with heat exchanger design and alternatives for the underhood compartment arrangement. Virtual modeling and numerical analysis of underhood thermal management are considered a vital step in the development process of passenger cars.

In the CFD simulation stage, the automotive fan is a very challenging component to model due to the high irregularity of the airflow in a compact limited space. In order to simulate the airflow behaviour accurately, a full detailed geometry of the fan system (blades, shroud, hub etc.) needs to be meshed in an acceptable manner and a transient flow field should be generated. These procedures are very time-consuming and computationally expensive. Because of the limitation of computational resources, it could be problematic to obtain results in a timely fashion. Therefore, in the past decade, a great amount of effort in the field of underhood thermal management has been put into exploring simpler methods to model fans and investigating the limitation and capabilities of fan modeling in various popular commercial CFD software packages.

## 1.2 Motivation

Many mature commercial software packages have been used for CFD purpose in the past decades, such as ANSYS FLUENT, Star-CCM+, and ACE+. They provide well-validated physical modeling capabilities and a wide range of multi-physics applications that are also capable of computing simulation results in a fast and accurate manner. There have been many studies using the above software to investigate underhood airflow behaviour. However, one of the biggest issues of commercial software is the substantial high cost for license fee; besides, the embedded algorithms of the software are not accessible for the users. Hence, the users are not able to study and modify the codes to suit their research purposes, reducing the software's flexibility dramatically.

In 2004, OpenFOAM, an open-source CFD software package, was developed by General Public License (GPL). It provides users with complete freedom of modifications and redistributions of the software, and within terms of the license, the software is guaranteed for continuous free use. Therefore, the use of OpenFOAM may result in a significant financial benefit compared to using a commercial software package. In addition, due to the complexity of the fluid motion, a full 3D, unsteady simulation of the fan is not practical for underhood thermal simulations of production automobiles. Therefore, in commercial CFD software packages, it is common to simulate the effects of the fan on a flow field using approximate models. OpenFOAM has a great potential to produce more accurate results since the programming code is open to modification by the user, allowing the implementation of more sophisticated fan models.

ENGYS is a company that utilizes open-source resources to develop well supported, user-friendly CFD software. It has produced a sequence of CFD software with Graphical User Interface (GUI) using OpenFOAM codes that are called Helyx and Elements. Thus, due to the potential of improved CFD performance and significant financial benefits, ENGYS OpenFOAM was chosen for investigation and validation of underhood thermal management.

### 1.3 Scope of Study

The main objectives of this project are to validate OpenFOAM's capability of underhood thermal simulations and investigate the performance of fan models with increasing levels of fidelity. To achieve the above goal, a systematic evaluation and comparative examination are conducted.

A fan testing facility has provided its fan test data and details of its testing setup. Hence, the bench model for an isolated fan is modeled to simulate the test condition, and the simulation results are compared with the test results. The CFD simulation methods selected for modeling the isolated fan were the Moving Reference Frame (MRF) and Actuator Disk models. The details of these two methods are explained in the following chapter. The simulation results are also compared with existing CFD simulation results from Star-CCM+ and ACE+. Besides the investigation of the isolated fan, a full vehicle model is also simulated including a fan geometry modeled using MRF technique. Again the simulation results are compared to test data.

This project is divided into three phases, as described below.

- i. Explore and validate MRF technique in ENGYS OpenFOAM using test bench simulation; compare results with existing CFD results and test data
- ii. Run full vehicle simulations with MRF technique; compare results with existing CFD results and test data
- iii. Explore and validate Actuator Disk technique in ENGYS OpenFOAM using test bench simulation; compare results with existing CFD results and test data

## CHAPTER 2

### LITERATURE REVIEW

#### 2.1 Introduction to Fan Modeling

In order to predict the airflow behaviour in the underhood compartment, it is crucial to simulate the fan performance using the appropriate CFD modeling method for turbomachinery. The choice of model is dependent on the level of accuracy one desires to achieve and also computational limitation. There are a few common fan modeling techniques available in the literature.

##### 1) Sliding Mesh Method

Sliding Mesh is currently considered the most accurate method for fan modeling in the automotive industry. It models the geometry in detail and simulates the actual rotation of the fan. Full transient simulations are conducted and the mesh in each zone is generated independently. The adjacent cell zones are able to move relative to each other in discrete steps along the grid interface which is the interface zone between neighboring cell zones. However, its high accuracy demands a large amount of computational resources and a much longer time to complete the simulation compared to other turbomachinery CFD methods, which becomes the main concern for many industrial companies in regard to the simulations' turn-around time and financial cost.

##### 2) Moving Reference Frame (MRF) Method

MRF stands for Multiple Reference Frame, which is also known as the 'frozen rotor approach'. It is a CFD modeling method to simulate rotating machinery, such as turbines, ventilators, and fans. This approach approximates the transient rotating motion at an instant in time. A rotating frame of reference is set up which changes the governing equations in the rotating zone. Since the body is not simulated as being physically rotated, this technique is considered as steady-state which requires a lot shorter time than the transient simulation procedure. This method has been a popular choice for the automotive industry since it offers a good balance between accuracy and computational cost.

### 3) Actuator Disk Method

Actuator Disk theory is also known as momentum theory, which describes a mathematical model of an ideal Actuator Disk, such as a rotor or propeller. The fan is modeled as an infinitely thin disk which induces a constant velocity along the axis of rotation and offers no resistance to air passing through it. Through this method, the fan is not modeled exactly, but the momentum that is transferred from the fan to the surrounding fluid region is predicted. This theory assumes that the thrust loading and velocity are uniform over the disk and viscous effects are not considered. Actuator Disk is considered the simplest method that requires the least computational cost since no detailed fan blade geometry is needed for grid generation and the actual detailed airflow is not being simulated adjacent to the fan. Therefore, the accuracy of the simulation results might be compromised.

Considering the feasibility of these fan modeling methods, MRF and Actuator Disk are selected for investigation in this research due to their lower demand on computational resources. Previously at Fiat Chrysler Automobiles (FCA), CFD simulations on an isolated fan have been studied using different software and methods, and the results were compared to available test data as shown in Figure 2.1. Star-CCM+ appears to have the most accurate results. Its curve trend complies with test results but has a lower value throughout the entire range. Beyond 1700 CFM, the pressure rise gradually becomes more accurate as the volumetric flow rate increases. MRF method using CFD-ACE+ seems to have the biggest deviation. As the volumetric flow rate increases, the software starts to greatly underestimate the pressure rise. CFD-ACE+ fan blade model behaves a bit unpredictably; at a very low volumetric rate and high volumetric rate, its data correlates well with the test data but between 500 and 2000 CFM the simulation results largely deviate from the trend. The Fan Blade Model is one of the two available fan models in CFD-ACE+ which requires the averaged blade angle. Local thrust and torsional force that are imposed on the flow by the fan are calculated first, and then the model calculates the equivalent body forces that are introduced into the momentum equations via source terms. The flow that enters and leaves the fan region radially through the tip is ignored in this fan model as well as the resistance due to the blockage

effect of fan blades. Therefore, the user must input a correction factor during the setup of the model.

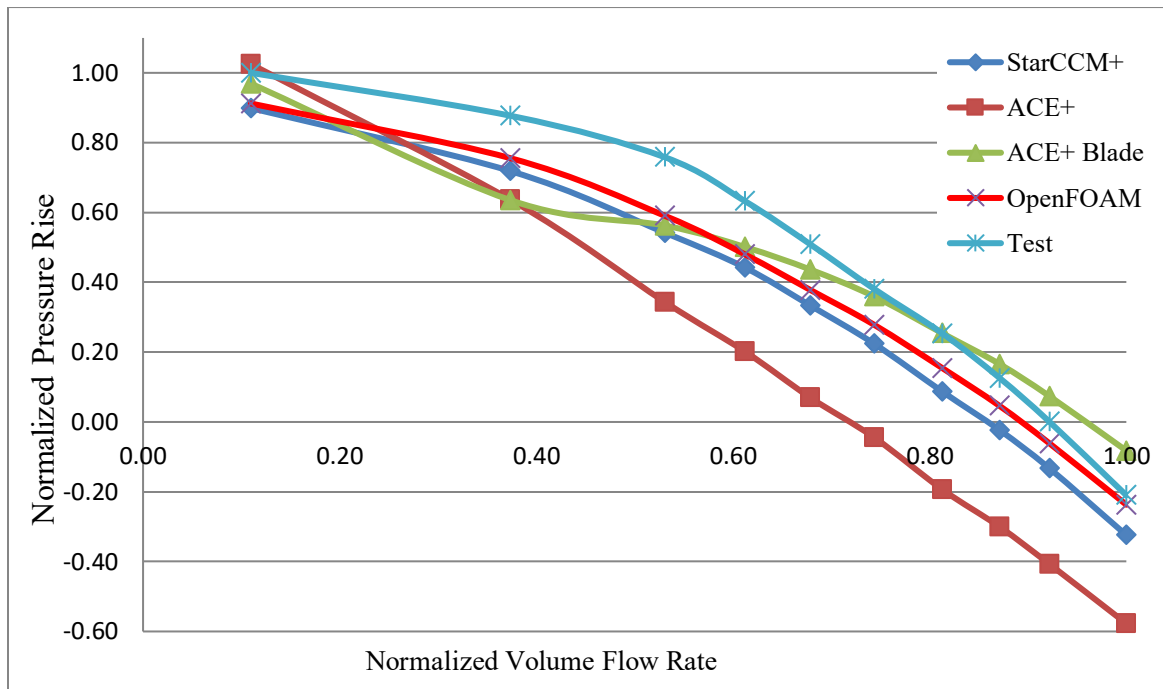


Figure 2.1: Normalized pressure rise comparisons of various CFD simulation and test results. Data obtained through private communication with Sreekanth Surapaneni.

## 2.2 Moving Reference Frame

Although the MRF model is well known for its drawback of under-predicting fan performance, in order to show that the method however is still a reliable fan modeling strategy, Gullberg et al. [1] conducted a study on a correction method for stationary MRF fan modeling by applying a correction factor on the fan speed. The investigation showed that by increasing fan speed by 14% at each operating point, the simulation results accurately predicted the pressure rise and matched with the experimental data under most of the driving conditions. In addition, the author also investigated the influence of different blade positions on the simulation results. The fan was rotated 15 and 30 degrees axially and the results showed that the effect was not as significant; the overall error was one order of magnitude smaller and therefore could be considered negligible.

Gullberg et al. [2] conducted a further investigation on studying the fan flow behaviour of three fans with different radius and functionality. Two classic fans with diameters of 750mm and 680mm were optimized for axial flow condition, and the third fan had a diameter of 750mm which was designed to have a stronger performance for mixed flow condition and high system restriction. It was shown that the mixed fan flow possessed a different tendency in the transition and radial flow region and had a more accurate performance than the classic fans. The MRF domain was studied as well; the default domain was a cylinder-shaped region surrounding the blade with a radius at the midpoint between the fan tip and the fan ring. The other MRF domain expanded radially until it covered the fan ring. Simulation results showed that the second domain improved the accuracy by 6%.

In 2011 Gullberg et al. [3] carried out a more thorough investigation on the influence of various MRF domains on the pressure rise for underhood purposes. Volvo 3P fan test rig was chosen to be the test objects for this study. A heavy duty fan with fan ring and fan shroud was placed in the middle of the connection location of the pressure chamber and outlet chamber. To simulate the influence of the engine blockage, a 3D mock-up engine was also included in the test. The surface mesh was created in ANSA and later meshed in Star-CMM+ with a total of nine million cells. Realizable k-epsilon was chosen to be the turbulence model with 2-layer prism layers. The authors have done a detailed study on the influence of MRF domain on the pressure rise. The domain was expanded radially, forward towards the face of the shroud and backward as far as possible before interfering with other parts of the model. The simulations indicated that the MRF domain has a significant effect on the pressure rise and showed that domain III, which extended to the forward face of the mock-up engine and backwards to the face of the shroud. Its deviation between test results and simulation results was less than 2% which was the best result among all the attempts. The choice of turbulence was also investigated; simulations were done with k- $\omega$  SST and quadratic k-epsilon as well. The results show little influence on the pressure rise comparing to the MRF domain.

Barron et al. [4] studied the effect of the location of computational boundaries on the pressure rise through the fan and on the flow behind it using MRF method. Both

upstream and downstream compartments were shaped as cylinders. Configuration A had an upstream cylinder with a bigger diameter than the downstream one (by about two fan diameters). Configuration B had exactly the opposite setup for the upstream and downstream. Configuration C was composed of upstream and downstream of the same sizes. The results showed significant influence on the pressure rise by the various sizes of computational boundaries. Configuration A and C both comply with the experimental data well, while configuration B predicted the pressure rise and velocity field incorrectly. The pressure contours of Configuration B on the measuring plane right behind the fan was in good agreement with experimental results although the pressure was poorly simulated. For the upstream velocity magnitude contours, configuration B appeared to predict the performance as accurately as the other configurations.

Regarding the comparison between OpenFOAM and other CFD commercial packages, Bothe et al. [5] completed an investigation of incompressible turbomachinery and examined the differences between OpenFOAM and ANSYS FLUENT in terms of accuracy and efficiency. A single rotor axial fan and a contra-rotating fan were modeled using Moving Reference Frame approach. Additionally, the influence of turbulence models  $k-\omega$  SST model and Spalart-Allmaras were studied. The results showed that both software packages underestimate the pressure rise and OpenFOAM has a relatively more accurate prediction, this might be caused by the different formulations of the wall function from ANSYS FLUENT. In the stable operating range, Spalart-Allmaras showed a better result than  $k-\omega$  SST model. It might be caused by the additional transport term of the dissipation in  $k-\omega$  SST model which creates a better resolution of the vortex structures and leads to a greater pressure loss.

Airflow distribution of a radiator axial fan used in an acid pump truck Tier4 (APT T4) Repower was modeled and studied by Jain and Deshpande [6] using ANSYS FLUENT MRF technique. The simulation results were then compared with both theoretical and experimental results. The pressure contours, velocity vectors etc. were plotted in order to show the flow characteristics for different orientations of the fan blade. In terms of solution method, SIMPLE-first order upwind was selected with the convergence criteria of  $1e-4$ . The simulation results provided an insightful understanding

of the behaviour of fluid flow of different fan blade orientations. The plots showed that around the outer diameter of the flow domain a high flow region was formed, and a low reverse flow region was formed at the center behind the fan hub; between the high and low reverse flow regions, strong circulation vortices were created. Strong circulation regions were also observed behind the fan blades. This phenomenon was caused by the hub obstruction. The flow of air was interrupted and lead to unwanted reverse flow regions. In addition, this study revealed that the left-oriented blade fan with counterclockwise rotation performed the same as a right-oriented blade fan with clockwise rotation.

Kumawat [7] investigated the flow behaviour through axial fans with the aim to achieve maximum efficiency. The main parameter being studied was the blade number; though other factors like noise level, velocity, temperature and pressure distribution on the blade surface were also examined to study the influence of each parameter on an axial fan. The CFD simulation was carried out in ANSYS CFX. Turbulence model was selected as k- $\epsilon$  model with standard wall function. The study revealed that the optimized design has eleven blades and as a compromise between efficiency and cost, axial fans with five to twelve blades are all within the good practical range.

### **2.3 Actuator Disk**

Tzanos and Chien [8] used Actuator Disk method to model the effect of an axial fan in STAR-CD with the aim of developing and validating a simple fan model that can be used to represent the fan as a source of axial and circumferential body forces. The model requires some input parameters such as the rotational speed of the fan, geometry fan data, lift and drag coefficients of the blades. They used the experimental results from DaimlerChrysler to validate the CFD simulation results. The axial velocity was measured at different locations downstream of the fan starting from 25mm from the downstream face of the fan hub, and at this specific point, the circumferential velocity was also recorded. The results show that the Actuator Disk Model over predicted the axial velocity with a maximum discrepancy at the tip of the blades. Besides the tip of the blades, a

maximum discrepancy of 14% took place at the measuring point where is closest to the fan. The overall trend complies with the experimental data.

The University of Windsor/DaimlerChrysler Fan Test Facility an experiment that was aiming to measure the pressure rise of the fan and the detailed velocity field downstream of the fan. For numerical simulations, FLUENT fan model was investigated to predict fan performance by Yang [9]. The simulation setup required the input of the polynomial relation of the experimental pressure rise and corresponding fluid velocity magnitude normal to the fan. To simulate the swirl as well, the simulation settings needed the relation of the radial and tangential velocity components as a function of radial distance which was both measured in the experiment by setting up two downstream planes at 25mm and 100 mm below the base of the hub. The results showed that the FLUENT fan model under predicted the tangential and radial velocity significantly but gave a good prediction of the fan performance curve. When the swirl was included, FLUENT had a good estimation on the axial and tangential velocity components but it severely under predicted the radial component. If the swirl was excluded, the axial velocity was predicted reasonably well while radial and tangential velocity were poorly estimated.

## **2.4 Experimental Setup**

A fan testing facility has provided the details of its test setup for fan experiments. The duct shown in Figure 2.2 was placed in a large room with an ambient temperature of 23° Celsius and 30% humidity. The testing fan along with its shroud and hub were placed on the right end of the duct. In order to measure the pressure in the chamber precisely, two sets of settling screens were added in the front and rear side of the duct with the aim to smooth out and stabilize the airflow in the duct. In the middle of the duct, there were four venturi differential pressure taps to measure the air mass flow through the rig. The main fan drive that drew the airflow through the duct was installed at the end of the duct. Behind the test board mounting location and the front settling screens, a fan pressure tap was mounted and used to measure the pressure in the duct and this set of data was provided as the testing results. The test was conducted at 14 different operating points

with the fan rotating at different speeds and with various mass flow rates. The inlet area, electric power, volumetric flow rate and pressure rise were provided. However, the uncertainty of measurement for pressure rise at each operating point was not available, so in this research, the listed experimental data is a specific number instead of a range. All the isolated fan simulations in this project were designed to model the test setup as accurately as possible and the simulation results are compared with test results. Therefore, a conclusion could be drawn regarding the level of accuracy of the corresponding fan modeling method in OpenFOAM.

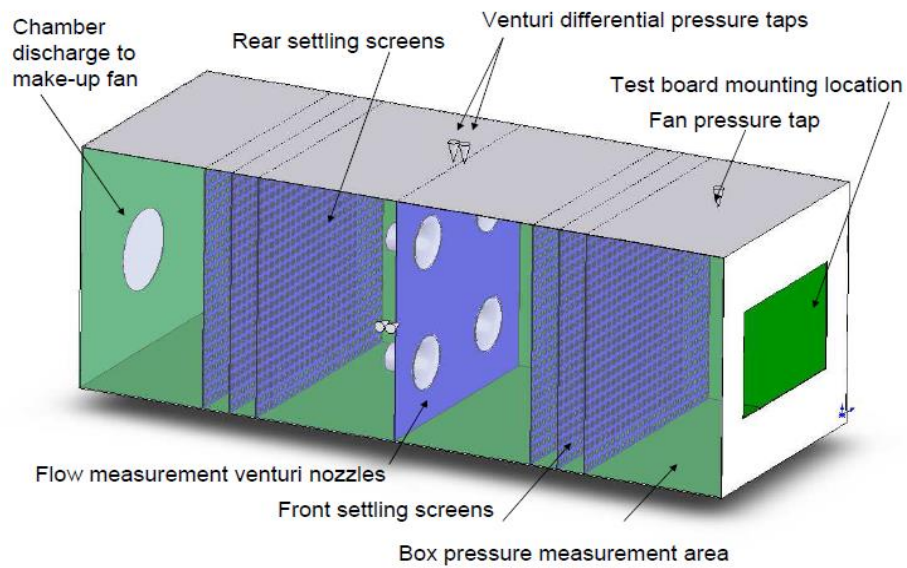


Figure 2.2: Fan testing setup configuration

## CHAPTER 3 MOVING REFERENCE FRAME

### 3.1 Theory

Computational fluid dynamics (CFD) is defined as a set of methodologies that analyzes a system of fluid flows including the thermal heat transfer and heat conduction effects etc. numerically using computer-based simulation. The fluid domain usually is defined by a solid boundary condition and the behaviour of the entire system can be visualized and studied in the CFD simulation software or a third-party visualization tool. CFD code is a numerical algorithm that aims to solve fluid flow problems. The first step of setting up a CFD simulation is to define the physics of the fluid system that the user is interested in studying. Then, the geometrical and mathematical model that was defined in step one is translated to numbers that the computer is able to read, and this procedure is named discretization. The first discretization takes place on the space domain, where the fluid domain and solid surfaces are represented by a finite number of isolated points, which then is a grid or mesh. This procedure can be extremely complex and the quality of the grid generation could have a crucial influence on the accuracy of the results. After space discretization, discretization of the mathematical equations on each mesh point is performed. The algebraic relations between neighboring mesh point values is called the numerical scheme. As a consequence of replacing the continuum physical model by a discrete numerical system, the error from discretization is unavoidable, therefore the most suitable numerical scheme should be carefully chosen with the aim to reduce the numerical error to the minimum through analyzing the simulation stability, consistency, and accuracy. The last step is to solve the numerical scheme to obtain the main flow variables. The solution algorithms could be chosen from time-dependent or steady flows.

#### 3.1.1 Governing Equations

The complexity of fluid mechanics is widely recognized and with the phenomena such as turbulence, the simulation of various flow situations could be very difficult. In order to solve this issue, the basic laws governing fluid flows were established. Although there are many different mathematical forms to describe the fluid behaviour, CFD allows the development of a general form of the laws based on the concept of conservation laws,

which is the fundamental concept behind the laws of fluid mechanics. Conservation laws are also the essential perception of the whole physical world, which states that a particular measurable property of an isolated physical system does not change as the system evolves over time. For a viscous heat conducting fluid, the flow is governed by the Navier-Stokes equations, namely the conservation of mass (3.1), conservation of momentum (3.2) and conservation of energy (3.3). It is crucial to keep in mind that not all fluid quantities obey a conservation law, such as pressure, temperature, and entropy etc. Navier-Stokes equations can be simplified to different forms based on the type of flow problems that are being solved. For a compressible fluid, the instantaneous equations are presented as below as dimensional differential conservative form, which models an infinitesimally small fluid element fixed in space that does not move with the flow.

$$\frac{\partial \rho}{\partial t} + \vec{\nabla} \cdot (\rho \vec{u}) = 0 \quad (3.1)$$

$$\frac{\partial}{\partial t} (\rho \vec{u}) + \vec{\nabla} \cdot (\rho \vec{u} \vec{u}) + \vec{\nabla} p = \vec{\nabla} \cdot \bar{\tau} \quad (3.2)$$

$$\frac{\partial}{\partial t} (\rho e_t) + \vec{\nabla} \cdot [(\rho e_t + p) \vec{u}] = -\vec{\nabla} \cdot \vec{q} + \vec{\nabla} \cdot (\vec{u} \cdot \vec{\tau}_x, \vec{u} \cdot \vec{\tau}_y, \vec{u} \cdot \vec{\tau}_z) \quad (3.3)$$

where  $\bar{\tau}$  represents the stress tensor and is expressed as,

$$\bar{\tau} = \begin{bmatrix} \tau_{xx} & \tau_{xy} & \tau_{xz} \\ \tau_{yx} & \tau_{yy} & \tau_{yz} \\ \tau_{zx} & \tau_{zy} & \tau_{zz} \end{bmatrix} = [\vec{\tau}_x, \vec{\tau}_y, \vec{\tau}_z] \quad (3.4)$$

Fourier's law of heat conduction deduced a relationship between the heat flux and temperature gradient. Heat flux vector  $\vec{q}$  is calculated as below, where  $\kappa$  is the coefficient of thermal conductivity.

$$\vec{q} = -\kappa \vec{\nabla} T \quad (3.5)$$

Assuming a calorically perfect gas, the following relations could be applied, where

$$p = \rho RT \quad (3.6)$$

$$e = C_v T \quad (3.7)$$

$$C_p - C_v = R \quad (3.8)$$

Conservation of mass states that the rate of the increase of mass in fluid element equals to the net rate of flow of mass that goes into the element. It is also called the Continuity Equation. The first term in the equation represents the change in density, and the second term is the convective term which describes the total mass of the flow that crosses the boundary. When the fluid is considered incompressible, the density is assumed as a constant. Hence the equation of conservation of mass is simplified to

$$\vec{\nabla} \cdot (\rho \vec{u}) = 0 \quad (3.10)$$

Conservation of momentum is developed based on Newton's second law which states that in an inertial reference frame, the vector sum of the forces  $\vec{F}$  on an object is equal to the mass  $m$  of that object multiplied by the acceleration of the object,  $\vec{F} = m\vec{a}$  [10]. The forces that are applied to the fluid particles can be classified into two categories. The first category is the surface forces that occur at the surface of the fluid particle such as pressure and viscous forces; the second is the body force which acts on a defined volume, such as gravity, centrifugal and Coriolis forces.

Conservation of energy represents by the first law of thermodynamics, which states that the total energy of an isolated system is constant; energy can be transformed from one form to another but can be neither created nor destroyed. It can be formulated as  $\Delta E = Q - W$ , where  $E$  is the internal energy of the closed system,  $Q$  represents the total amount of heat that is applied to the system and  $W$  is the amount of work that is done to the surroundings by the system.

### 3.1.2 Moving Reference Frame

In OpenFOAM, a utility function called *MRFSource* can be included in the model in order to simulate rotating components in stationary meshes. This is achieved by adding the effects of Coriolis and centrifugal forces as a momentum source. Without simulating the actual grid rotating motion, MRF approach is able to model different cell zones or mesh domains rotating along different axes at various speeds using the steady-state approximation. The Coriolis force is an inertial force that acts on an object which

moves relative to a rotating reference frame. It leads to an apparent deflection of the path of the moving object due to the rotation of the system, and the Coriolis force per unit mass can be formulated as below (3.11), where  $\vec{w}$  is the velocity of the object relative to the rotating system, and  $\vec{\omega}$  represents the angular velocity vector of the rotating system.

$$\vec{F}_c = -2(\vec{w} \times \vec{\omega}) \quad (3.11)$$

The centrifugal force per unit mass is represented as

$$\vec{f}_c = -\vec{\omega} \times (\vec{\omega} \times \vec{w}) \quad (3.12)$$

Since the mass balance of the system does not change because of the existence of the Coriolis force or centrifugal force, the conservation of mass equation of the system remains the same. The governing equation of the fluid in the moving reference frame for the relative velocity formulation can be expressed as

$$\frac{\partial \rho}{\partial t} + \vec{\nabla} \cdot (\rho \vec{w}) = 0 \quad (3.13)$$

However, for the conservation of momentum equation, the Coriolis force and centrifugal force have a great influence on the rotating flow since the total force on the domain is changed significantly. After including these two forces into consideration, the new conservation of momentum equation is shown as

$$\frac{\partial}{\partial t} (\rho \vec{w}) + \vec{\nabla} \cdot (\rho \vec{w} \vec{w}) + \vec{\nabla} p = \rho \vec{f}_e - \rho \vec{\omega} \times (\vec{\omega} \times \vec{w}) - 2\rho (\vec{w} \times \vec{\omega}) + \vec{\nabla} \cdot \vec{\tau} \quad (3.14)$$

## 3.2 Mesh Generation

### 3.2.1 Refinement Settings

The first step of setting up the simulation is to import the geometry. In OpenFOAM, the CAD model could be in STL, STEP or IGES format. With the aim to compare the capability of different CFD software, the simulations that were conducted in OpenFOAM utilized the exact same geometry that were used in Star-CCM+ and CFD-ACE+. As mentioned in the previous chapter, before this project was initiated, the same test bench fan simulation has been modeled and studied using Star-CCM+ and CFD-ACE+. There were eight CAD parts in the whole fan testing system, namely the fan blades, shrouds, hub, motor, tunnel, tunnel inlet, tunnel outlet and MRF domain as showing in Figure 3.1.

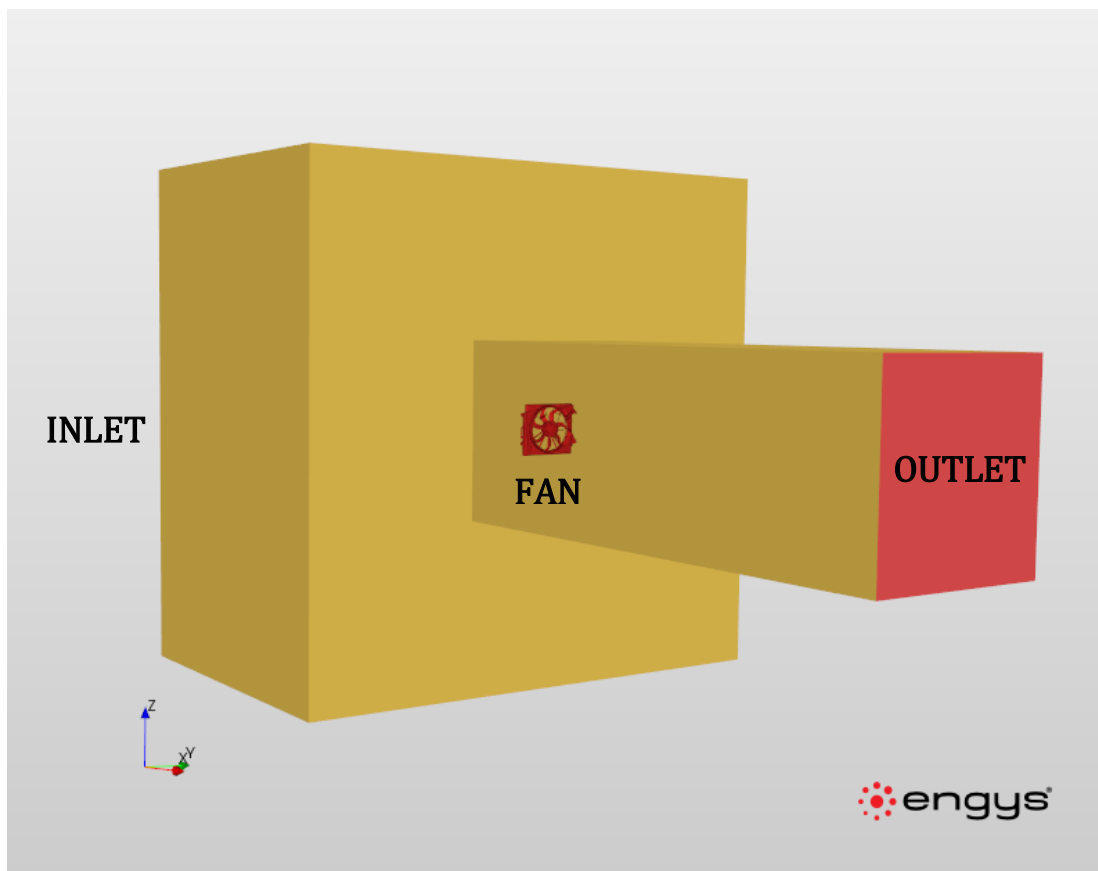


Figure 3.1: Geometry setup

The utility *surfaceCheck* performs topological checks on the imported geometry in order to make sure the models are valid for further meshing in *helyxHexMesh*. *HelyxHexMesh* utility aims to create high-quality conformal meshes that are composed of both hexahedral and split-hexahedral elements. To initiate the mesh generation process, a base mesh needs to be set up. In this simulation, a base mesh spacing of 0.3 is used in order to achieve a proper meshing size. After the base mesh size is defined, the minimum and maximum refinement levels are to be specified for each mesh patch. The minimum level defines the cell size that is achieved generally across the patch domain and when the surface curvature exceeds the user-defined threshold, the maximum level of refinement size is adopted. The base mesh size is equal to the level 0 refinement. Each level increased above level 0 leads to the cell size decreased by half the length of the previous level on each Cartesian axis as showing in Figure 3.2. For example, in this case, since base mesh spacing is set to 0.3m, which means refinement level 0 has a meshing cell size of 0.3m, and refinement level 1 will have a cell size of 0.15m.

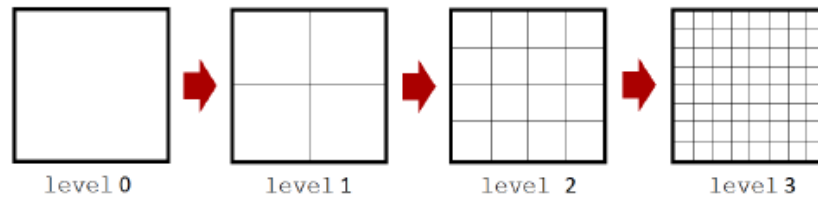


Figure 3.2: Refinement levels in helyxHexMesh

Besides setting up refinement levels, there are a few optional settings that can be further specified for the mesh generation, as listed below.

*Proximity Refinement:* When two surfaces or patches are very close to each other, the user is able to define a certain integer of extra refinement levels in addition to the maximum level specified previously in that region to create a finer mesh in the vicinity to prevent cells collapsing.

*Refinement Feature Angle:* In order to construct a relatively high-quality mesh, the feature edges with a feature angle greater than a certain value should be identified and the specified maximum refinement level is performed on the surface edges. Usually, the feature angle is set as 20 degrees.

*Refine Surface Boundary:* Contrary to the previous function, the specified maximum level of refinement is performed on all surface edges disregarding the feature angle. This setting is usually set as false for all simulations since when the feature angle is very small, very fine mesh is not necessary for the model.

*Cells Across Gap:* When there is a gap in the model, the user could specify a maximum number of cells that could be created across the gap. The number of cells is usually set as 2.

*Cells Between Levels:* For the neighboring mesh patches that have different refinement levels, this function creates a transition zone with a certain number of buffer layers as specified by the user. Usually, it is set as 2 layers.

The final mesh refinement settings for the system are shown in Table 3.1. Due to the very detailed CAD geometry of the fan system, the blade, shroud, hub, and motor adopted, a relatively smaller cell size of about 2mm is used. The tunnel, inlet and outlet are made of simple smooth planes; therefore, a coarser mesh was selected in this case with a cell size of 19mm.

Patch Name	Minimum Refinement Level	Maximum Refinement Level	Proximity Refinement Level	Cell Size (m)
Blade	7	7	1	0.002
Shroud	7	7	1	0.002
Hub	7	7	1	0.002
Motor	7	7	1	0.002
Tunnel	4	4	0	0.019
Inlet	4	4	0	0.019
Outlet	4	4	0	0.019

Table 3.1: Mesh settings for MRF model

Compared to the global base mesh size of 0.3m, the difference between it and the fan cell size is relatively large, which should be avoided in mesh generation. Hence a few primitive objects were created as transition zones. Adjacent to the fan, two volumetric

cylinder zones were created with diameters greater than the blade and shroud. One cylinder extended more than the other one radially and axially as showing in Figure 3.3.

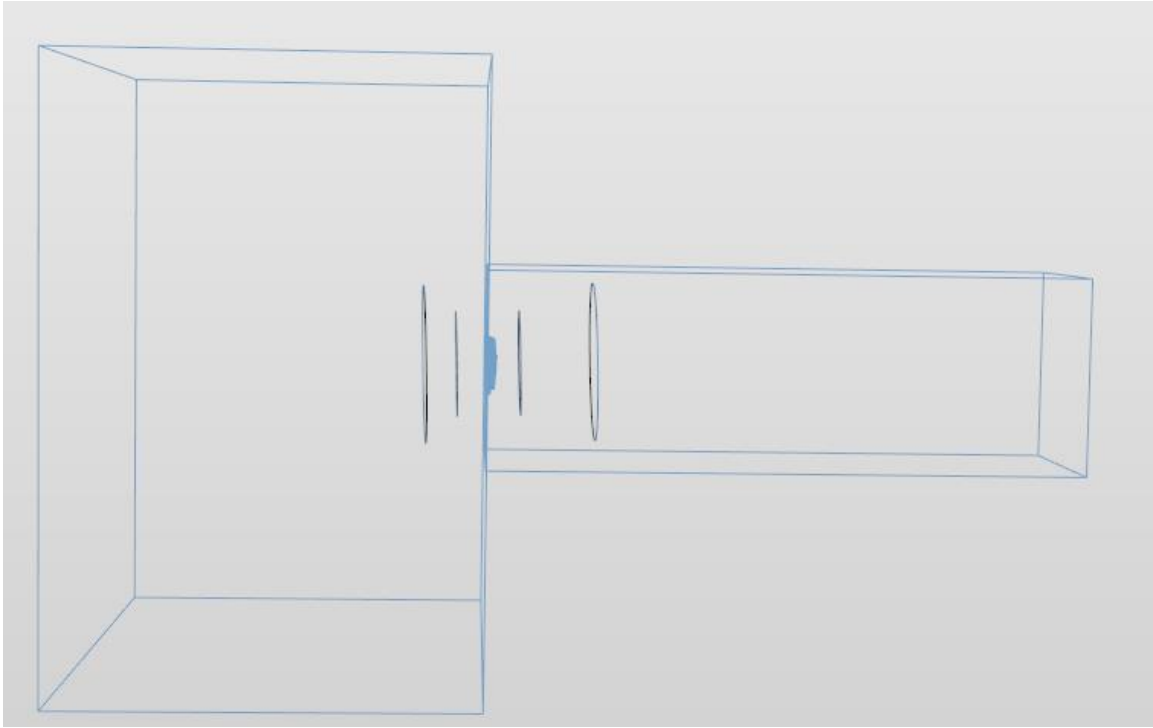


Figure 3.3: Volume refinement objects

Besides the two cylinders, a spherical volumetric zone is added into the system which surrounds the whole tunnel and the refinement level is set as level 1. The detailed geometry dimensions and cell sizes are shown in Table 3.2 (corresponding data for the fan blade is added in the table for comparison). All primitive objects are set to be isotropic. Cylinder\_S refers to the smaller cylinder component and Cylinder\_L refers to the larger cylinder component.

Patch Name	Radius (m)	Thickness (m)	Refinement Level	Cell Size (m)
Blade	0.245	0.05	7	0.002
Cylinder_S	0.5	0.6	6	0.005
Cylinder_L	0.75	2	5	0.009
Sphere	6	-	2	0.075

Table 3.2 Dimensions and mesh sizes of volume refinement objects

As previously mentioned, the STL geometry of the MRF domain was provided. It encloses the entire blade and extends radially and axially before intersecting with the shroud as shown in Figure 3.4. The MRF domain is set as a volumetric mesh with a mesh size of 0.009m. A corresponding MRF internal cell zone is required to be created which is a domain of cells that define volumetric sub-regions of the mesh.

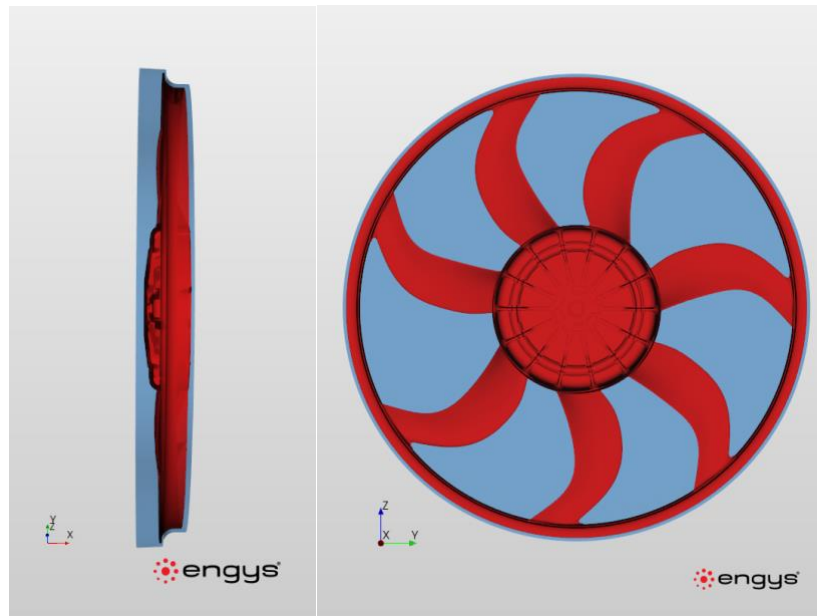


Figure 3.4: MRF domain

### 3.2.2 Boundary Layer

When the flow gradients are strong, the size and distribution of mesh sizes have a dramatic influence on the simulation results. The flow characteristics significantly depend on the mesh resolution. Therefore, the near-wall cells should be carefully defined in order to resolve the flow behaviour accurately. In OpenFOAM, there are two methods that model the flow behaviour of the boundary layer region. For flows with low Reynolds number where viscous effects near the wall are crucial, explicit modeling is recommended. The flow is modeled and explicitly solved near the wall including the inner region of the boundary layer. The  $y^+$  should be around one and it is necessary to have a large number of cell layers near the wall. The second method is called “wall function” which is ideal for high Reynolds number flows, and it is adopted in this project since the region near the fan system is highly turbulent. It simulates the flow quantities in

the fully turbulent region away from the wall. Thus, solving the viscous-dominated inner region using a complicated near-wall mesh is not required.

To set up the boundary layers in OpenFOAM, one can define a combination of three of the following parameters for each surface patch.

*Fch*: refers to  $\Delta_1$  in Figure 3.5, which is the first cell height of the near-wall mesh with an absolute distance in meters.

*expansionRatio*: the ratio of the neighboring cell heights. In this case in Figure 3.5, expansion ratio is equal to  $\frac{\Delta_2}{\Delta_1} = \frac{\Delta_3}{\Delta_2} = \frac{\Delta_4}{\Delta_3} = \frac{\Delta_5}{\Delta_4}$ . The expansion ratio is constant among all layers.

*nSurfaceLayers*: the number of the cell layers

*finalLayerThickness*: the ratio of the final layer height and the surface mesh cell size, which is  $\frac{\Delta_5}{\Delta_S}$  in this case.

*maxLayerThickness*: the ratio of the total layer height and the surface mesh cell size, which is  $\frac{\Delta_L}{\Delta_S}$  in Figure 3.5.

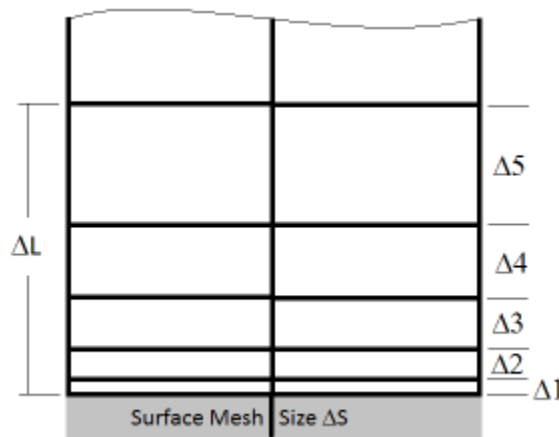


Figure 3.5: Boundary layer parameter definitions

The boundary layer thickness can be estimated using the following formula which is the Blasius solution for laminar flow over a flat plate [11],

$$\delta(x) = 5 \sqrt{\frac{\nu x}{U_\infty}} \quad (3.15)$$

where  $\nu$  represents the kinematic viscosity of the fluid and  $U_\infty$  is given by

$$U_\infty = r\omega = 0.245 \times 210 = 51.45 \text{ m/s} \quad (3.16)$$

where  $r$  is the radius of the fan, and  $\omega$  represents the rotational speed of the fan in rad/s. The testing facility has operated the experiments with a fan rotational speed at around 210 rad/s. By using the respective parameters from this project, the approximate boundary layer thickness can be estimated below,

$$\delta(x) = 5 \sqrt{\frac{0.000015881 \times 0.245}{0.245 \times 210}} = 0.00137 \text{ m} \quad (3.17)$$

In order to get a rough estimation of first cell height of the boundary layer, the following formulas for flat-plate boundary layer theory [11] were used.

$$Re = \frac{\rho U_\infty L}{\mu} = \frac{1.155 \times 51.45 \times 0.245}{0.0000183} = 793842 \quad (3.18)$$

$$C_f = \frac{0.026}{Re^{\frac{1}{7}}} = \frac{0.026}{793842^{\frac{1}{7}}} = 0.00373 \quad (3.19)$$

$$\tau_{wall} = \frac{C_f \rho U_\infty^2}{2} = \frac{0.00373 \times 1.155 \times 51.45^2}{2} = 5.7 \quad (3.20)$$

$$U_{fric} = \sqrt{\frac{\tau_{wall}}{\rho}} = \sqrt{\frac{5.7}{1.155}} = 2.22 \quad (3.21)$$

$$\Delta s = \frac{y\nu}{U_{fric}} = \frac{30 * 0.00001588}{2.22} = 2.14 \times 10^{-4} \text{ m} \quad (3.22)$$

Since the above calculation is aimed to estimate the flat-plate condition, it is only an approximation for computing the boundary layers on the fan. The fan blade geometry is highly irregular with various curvatures and corners. By setting up the initial simulations with the above parameters, the results showed that the average  $y^+$  is around 10 on the blade, and the majority of the area on the blade had a  $y^+$  between 5 and 20. Therefore, many more simulations were done to achieve a desired  $y^+$  above 30 by experimenting with first cell height, expansion ratio and numbers of the boundary layer.

Adjusting the first cell height was the most influential factor to change the  $y^+$ . The most optimal simulation results showed an average  $y^+$  of 35 across the blade and with majority of the area possessing a  $y^+$  ranging from around 30 to 80. The edge of the blades had the highest  $y^+$  between 70 and 80 while the hub with adjacent areas had a relatively low  $y^+$  which was expected. The average first cell height, in this case, was 0.000675m and the total height of the boundary layer was 0.00149m.

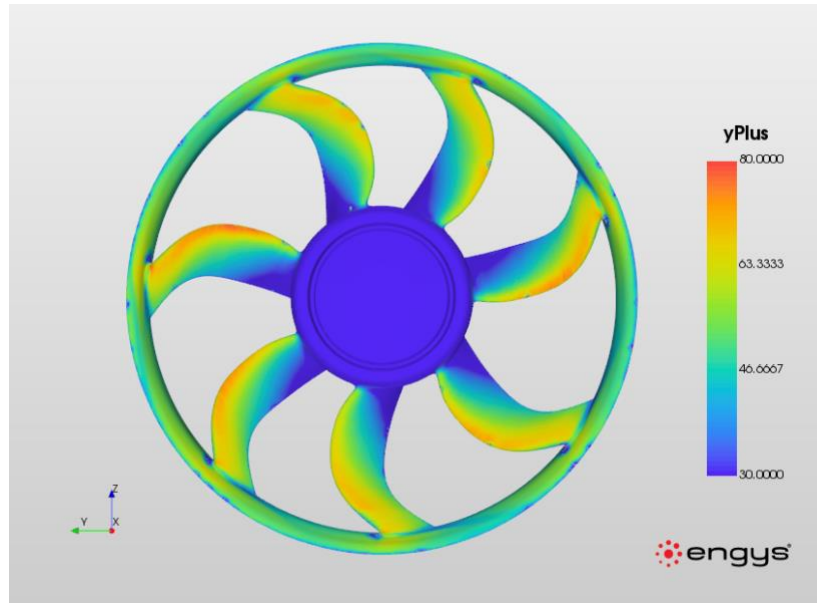


Figure 3.6:  $y^+$  distribution on fan blade

### 3.3 Boundary Conditions

After the mesh was successfully generated, boundary conditions were applied to each surface patch. Blade, shroud, hub, motor and tunnel were all defined as no-slip solid walls. For the fan system and downstream tunnel, the no-slip option describes the real boundary conditions by assuming that the fluid has zero velocity at the solid boundary relative to the boundary. For the upstream geometry box, it is a numerical boundary for defining the simulation zone instead of a real solid object, hence it would be ideal to define it as a slip wall. However, the geometry that was provided combined the upstream box and downstream tunnel as one part, so different boundary conditions are not able to be applied to the two regions. Since the airflow in the downstream tunnel is more

significant to be studied, the entire tunnel is set up as no-slip wall, which also complies with the setup in Star-CCM+ and CFD-ACE+.

The inlet patch was defined as a fixed flow rate inlet, and for each operating point, the volumetric flow rate was changed to various values based on the testing conditions. The outlet patch was set up as a static pressure outlet. These settings allow the fluid to enter and exit the solution domain.

In OpenFOAM, MRF could be defined and set up by creating a source in the dictionary file 'fvOptions' after the mesh was generated. In fvOptions file, as shown in Figure 3.7, the MRF mesh patch was specified as a cell zone, then the origin coordinate of the MRF domain, the MRF rotating axis and fan rotating speed are specified. The unit of the rotational speed of the fan is rad/s.

```
MRF_mrf
{
    type MRFSource;
    active true;
    MRFSourceCoeffs
    {
        selectionMode cellZone;
        cellZone MRF;
        origin ( 0.0 0.0 0.0 );
        axis ( 1.0 0.0 0.0 );
        omega constant 212.686;
        rotatingPatches ( );
        nonRotatingPatches ( );
        attachedPatches ( );
    }
}
```

Figure 3.7: MRF fvOptions settings

### 3.4 Solver Settings

#### Incompressible

As mentioned before, the simulations are set up as steady-state which means the flow properties at any location of the simulation domain do not change with time. The maximum flow velocity of the entire simulation region does not exceed 60m/s which is equivalent to Mach number of 0.176. Since the flow is steady and isothermal, when Mach number is smaller than 0.3, the compressibility effect is negligible and the flow can be

considered as incompressible [12]. Hence, the density of the fluid is treated as constant, which physically means that the variation in pressure and temperature is small enough that its influence on the flow density could be ignored.

### **SIMPLE Solver**

In OpenFOAM, there is no generic solver that applies to all types of flow conditions. The available solvers are categorized based on the type of continuum mechanics such as incompressible flow, heat transfer, combustion etc. For incompressible flows, there are a few solvers available and the majority of them are for transient simulations except for *simpleFoam* and *buoyantBoussinesqSimpleFoam*. Both have the capability to solve MRF and porous regions but *buoyantBoussinesqSimpleFoam* also supports the thermal and buoyant studies. Hence *simpleFoam* was chosen to be the solver in this study. SIMPLE is short for Semi-Implicit Method for Pressure-Linked Equations which was developed by Spalding and his student in 1970s [13]. It has been very popular among researchers for investigating fluid flow and heat transfer problems and there are many extensive versions that were developed by the users for specific purposes. The principal behind SIMPLE is that it assumes that fluid flow moves from regions with higher pressure to regions with lower pressure. After the pressure field is initiated, each cell is evaluated based on continuity. If the mass flow that goes into the cell is not equal to the one that goes out, in the next iteration the pressure will be changed accordingly with the aim to balance the mass flow rate.

### **Segregated**

The solver formulation can be chosen from segregated and coupled. To solve the continuity, momentum and energy equations, the segregated method solves them in sequence while the coupled method resolves them at the same time. Both methods serve a large range of flow type, generally segregated approach are frequently chosen for incompressible flow and mildly compressible flows while the coupled method has an advantage for compressible flows with high velocity.

### **RANS**

As described in the first section of this chapter, Navier-Stokes equations are the fundamental equations for flow behaviour analysis and it has a great capability for solving a large range of problems. However, the velocity scales and variations make the computation very problematic. Turbulence is considered a fundamental property of fluid mechanics, whose main variables such as velocity, pressure etc. can be decoupled and modeled as fluctuations around a mean value. The most accurate method to compute the results numerically is called DNS (Direct Numerical Simulation), which resolves the entire range of turbulence fluctuations at all physical scales. A lower level of approximation is LES (Large Eddy Simulation). It is similar to DNS but only computes the turbulent fluctuations in space and time when the length scales are above a certain threshold. The turbulence that is below this threshold is named the sub-grid scale and is modeled by using semi-empirical laws. The LES computational requirement is significantly lower than DNS but it is still considerably high for flow conditions with high Reynolds number. For specific industrial applications such as combustion phenomena, using LES is considered reasonable. A comparison chart between the different methods are shown in Figure 3.8. The most widely applied method in CFD industrial practice is named Reynolds-Averaged Navier-Stokes Equations (RANS) and it has greatly simplified the original calculation by only calculating the turbulent-averaged flow over the complete spectrum of turbulent fluctuations as shown in equations 3.23, 3.24 and 3.25 [14]. It aims to create time-averaged laws of motion that remove the effect of turbulent fluctuations.

$$\frac{\partial U}{\partial t} + \text{div}(UU) = -\frac{\partial P}{\rho \partial x} + \nu \text{div}(\text{grad}(U)) + \frac{1}{\rho} \left[ \frac{\partial(-\rho \overline{u'^2})}{\partial x} + \frac{\partial(-\rho \overline{u'v'})}{\partial y} + \frac{\partial(-\rho \overline{u'w'})}{\partial z} \right] \quad (3.23)$$

$$\frac{\partial V}{\partial t} + \text{div}(VU) = -\frac{\partial P}{\rho \partial y} + \nu \text{div}(\text{grad}(V)) + \frac{1}{\rho} \left[ \frac{\partial(-\rho \overline{u'v'})}{\partial x} + \frac{\partial(-\rho \overline{v'^2})}{\partial y} + \frac{\partial(-\rho \overline{v'w'})}{\partial z} \right] \quad (3.24)$$

$$\frac{\partial W}{\partial t} + \text{div}(WU) = -\frac{\partial P}{\rho \partial z} + \nu \text{div}(\text{grad}(W)) + \frac{1}{\rho} \left[ \frac{\partial(-\rho \overline{u'w'})}{\partial x} + \frac{\partial(-\rho \overline{v'w'})}{\partial y} + \frac{\partial(-\rho \overline{w'^2})}{\partial z} \right] \quad (3.25)$$

where U, V and W refer to mean velocity;  $u'$ ,  $v'$  and  $w'$  represent velocity fluctuations. For most industrial applications, the details of the turbulent fluctuations are unnecessary to resolve therefore RANS has been a very popular choice among engineering companies. It requires the least computational effort and obtains a reasonably accurate flow calculation. It has been observed that the velocity fluctuation adds additional stresses on the fluid and they are named Reynolds stresses as shown in equation (3.26) and (3.27). The relationship between the Reynolds stresses and the mean flow quantities are unknown, hence it leads to the introduction of models that connect these two parameters and close the system of mean flow equations. These models are called the turbulence models.

Normal Stresses:

$$\gamma_{xx} = -\rho \overline{u'^2} \quad \gamma_{yy} = -\rho \overline{v'^2} \quad \gamma_{zz} = -\rho \overline{w'^2} \quad (3.26)$$

Shear Stresses:

$$\gamma_{xy} = \gamma_{yx} = -\rho \overline{u'v'} \quad \gamma_{yz} = \gamma_{zy} = -\rho \overline{v'w'} \quad \gamma_{xz} = \gamma_{zx} = -\rho \overline{u'w'} \quad (3.27)$$

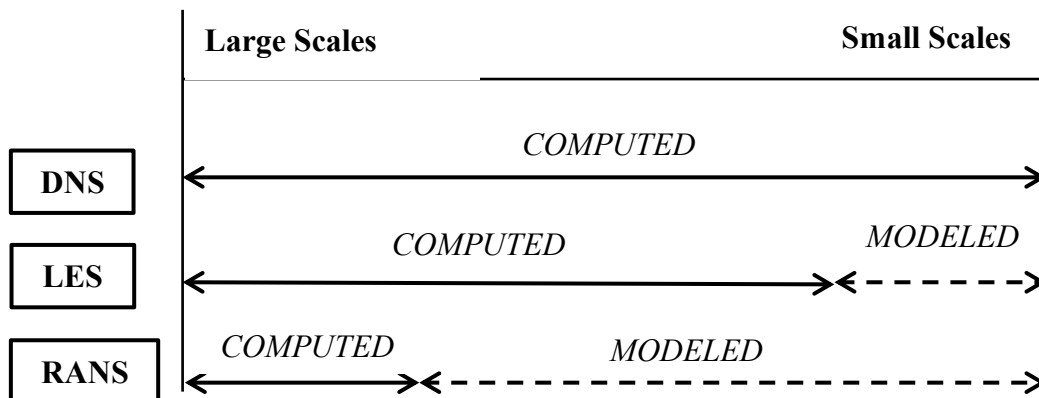


Figure 3.8: Comparisons of DNS, LES and RANS

## Turbulence Model

Frequently the turbulence models are classified based on the number of additional transport equations that need to be resolved. Some common turbulence models are listed in Table 3.3.

Number of Extra Transport Equations	Turbulence Model
Zero	Mixing-length model
One	Spalart-Allmaras model
Two	k- $\epsilon$ model (Standard, RNG, Realizable)
	k- $\omega$ model (Standard, SST)
	Algebraic stress model
Seven	Reynolds stress model

Table 3.3: RANS turbulence models

Among the above turbulence models, k- $\epsilon$  model has been widely applied in industrial computations because of its robustness and reasonable computational cost; besides, its calculation is MORE stable and the results are relatively accurate. The k- $\epsilon$  model mainly relies on the mechanisms that influence the turbulent kinetic energy k. For a turbulent flow, the instantaneous energy k is the sum of the mean kinetic energy K and the turbulent kinetic energy  $k'$ , where

$$K = \frac{1}{2} (U^2 + V^2 + W^2) \quad (3.28)$$

$$k' = \frac{1}{2} (\overline{u'^2} + \overline{v'^2} + \overline{w'^2}) \quad (3.29)$$

$$k = K + k' \quad (3.30)$$

To facilitate with the upcoming calculations, the rate of deformation  $s_{ij}$  is written as below, and the stress  $\tau_{ij}$  in tensor form was demonstrated in equation (3.4).

$$s_{ij} = \begin{bmatrix} S_{xx} & S_{xy} & S_{xz} \\ S_{yx} & S_{yy} & S_{yz} \\ S_{zx} & S_{zy} & S_{zz} \end{bmatrix} \quad (3.31)$$

The rate of deformation of fluid elements can be decomposed to the sum of the mean and fluctuating components as shown below,

$$s_{ij} = S_{ij} + s'_{ij} \quad (3.32)$$

The standard k-ε model is composed of two equations. The meaning of each term in the equation respectively represents rate of change of k or ε, transport of k or ε by convection, transport of k or ε by diffusion, rate of production of k or ε and rate of destruction of k or ε. A dimensionless constant  $C_\mu$  is defined first and the eddy viscosity is specified as following.

$$\mu_t = \rho C_\mu \frac{k^2}{\varepsilon} \quad (3.33)$$

$$\frac{\partial(\rho k)}{\partial t} + \text{div}(\rho k \mathbf{U}) = \text{div} \left[ \frac{\mu_t}{\sigma_k} \text{grad } k \right] + 2\mu_t S_{ij} S_{ij} - \rho \varepsilon \quad (3.34)$$

$$\frac{\partial(\rho \varepsilon)}{\partial t} + \text{div}(\rho \varepsilon \mathbf{U}) = \text{div} \left[ \frac{\mu_t}{\sigma_\varepsilon} \text{grad } \varepsilon \right] + C_{1\varepsilon} \frac{\varepsilon}{k} 2\mu_t S_{ij} S_{ij} - C_{2\varepsilon} \rho \frac{\varepsilon^2}{k} \quad (3.35)$$

## Monitoring Functions

In order to assist with post-processing, a few functions are added into the case setup to monitor the flow properties. For the MRF test bench simulations, Volume Report and Surface Report are included. Volume Report monitors the volumetric data of the domain. It computes the minimum, maximum, volume weighted average and standard deviation values for the prescribed mesh volume region that the user defined. Specific fluid properties can be selected or added by the user such as  $y^+$ , shear stress, total pressure. In addition, it lets the user visualize where the maximum or minimum value of a monitored flow property occurs in the domain. Surface report calculates and presents the area or flux averaged values at each time step for a boundary region, surface patch or a user-defined surface. It is also able to compute the volumetric flow rate for

incompressible flow. A few measuring planes that are parallel to the fan were included and placed at different locations in the tunnel in order to monitor the pressure rise across the fan as shown in Figure 3.6. An additional measuring plane was placed in the orthogonal direction of the fan system plane, which cuts the fan in half. This plane is used to observe the velocity vector pattern near the fan blade in a vertical direction and later can be used to compare with the velocity field that is created using Actuator Disk method. The pressure is monitored on the inlet patch and outlet patch as well to help understand the pressure distribution in the simulation domain.

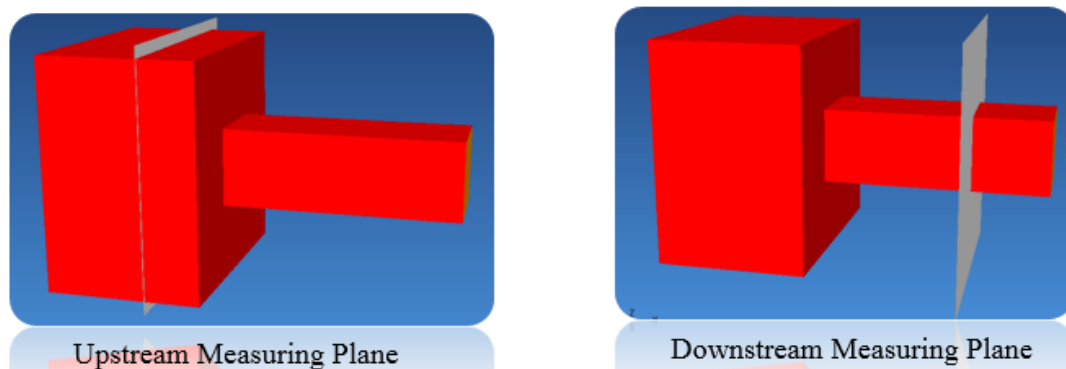


Figure 3.9 Measuring planes from surface reports

### 3.5 Results & Discussions

With the mesh and boundary layer settings mentioned in the previous section, the resulting mesh is comprised of approximately 17.88 million cells, and ninety percent of the total cells are hexahedral. To ensure the mesh size is appropriate, an investigation was conducted to check the sensitivity of the simulation solutions in regard to the size of the mesh. The baseline mesh on the fan system has a mesh size of around 1.5cm, which gives a relatively precise modeling of the fan geometry. Feature lines of the fan blade, hub, motor and shroud were extracted in order to capture the detailed outline of the geometry so that the boundary layers can be better generated. The boundary layer on the blade was successfully generated with coverage of over 99 percent.

To simulate the fan test bench model with a coarser mesh, a new mesh was set up with the aim to decrease the total cell number by half. The mesh size of the fan components was increased to 2cm and the final mesh contained a total cell number of 12.8 million. The post-processing of the mesh was conducted in Paraview and the visualization of the fan components indicated that at many locations the mesh was badly generated especially on the edge and middle of the blade, therefore, the boundary layers near these cells failed to create. The pressure rise appeared to decrease by approximately 7 percent compared to the baseline simulation, and the percentage error compared to the test data increased to 19.38% from 13.88%.

For a more refined mesh, the mesh size of the fan components was decreased to 1cm, and the total cell number became about 34.98 million of which 84% is composed of hexahedral cells. The details of the fan components geometry were better represented and the boundary layers on the blade achieved 99.6%. The pressure rise across the fan increased less than 1% comparing to the baseline simulation, which could be considered negligible. The velocity gradients appear to be the same as the baseline simulation. Although the geometry is meshed with a higher quality, the results are on the same level of accuracy as the baseline model. Therefore, in order to save computational cost, the baseline model with around 17.88 million cells was chosen to be used in this project based on its reasonable computational capacity and accuracy.

	<b>Coarse</b>	<b>Baseline</b>	<b>Fine</b>
<b>Number of Cells</b> (Million)	12.8	17.88	34.98
<b>Pressure Rise</b> (percentage compared to baseline)	93%	100%	100.62%
<b>Error Percentage</b> (compared to test data)	-19.38%	-13.88%	-14.41%

Table 3.4: Grid independence study

Using the above baseline mesh settings, the simulations were set up and run on ten operating points with various volumetric flow rates and fan rotating speeds that were

provided by the fan testing facility. The volumetric flow rate and pressure rise values that are presented in this thesis have been normalized due to confidentiality. The pressure rise across the fan is calculated by subtracting the downstream pressure from the upstream pressure, therefore the downstream pressure and upstream pressure need to be measured. For the upstream pressure, the simulation results showed that the pressure at any location of the upstream does not vary significantly, so the value of the upstream pressure can be chosen to use any data from the upstream measuring planes as long as it is placed between the inlet and the fan. Since the fan facility did not provide the exact location of where the pressure tap was located in the testing tunnel, the location of the measuring plane at downstream needs to be decided. The simulation results showed that the downstream pressure in the tunnel is more sensitive to the location of the measuring plane. For the operating points with low volumetric flow rate such as the first five operating points, the pressure difference in the tunnel at different locations is relatively small, less than 1 Pascal; hence in this region, the downstream pressure value can be measured using any measuring plane that is placed between the fan and the outlet. However, when the volumetric flow rate increases to a relatively higher value, the pressure difference between the measuring plane which is placed close to the fan and the outlet can go up to around 5 Pascal. To accurately present the pressure rise across the fan, the pressure rise is represented by a range with two values; one is the minimum (green plot) which is measured as the measuring plane that is placed at around 50cm downstream to the fan and the other one is the maximum (blue plot) which is measured at the outlet. The normalized pressure rise of the test and the simulation results are shown in Table 3.5 and Figure 3.10.

	1	2	3	4	5	6	7	8	9	10
$\Delta P_{\text{Test}}$	1	0.88	0.76	0.63	0.51	0.38	0.25	0.13	0.00	-0.21
$\Delta P_{\text{Outlet}}$	0.91	0.76	0.59	0.48	0.38	0.28	0.15	0.05	-0.06	-0.24
$\Delta P_{\text{Plane}}$	0.91	0.76	0.59	0.48	0.38	0.26	0.13	0.02	-0.09	-0.27

Table 3.5: Pressure rise comparison between test data and OpenFOAM simulation results

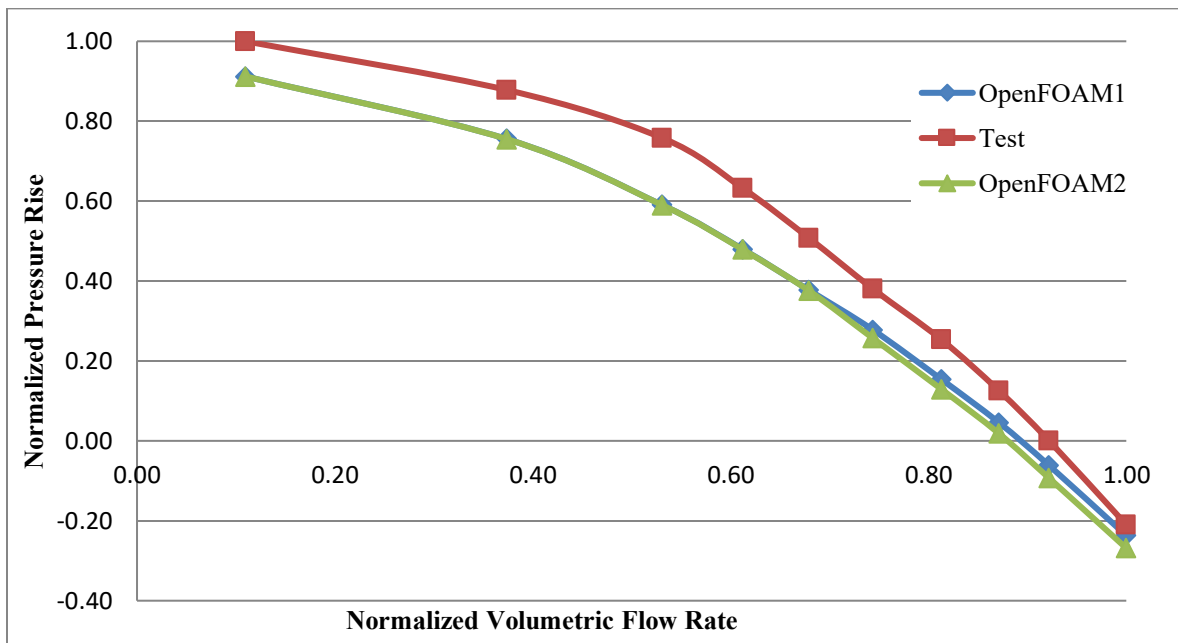


Figure 3.10: Plots for comparison between pressure rise vs. volumetric flow rate between test data and OpenFOAM

The simulation results show that the MRF fan model in OpenFOAM underestimates the pressure rise across the fan which complies with the conclusions from the previous literature review. When the volumetric flow rate is lower, the MRF fan model is less accurate due to the significant influence of the fan. While as the volumetric flow rate increases, the pressure rise becomes more and more accurate comparing to the test data since the fan has less effect on the system. Comparing to other software as displayed in Figure 3.11, the red solid line represents the simulation results from

OpenFOAM. It is quite similar to the behaviour of the MRF model in Star-CCM+, both underestimate the pressure rise throughout the entire volumetric flow rate range but the trends of the plot are consistent with the test data. When the volumetric flow rate is lower, the pressure rise from these two software packages are almost the same, as the volumetric flow rate increases, the accuracy of both software both increase and shift closer to the test data trend, while OpenFOAM tends to have more promising results. MRF model using ACE+ appears to have an opposite behaviour which is very accurate when the flow rate is low but then turns to be very unreliable at higher volumetric rates which shows significant low-pressure rise comparing to the test results. Overall, by modeling the MRF fan model using the same geometry, OpenFOAM appear to be able to provide a very promising result comparing to other commercial CFD software.

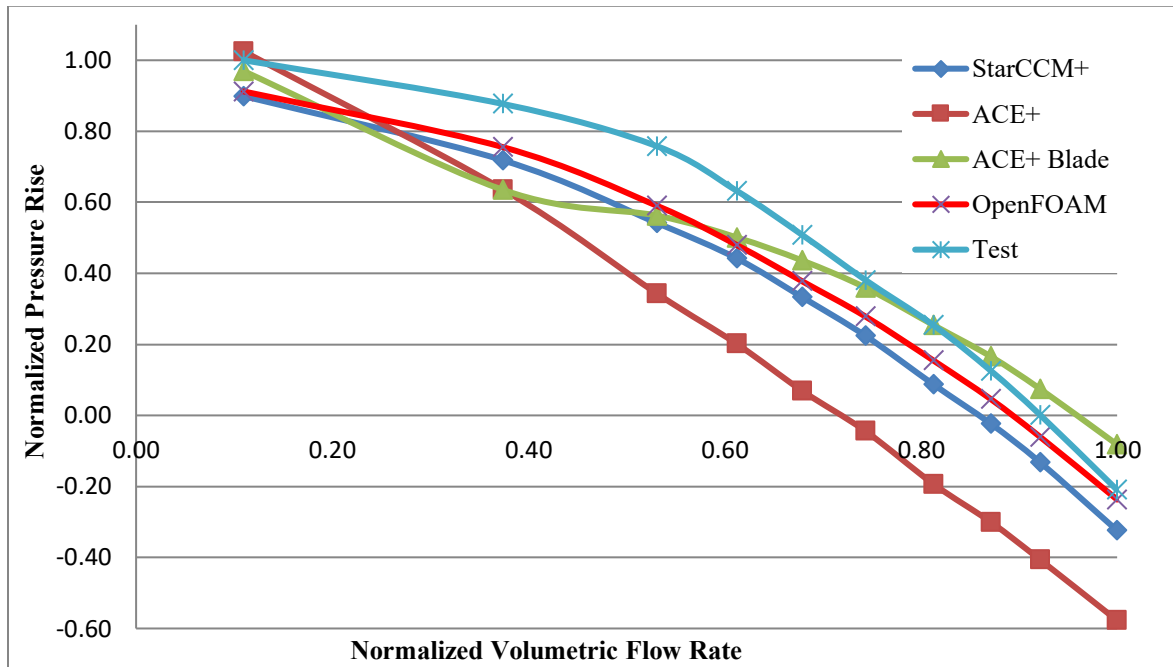


Figure 3.11: Plots for comparisons between OpenFOAM and other commercial software

The following two graphs are two cut planes, at 100mm upstream of the fan and 25mm downstream of the fan. The planes are colored with the pressure data and the vector indicates the tangential velocity distribution and its color represents the velocity magnitude. One can observe that at the upstream region the airflow tends to flow towards

the middle without obvious swirls. The pressure seems evenly distributed with a slightly lower value in the middle but the difference between the maximum and minimum pressure is still less than one Pascal. The velocity magnitude is quite small, under 1 m/s, and the velocity tends to increase towards flowing into the middle. At the downstream plane, after the airflow passes through the fan, a swirl forms in the middle of the tunnel with a direction which complies with the rotational direction of the fan. Higher velocity occurs near the tip of the blades and the pressure distribution is a slightly more chaotic but the pressure difference is quite small, under 3 Pascal. Figure 3.14 and 3.15 show the pressure distribution and velocity magnitude in x, y and z directions on a cut plane downstream close to the fan.

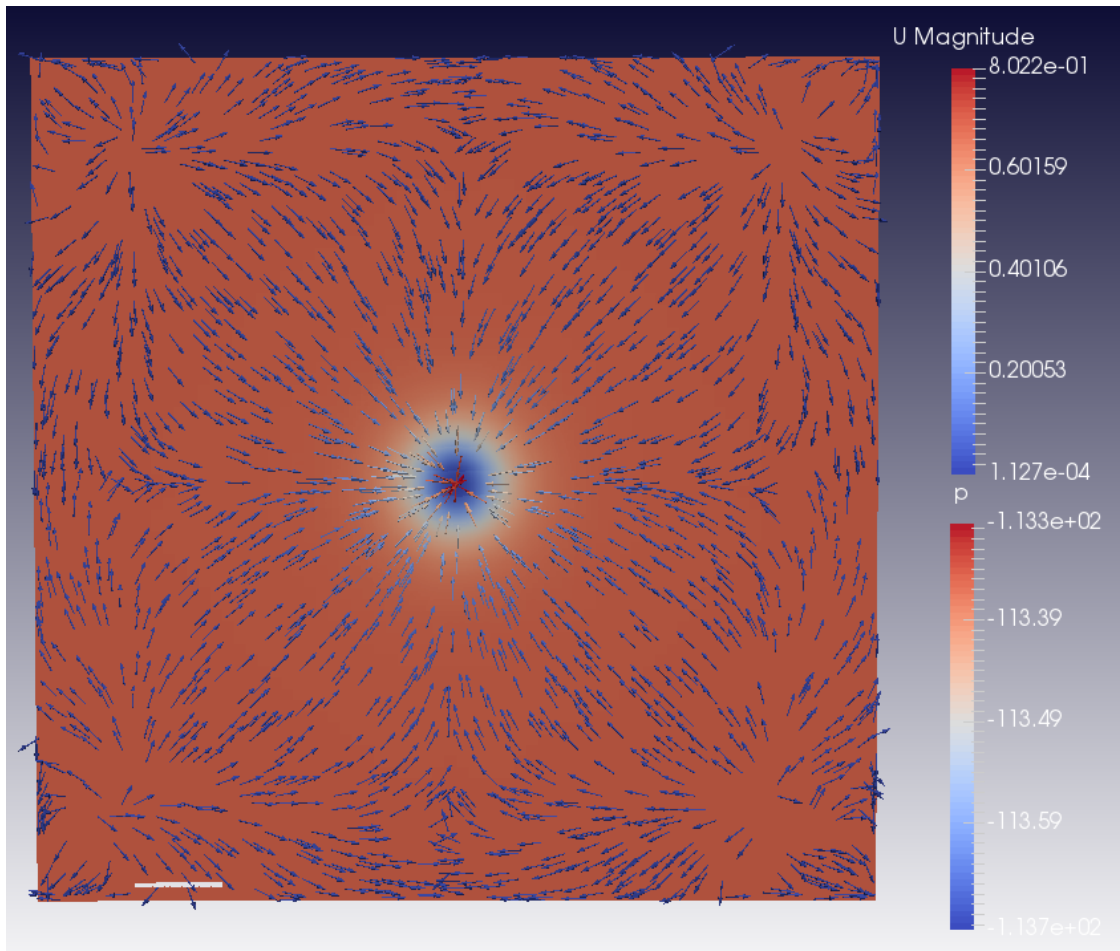


Figure 3.12: Cut plane at 100mm upstream from the fan

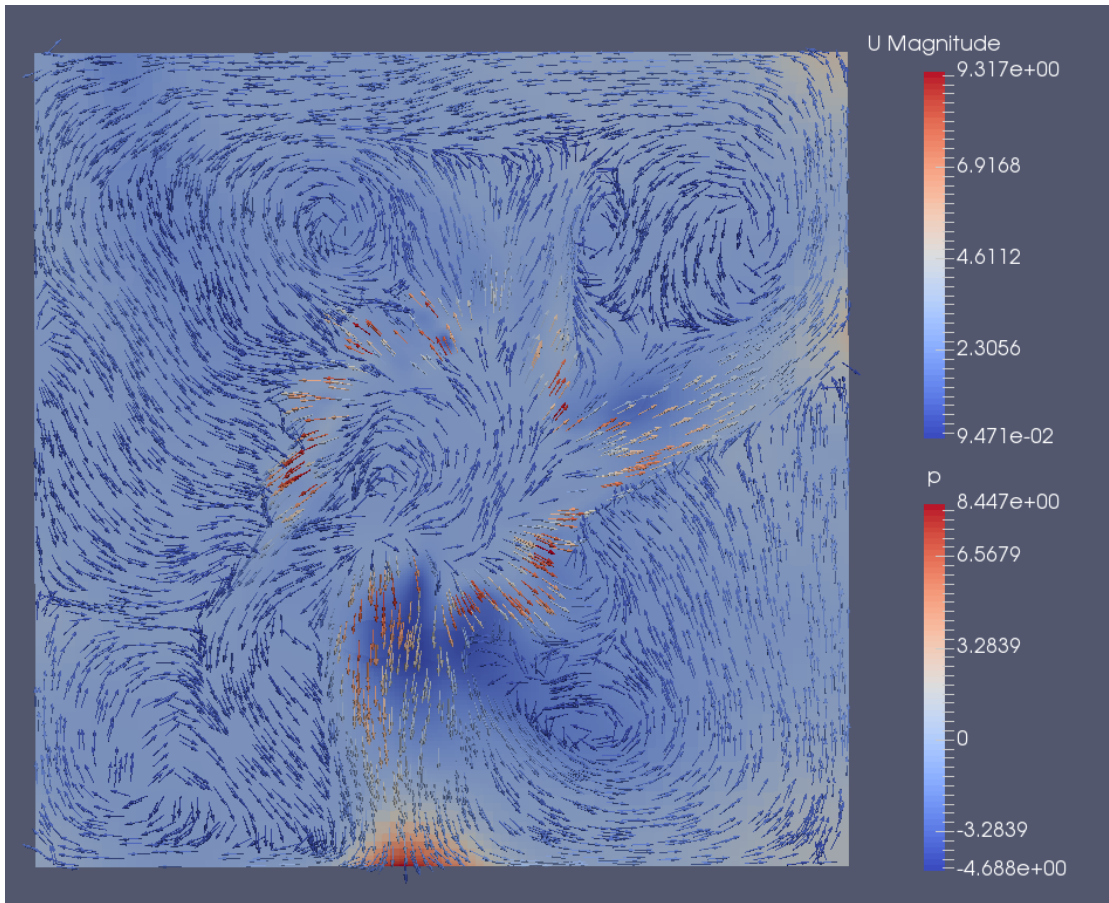


Figure 3.13: Cut plane at 25mm downstream from the fan

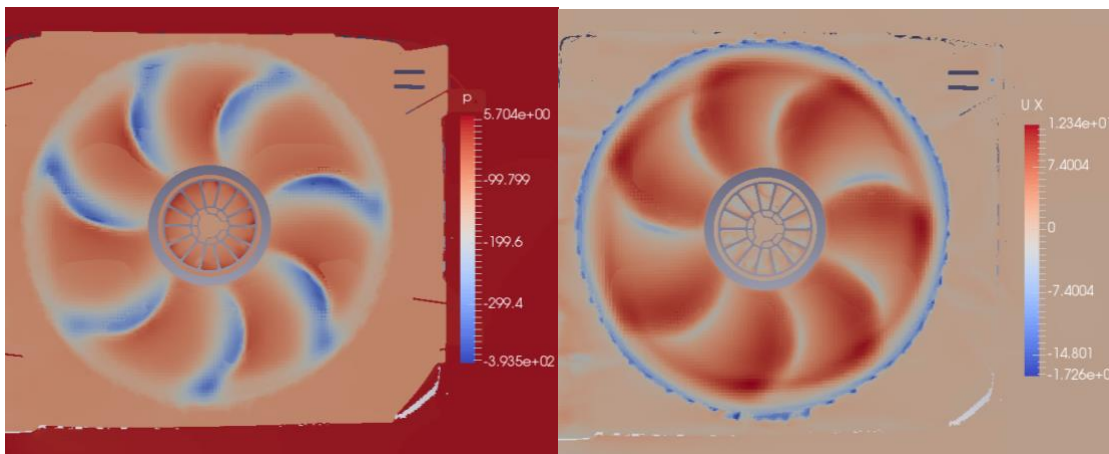


Figure 3.14: Pressure distribution on the fan; velocity distribution in x-direction on the fan

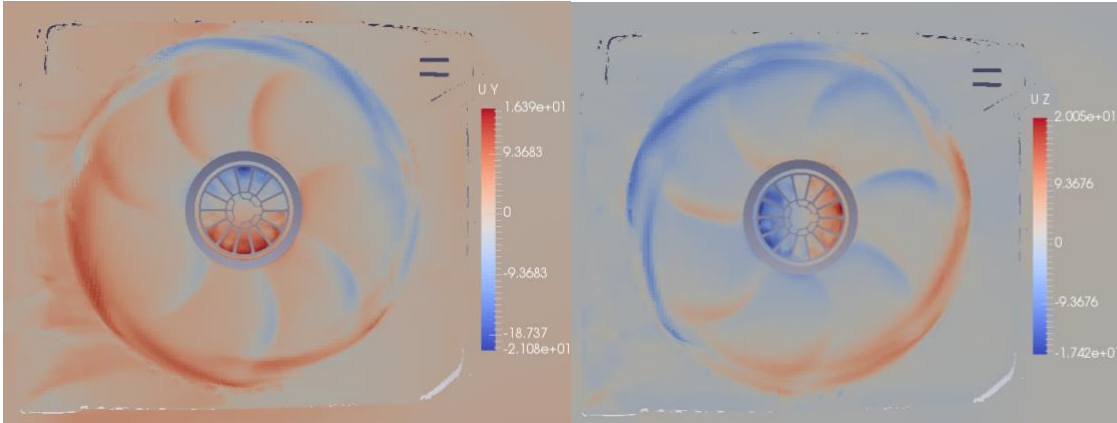


Figure 3.15: Velocity distribution in y-axis and z-axis on the fan

### 3.5.1 Changing MRF Domain

From the literature review, it has been shown that the MRF domain has a significant influence on the pressure rise across the fan. Therefore, this project has included an investigation of various sizes of MRF domain. However, the domain of MRF region is very constrained due to the existence of the shroud. The shroud is very closely positioned outside of the MRF domain with a very small clearance, especially in the radial direction, the diameter of the MRF is not able to be increased any larger or it would interfere with the shroud. Figure 3.16 shows the original MRF domain that was provided for standard MRF simulations. The green region represents the MRF domain and the yellow part is the fan shroud. Thus, this study will not investigate the effect of various diameters of the MRF on pressure increase; the adjustments on the MRF domain are along the axial direction only. Domain A extends the original domain 3mm in the positive x direction. 3mm is the maximum length that could be extended before it obstructs the front face of the shroud. Domain B extends the original domain in the negative x direction by 10mm where it reaches the same surface of the back face of the shroud as shown in Figure 3.17.

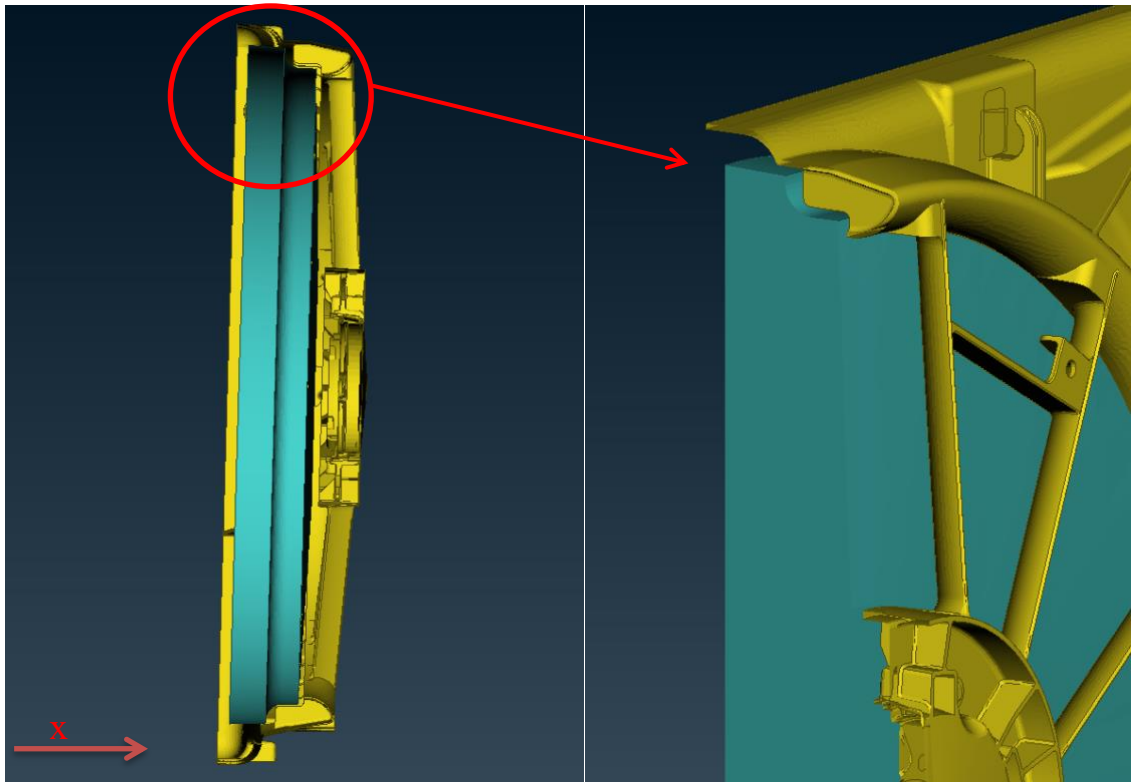


Figure 3.16: Original geometry of MRF domain

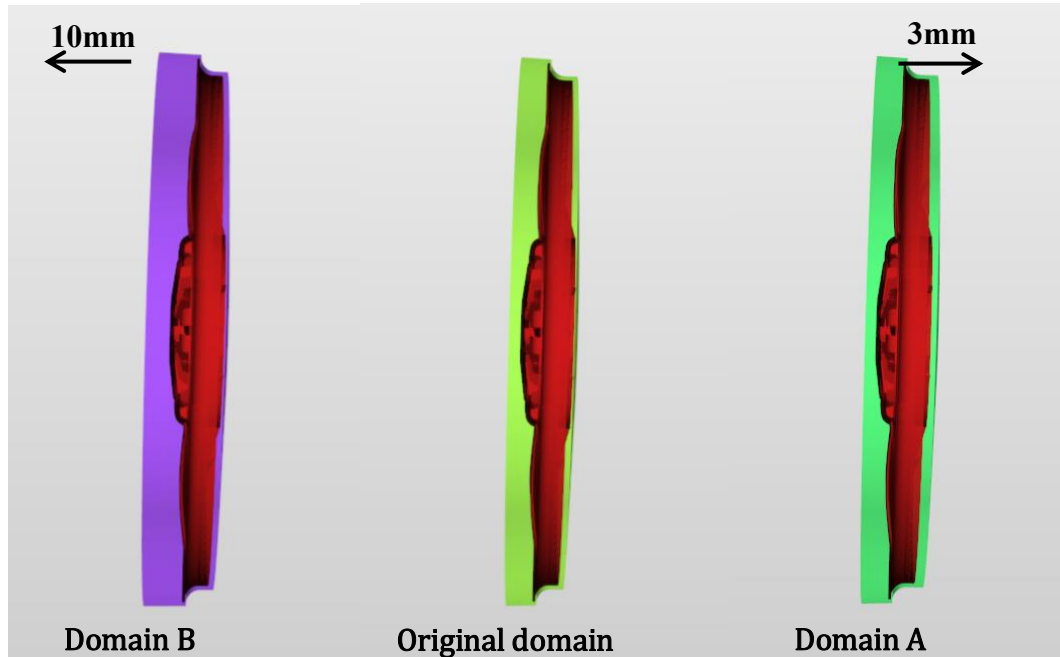


Figure 3.17: Illustrations of domain B, original and domain A geometries

By replacing the MRF original domain with the domain A and domain B shown above, the corresponding pressure rises at five operating points were recorded and plotted in Figure 3.18 together with test data and original simulation results for comparison purpose. The percentage error of each case comparing to the test data is listed in Table 3.6. As indicated in the plots and the table, one can observe that both domain A and domain B improved the accuracy of the results although the change of the domain is very small. The result of domain A appears to be even more promising than domain B even though domain A was only extended 3mm in the axial direction. The pressure rise at high flow rates are very accurate using the new domains, where the error comparing to the test data is less than 2%.

	1	2	3	4	5
Original MRF Domain	-8.79%	-13.98%	-24.12%	-39.20%	12.86%
MRF Domain A	-3.53%	-10.21%	-16.52%	-25.53%	1.51%
MRF Domain B	-5.19%	-13.12%	-18.74%	-29.83%	-1.25%

Table 3.6: Percentage error between different domains from test data

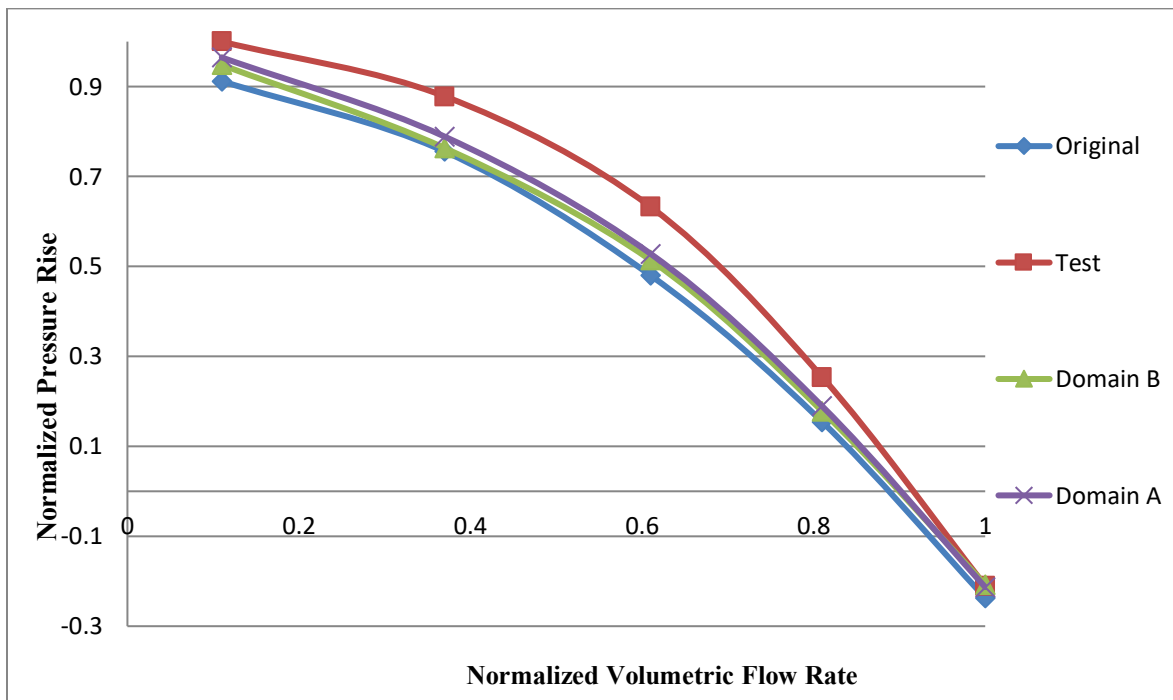


Figure 3.18: MRF pressure rise vs. volumetric flow rate comparisons of various domains

### 3.5.2 Changing Upstream Boundary Condition

As mentioned in the previous section, the upstream box geometry and the downstream tunnel geometry were provided in one stl. file, hence as one part, the boundary condition cannot be assigned with different properties and both of these regions were defined as no-slip solid wall. In order to study the effect of slip and no-slip boundary conditions on the system and optimize the accuracy of the model, the geometry was separated into two parts: upstream box and downstream tunnel as shown in Figure 3.19. Therefore, different boundary conditions could be applied separately to the two regions. The upstream box is defined as slip-wall since it is a numerical boundary for simulation purpose. It is not the actual physical boundary of the experimental lab. The downstream tunnel remains as no-slip wall since it models the actual dimensions of the test tunnel. The pressure rises at five operating points with the new boundary condition were plotted in Figure 3.20 along with the original setup results and test data for comparison purposes. The graph shows that the pressure rise is nearly the same as the original case which is not influenced by the modified boundary condition. The reason could be that in the upstream region the velocity is very small near the wall so the difference between no-slip and slip conditions is negligible. Figure 3.21 displays the velocity magnitude distribution on a cut plane upstream at the same location in both cases. One can observe that the velocity is very small in the entire region less than 0.035m/s near the wall.

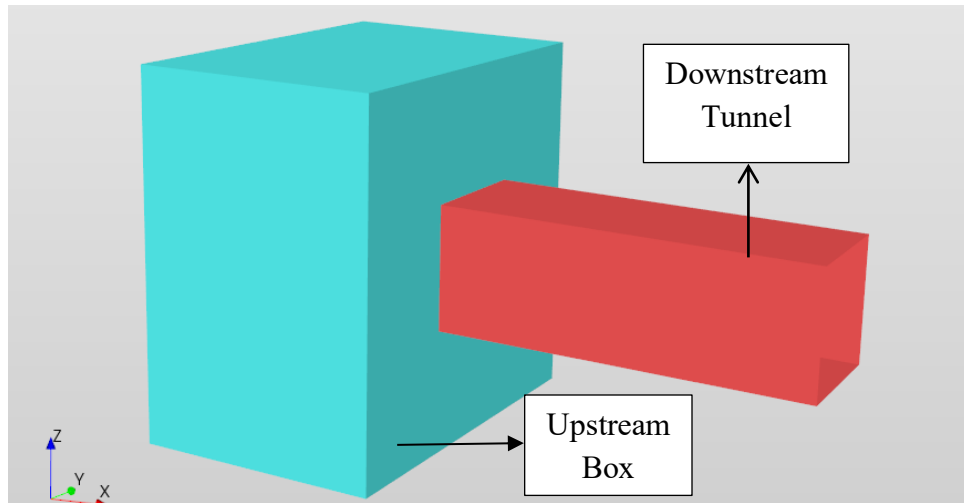


Figure 3.19: Upstream box and downstream tunnel illustration

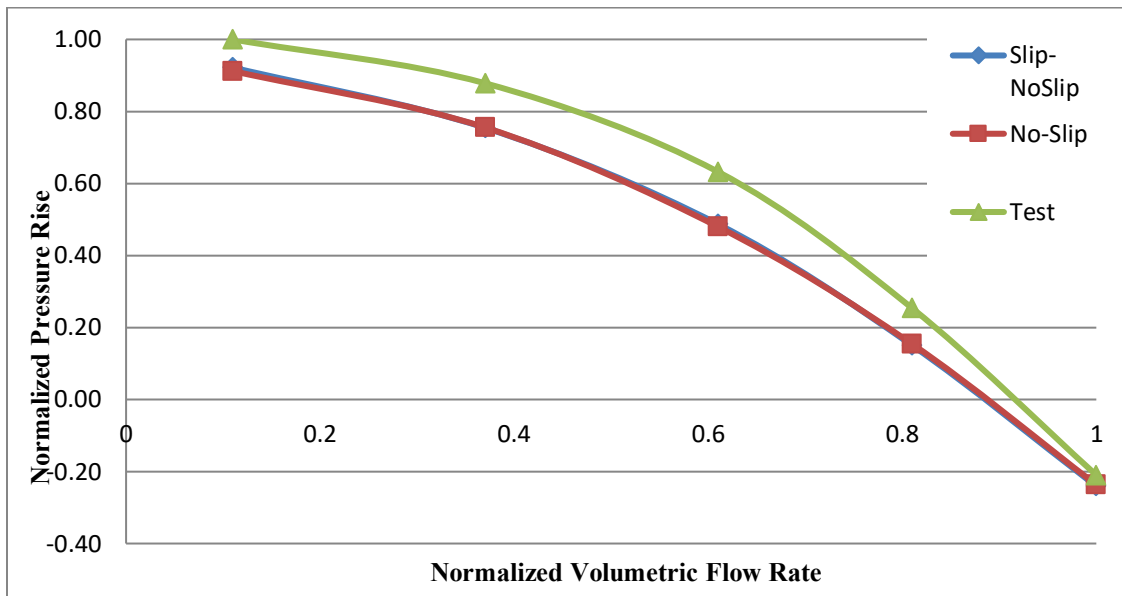


Figure 3.20: Pressure rise vs. volumetric flow rate between no-slip and slip upstream boundary conditions

	1	2	3	4	5
Normalized Pressure Rise No-Slip	0.91	0.76	0.48	0.15	-0.24
Normalized Pressure Rise Slip+No-Slip	0.92	0.75	0.49	0.15	-0.24

Table 3.7: Normalized pressure rise data of no-slip and slip upstream boundary conditions

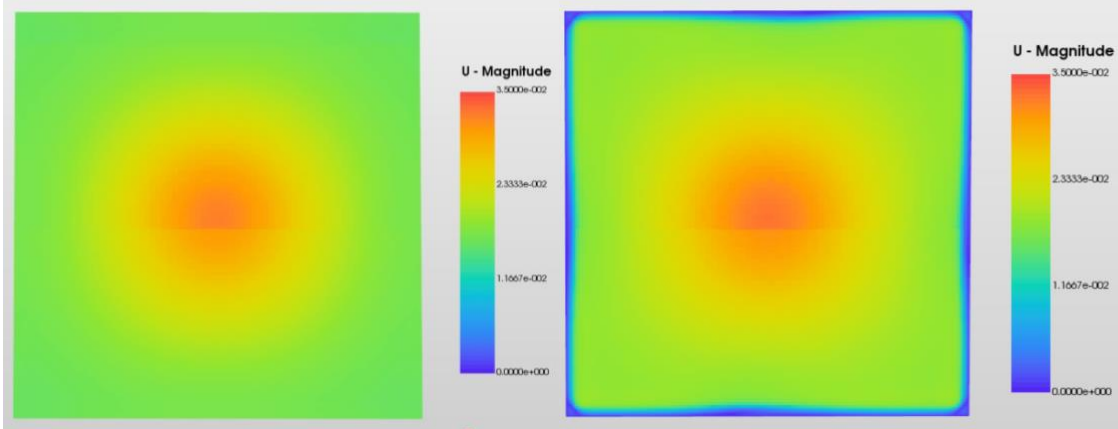


Figure 3.21: Velocity distribution on a cut plane upstream between slip and no-slip boundary conditions

### 3.5.3 Changing the Upstream Volume

This section aims to study the influence of the upstream volume on the pressure rise across the fan. Unlike the downstream tunnel which describes the actual physical geometry, the upstream box does not represent the real physical boundary. The dimension of the upstream geometry is a user-defined numerical simulation boundary which intends to model the equivalent domain. The side of the original upstream domain is approximately 5.5 meters long. The domain C extends from the original domain 1-meter-long in all three directions and domain D is the opposite, which shortens the length of the geometry in every direction by one meter as shown in Figure 3.22. Domain E has the same dimension of the side, but in the axial direction (x-axis) it remains the same as the original domain to investigate the influence of the upstream domain length in axial direction.

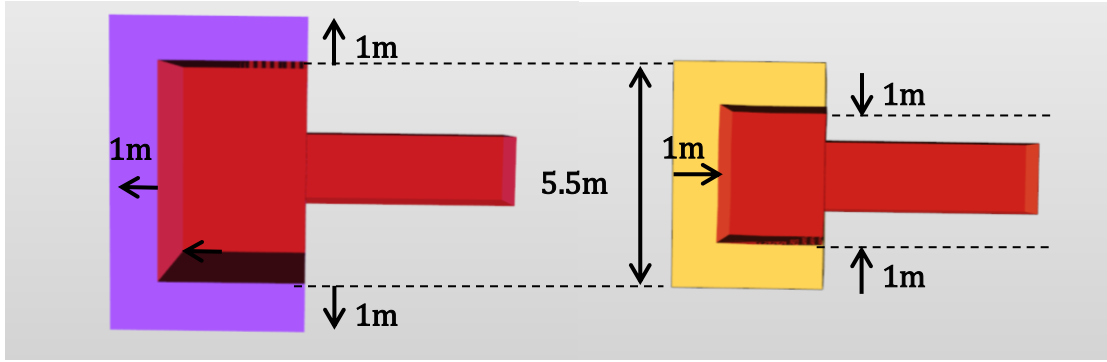


Figure 3.22: Domain C (larger domain) & Domain D (smaller domain)

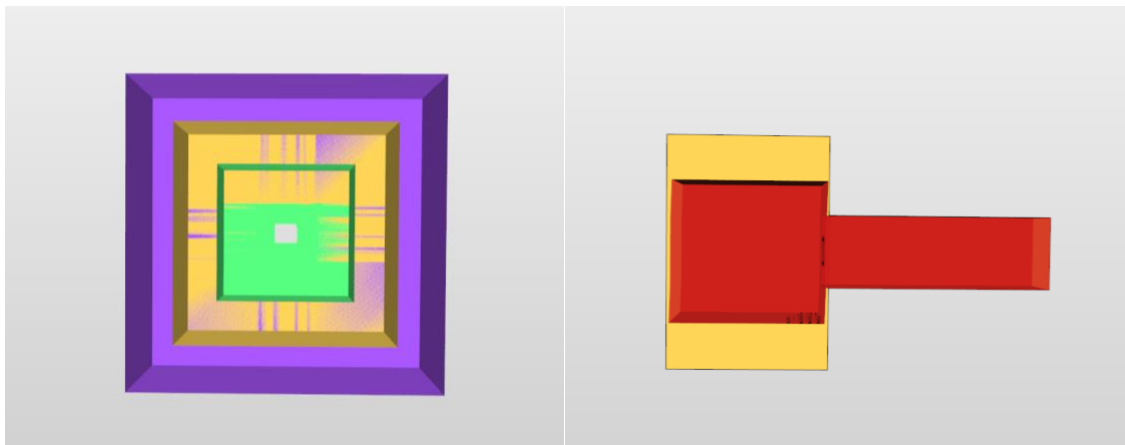


Figure 3.23: Comparisons of three domains in y-z plane; Domain E

The pressure rise across the fan in each domain is listed as below. The results show that the upstream domain has a very small influence on the pressure rise. Hence the provided geometry of the upstream box has a very reasonable dimension. The airflow velocity in the upstream region is relatively very small and the airflow behaviour tends to be stable without extreme irregularities, therefore the domain of the upstream box does not change the flow pattern as much as it would in the downstream region when the inlet flow rate is relatively lower. When the inlet flow rate increases, it could be observed that the two smaller domains possess a higher accuracy than the larger domain and the original MRF domain.

Airflow Rate	Pressure Rise Test	Original	Pressure Rise Domain C	Pressure Rise Domain D	Pressure Rise Domain E
0.11	1	0.91	0.89	0.90	0.92
0.37	0.88	0.76	0.76	0.76	0.76
0.61	0.63	0.48	0.48	0.49	0.49
0.81	0.25	0.15	0.14	0.17	0.17
1	-0.21	-0.24	-0.26	-0.22	-0.22

Table 3.8: Pressure rise of different domains

## CHAPTER 4 FULL VEHICLE MODELING

### 4.1 Background

After investigating the performance of isolated MRF fan model in OpenFOAM as illustrated in the previous section, this chapter aims to validate the MRF technique in a full vehicle model since test bench fan model alone cannot represent the entire cooling system performance truthfully. Previously, experiments on full vehicles were conducted in the aero-acoustic wind tunnel as illustrated in Figure 4.1 with an approximate dimension of  $5\text{m}\times 7\text{m}\times 22\text{m}$  and the vehicle was placed at about 5 meters behind the inlet patch. Propeller anemometers were mounted in front of the radiator and the airflow rate was measured. The experiment was conducted at seven operating points with various vehicle speeds and fan rotating speed and the volumetric flow rate in front of the radiator was recorded at each case. These values are used to validate the level of accuracy from simulation results and therefore help measure the CFD computation capability of OpenFOAM.

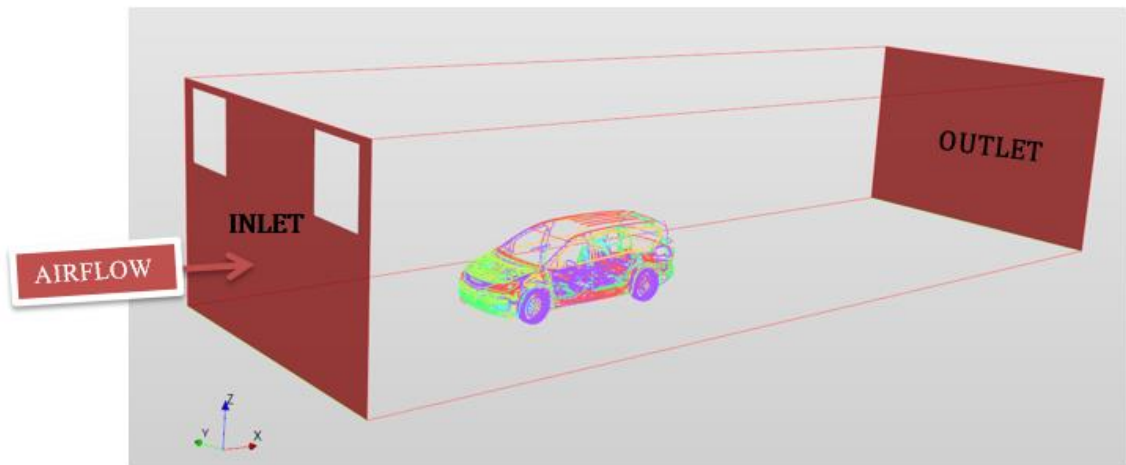


Figure 4.1: Experimental setup illustration

ACE+ has been widely used for full vehicle simulations and a popular fan modeling technique is called Fan Blade Model. It requires the input of the averaged blade angle, the rotational speed of the fan. The local thrust and torsional forces that were

imposed on the flow by the fan then are able to be computed. Also, the body forces are calculated and included in the source terms for the momentum equations. The forces that are exerted on the airflow by the fan are assumed to be in axial and circumferential directions only, therefore it is considered as a two-dimensional model where the geometry is symmetrical around the axis. A simplified configuration is shown in Figure 4.1, where  $F_x$ ,  $F_\theta$  represent fan forces in axial, circumferential direction respectively and  $F_n$  is the force along the normal direction to the fan blades.  $\theta$  is the blade angle.

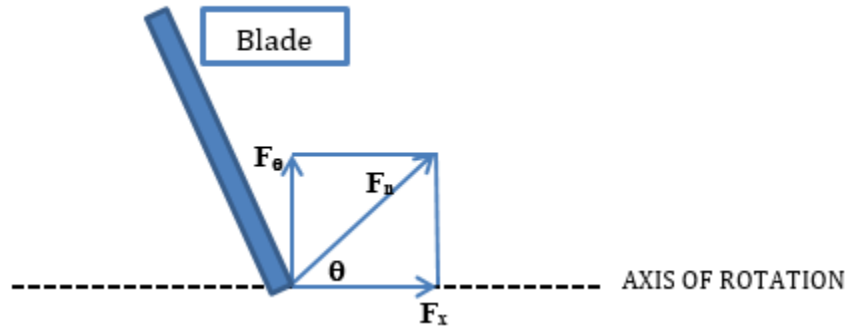


Figure 4.2: Fan blade model mathematical simplified configuration

The normal force which was exerted on the airflow by the blade is written as below, where  $m$  stands for the amount of mass that was displaced by the fan blades in its orthogonal direction, and the blade and airflow velocities in the same direction are noted as  $V_{bn}$  and  $V_{fn}$ .  $A_b$  represents the blade area [13].

$$F_n = m(V_{bn} - V_{fn}) \quad (4.1)$$

$$V_{bn} = r\omega \sin \theta \quad (4.2)$$

$$m = \rho A_b V_{bn} \quad (4.3)$$

Once the normal force is computed, the forces in axial and circumferential directions can be calculated as follows and are to be inserted into the source term.

$$F_x = F_n \cos \theta \quad (4.4)$$

$$F_\theta = F_n \sin \theta \quad (4.5)$$

This fan modeling technique neglects the flow that passes through the fan tip radially and the resistance from the blockage effect of the fan blades. In addition, since the actual

geometry is not modeled, and to minimize the inaccuracy it causes, usually, a correction factor is specified by the user. The previous correction factor that was used for full vehicle simulation is defined in Equation (4.6), where blade frontal area refers to the total surface area of the blades in the axial direction and annular area represents the entire surface area between the fan ring and fan hub.

$$Fan\ Factor = \frac{Blade\ Frontal\ Area}{Annular\ Area} \quad (4.6)$$

$$Annular\ Area = \pi(r_{fan}^2 - r_{hub}^2) \quad (4.7)$$

With the correction factor, the simulation results from ACE+ achieved a very high level of accuracy comparing to the experimental data as shown in Figure 4.3. The performance of the Fan Blade Model was improved significantly and with a regional percentage error under 5%. The simulation results from ACE+ are to be compared with OpenFOAM results as well so that the capabilities of these two software packages can be studied.

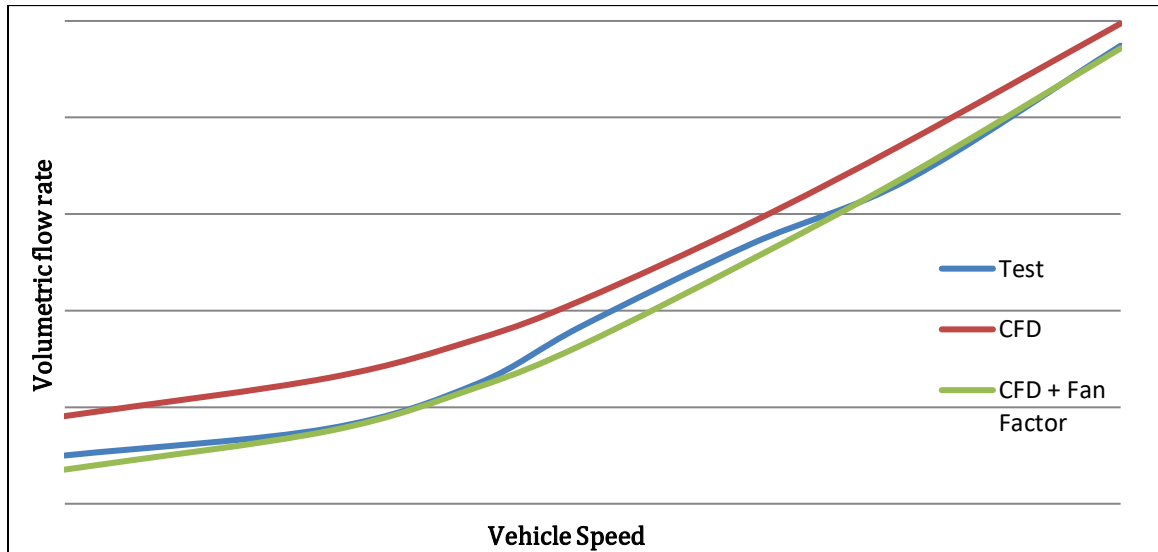


Figure 4.3: Full vehicle simulation results (airflow rate across radiator) between test and CFD

## 4.2 Heat Exchangers

The fuel generates a huge amount of heat energy when it is being burnt in the engine, but only around thirty percent of the energy is converted into power. Another thirty percent is absorbed by engine lubrication oil and lost in friction. The rest of the heat is taken away by the engine cooling system. The existence of the engine cooling system is very necessary because the parts could melt from the substantial excessive heat, and the pistons will expand due to the high temperature which leads to ‘seize’; a terminology to describe the situation when the pistons are stuck in the cylinders. To summarise, the main purpose of an engine cooling system is to keep the engine operating at an optimal temperature by removing excessive heat.

Heat exchangers refer to devices that transfer heat between two or more mediums. They are widely applied in many fields such as power stations and chemical plants. The most important heat exchanger in the engine cooling system is the radiator. In order to cool down the engine, a coolant is fed into the engine block and circulates around to absorb excessive heat. After it exits the engine block, the hot coolant then is distributed across the radiator core through tubes. Downflow and crossflow are the two basic types of radiators, and the difference is the orientation of the tubes. Downflow is when the coolant flows from the top of the core to the bottom, while crossflow is when the coolant flows from one side to the other side horizontally. When the hot coolant flows through these tubes, the heat is transferred into the air by convection. The efficiency of heat transfer is largely improved with fins because they greatly increase the area of contact surface between the coolant and the surrounding air. More heat will be exchanged into the air when the volumetric flow rate of the air increases, and this is the main purpose of the fan. It ensures that there is sufficient airflowing through the radiator all the time.

Figure 4.4 shows the major heat exchanger configuration that is used in this thesis. Except for the fan, the condenser, Transmission Oil Cooler (TOC), and radiator are not simulated using its detailed geometry. A common method for full vehicle simulation to model the heat exchanger is to define them as porous media. Before defining the properties for porous media, three simple boxes need to be created

correspondingly to TOC, condenser, and radiator based on the size of each of the above components.

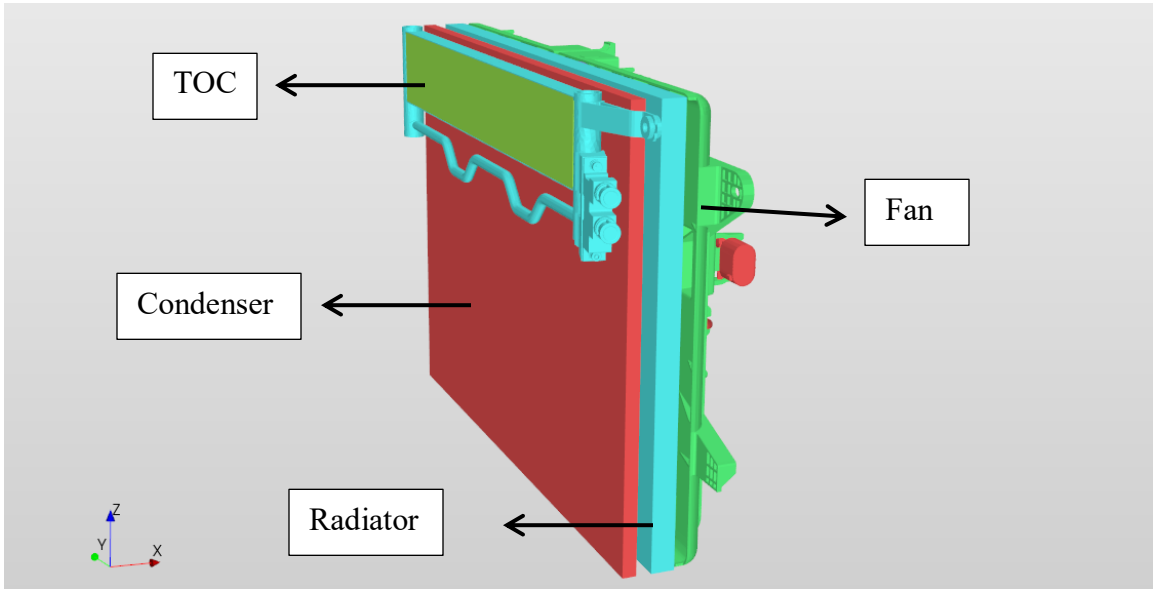


Figure 4.4: Heat exchangers

The principle of porous media is by including a volumetric source term  $S_i$  in the momentum equations. In OpenFOAM, there are two methods that could be used to define the region. In this project, Darcy-Forchheimer formula is chosen instead of the power-law approximation of the velocity. The equation of the source term  $S_i$  is shown as below. The first term on the right-hand side is known as Darcy which is the viscous loss term, the second term is named an inertial loss term.

$$S_i = - \left( \sum_{j=1}^3 D_{ij} \mu U_j + \sum_{j=1}^3 F_{ij} \frac{1}{2} \rho \bar{U} U_j \right) \quad (4.8)$$

where  $D_{ij}$  and  $F_{ij}$  are the prescribed porous media tensors;  $U_j$  is the  $j^{\text{th}}$  component of the velocity vector;  $\bar{U}$  stands for the velocity magnitude and  $\mu$  represents the dynamic viscosity of the fluid.

Similar to define MRF properties, when setting up a porous medium region, the first step is to create a cell zone using the geometry that was imported. Then, the parameters  $e_1$  and  $e_2$  need to be provided by the user. These are two orthogonal vectors that represent the x

and y axes of the local coordinate system that describe that orientations of the porous medium in a global Cartesian coordinate system.

### **Viscous Loss Coefficient (d); Inertial Loss Coefficient (f)**

Commonly, the experimental data of radiator, condenser, and TOC are provided by the supplier with the corresponding mass flow rates through the device and the pressure drops. The geometry dimensions of the heat exchangers are also provided. In order to derive the viscous loss coefficient and inertial loss coefficient, a characteristic curve needs to be created first. The y-axis uses a modified parameter which is the pressure drop per unit length  $\frac{\Delta P}{L}$ , where L represents the thickness of the porous medium region. The x-axis values are the mean velocity of the air flowing through the porous medium and it could be calculated by dividing the mass flow rate by the cross-sectional area and air density. After the curve is plotted, a polynomial quadratic fit equation can be obtained.

For example, for the radiator, the modified characteristic curve is shown as below and the trend line is derived as  $y = 107.33x^2 + 991.8x$ . Now the viscous loss coefficient d and the inertial loss coefficient f can be calculated as below. The unit of d is  $1/m^2$  and the unit of f is  $1/m$ .

$$d = \frac{991.8}{\mu} = \frac{991.8}{0.00001846} = 5.37e7 \quad (4.9)$$

$$f = \frac{107.33}{0.5 \times \rho} = \frac{107.33}{0.5 \times 1.1614} = 184.83 \quad (4.10)$$

In OpenFOAM, both of these two coefficients need to be defined in three directions. The above calculation results are to be put into the direction which aligns with the flow direction, and then the other two directions need to be input with parameters that are at least one magnitude larger. Therefore, in this case, the coefficients that are put into the OpenFOAM settings are [5.37e7, 5.37e8, 5.37e8] for viscous loss coefficient and [184.83, 1848.3, 1848.3] for inertial loss coefficient.

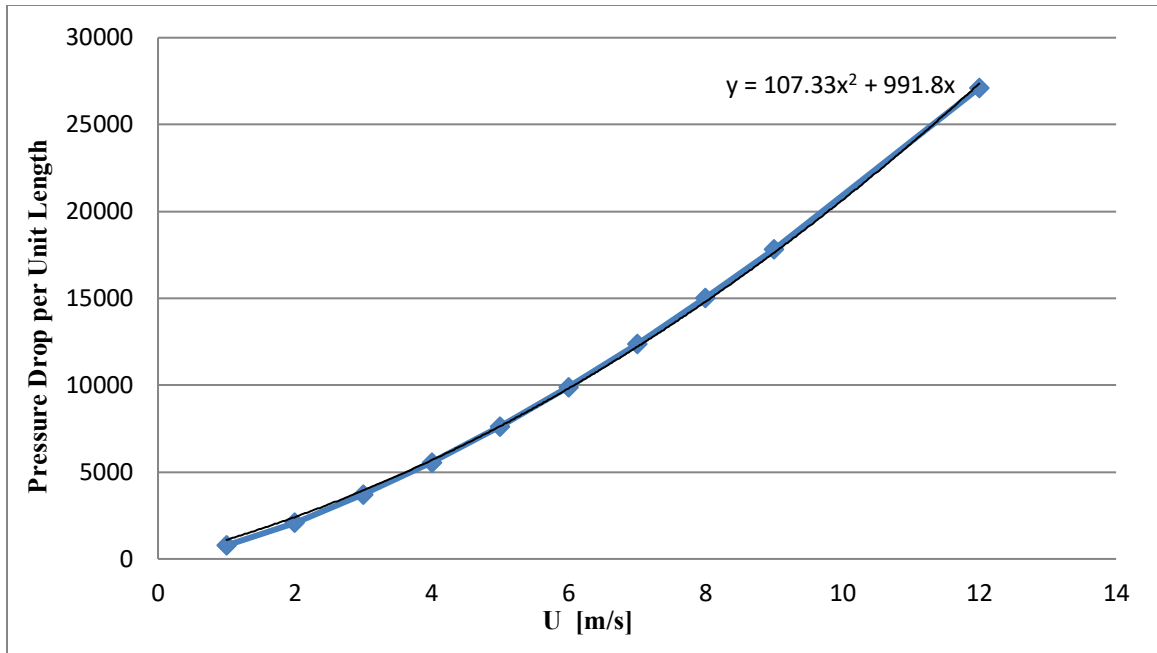


Figure 4.5: Radiator characteristic curve

By applying the above procedures also for the condenser and TOC, the coefficient of the porous medium settings can be summarized in Table 4.1.

	Polynomial Equation	Viscous loss coefficient	Inertial loss coefficient
Radiator	$y = 107.33x^2 + 991.8x$	$5.37e7$	184.83
Condenser	$y = 194.79x^2 + 869.4x$	$4.71e7$	335.44
TOC	$y = 235.41x^2 + 1609.6x$	$8.72e7$	405.39

Table 4.1: Porous medium coefficients for heat exchangers

### 4.3 Simulation Settings

Similar to setting up MRF mesh, each part in the full vehicle model is assigned with two levels of refinement which defines a range of mesh sizes for the corresponding component. The base meshing size is set to 0.3 meters and the mesh settings for the fan system remains the same as the setup in Chapter 3. For the condenser, TOC, and radiator, the mesh sizes are set to 0.002 meters. For some very detailed components such as grill texture, 1mm to 2mm are used as the mesh size range. The majority of the rest of the components are set up a mesh size range from 0.005 to 0.009 meter. The mesh sizes of some major components are summarized in Table 4.2.

	Refinement Level	Mesh Size (m)
Fan	7-7 plus proximity level 1	0.001 -0.002
Radiator, Condenser, TOC	7	0.002
Grill texture& nearby components	7-8	0.001-0.002
Tunnel, Inlet, Outlet	4	0.019

Table 4.2: Mesh settings for major full vehicle components

The full vehicle model contains a large quantity of very detailed geometries, approximately around 300 components in various sizes. Hence, for some crucial regions that require high quality mesh, a few volume refinement boxes were added. In Figure 4.6, it shows the front box and grill box. These two boxes are very important to be refined since it is where the grills are located, which means the accuracy of the mesh generation in these regions has an unavoidable effect on the airflow and therefore the simulation results. Another two volume refinement boxes are defined for the heat exchangers and the engine system as shown in Figure 4.7. The heat exchangers are the main focus of this simulation; therefore, a great attention has been given to study this area. Besides the boxes for smaller specific regions, there are also a few more broad larger volume boxes as shown in Figure 4.8 including ground box, car box, and global box. The global box contains the entire simulation area including the whole wind tunnel. The car box surrounds only the car geometry. The height of the ground box is defined as from the

bottom level of the wheels to the center of the wheels with 3 meters as width and a length of 7.5 meters. The final mesh sizes for these refinement boxes are shown in Table 4.3.

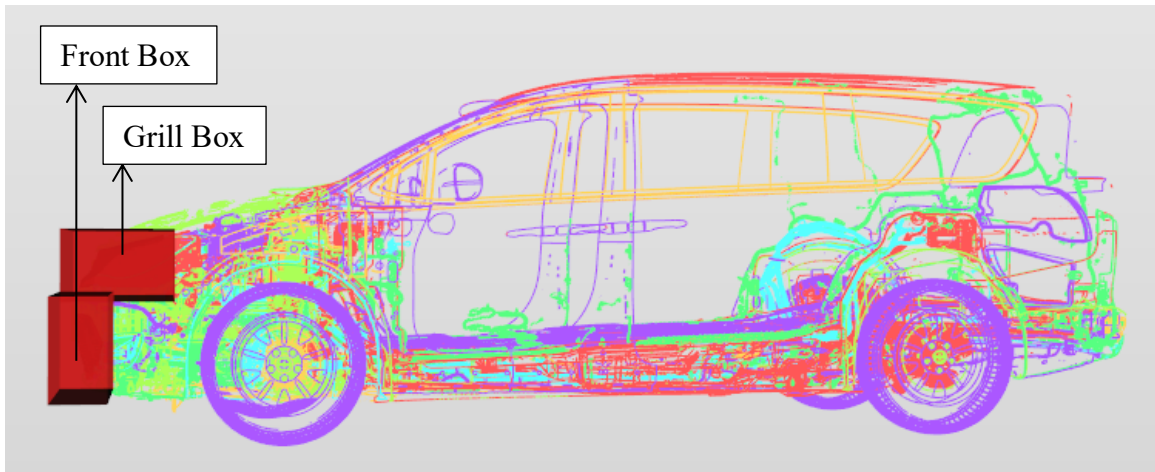


Figure 4.6: Volume refinement boxes: front box & grill box

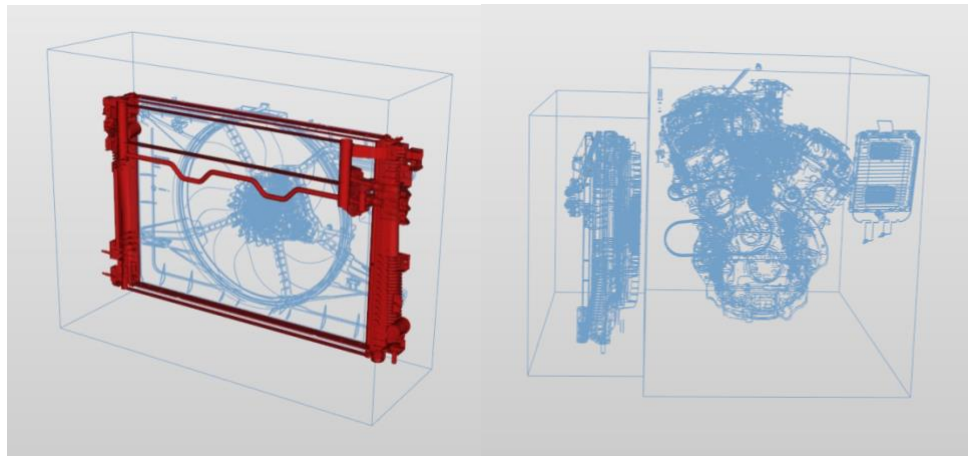


Figure 4.7: Volume refinement boxes: heat exchanger box & engine box

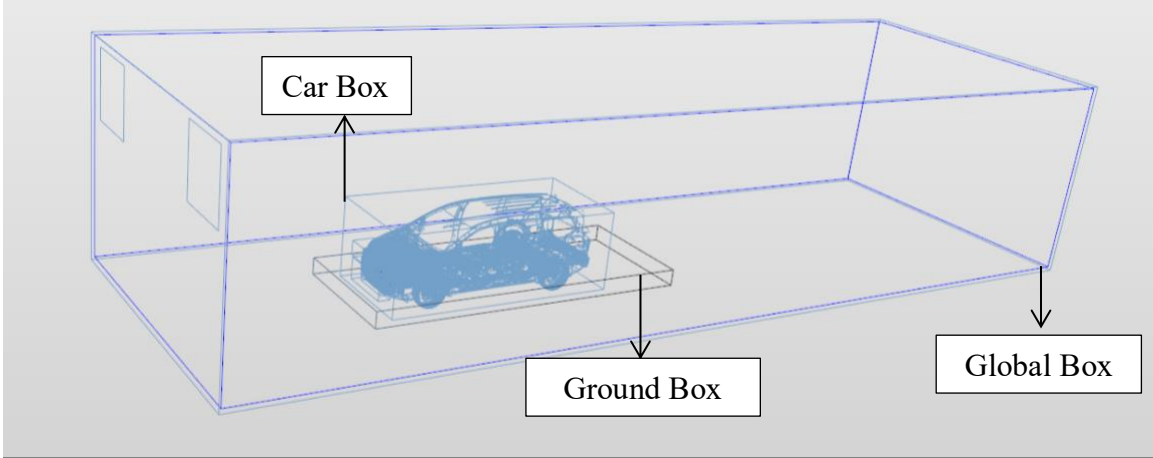


Figure 4.8: Volume refinement boxes: car box, ground box & global box

	Refinement Level	Mesh Size (m)
CM Box	6	0.005
Grill Box	6	0.005
Engine Box	5	0.009
Front Box	5	0.009
Ground Box	4	0.019
Car Box	2	0.075
Global Box	1	0.15

Table 4.3: Mesh settings for volume refinement boxes

In terms of boundary conditions, it is similar to isolated MRF modeling, where all the car components are modeled as no-slip solid walls. The inlet patch is composed of three boundaries and they are all modeled as velocity inlets. When modeling idle conditions, as shown in Figure 4.1 only the two small inlets are set with corresponding velocities and the big patch is treated with 0 velocity. For all the other cases, all three regions are assigned with the same velocity value. The outlet patch is model as a fixed pressure outlet.

The relevant settings are summarised as below:

- Incompressible; SIMPLE Solver; Steady State; Segregated;
- RANS; Standard k-ε turbulence model; No energy equations
- Fan: MRF (cell zone)
- Heat exchangers (Radiator, TOC, condenser): Porous Medium

Regarding Monitoring Functions, besides Surface Report, Volume Report that mentioned in MRF chapter, Zone Force is selected specifically since it calculates the volumetric flow rate and pressure drop across each porous media. The volumetric flow rate across the radiator is the main concern from the simulation regarding validating procedure since it is the only available parameter that could be compared from experimental data. In addition, the airflow data across radiator is also available from ACE+, hence the software capability between OpenFOAM and ACE+ are able to be compared.

## 4.2 Results & Discussions

With the mesh settings mentioned in the last section, a total of 54.17million cells were generated for the entire computational domain which contains 78% of hexahedral cells. The volumetric flow rate across the radiator is extracted at each operating point and compared to experimental data and ACE+ simulation results as shown in Figure 4.9 and Table 4.4.

OpenFOAM underestimates the volumetric flow rate across the radiator at low vehicle speed and the highest 20% error comparing to test data occurs at idle condition. As the vehicle speed increases, the percentage error drops and the results become more accurate to a certain threshold after where OpenFOAM begins to over-predict the airflow across the radiator. Comparing to the test bench model, the airflow patterns across the fan in full vehicle simulation are much more complicated, where the fan system is surrounded by very detailed component geometries. The airflow that comes from the inlet goes through the grill, AGS (active grill shutter) and all the cooling modules (TOC, condenser, radiator), and the nearby components such as heat exchanger seals and coolant

lines sometimes block the airflow and therefore creates swirls in the engine bay. Right behind the fan system are the exhaust heat shield and the main components of the engine. They create a blockage of the airflow that exits the fan blades and shrouds, which makes the airflow patterns more complicated. Comparing the CFD simulations to the actual full vehicle experiments, since the real geometries of TOC, condenser, and radiator are not simulated in CFD software, the change of the airflow patterns in real life through these heat exchangers are not precisely modeled. In addition, the actual wind tunnel has more complexity in details since it is a laboratory with all testing equipment and piping systems. In CFD simulation, the wind tunnel is simplified as a rectangular geometry with smooth walls. Since the airflow rate is greatly dependent on the heat exchangers' input parameters, the experimental data provided by the testing facility might not be accurate, and this could be one of the reasons that lead to inaccuracy.

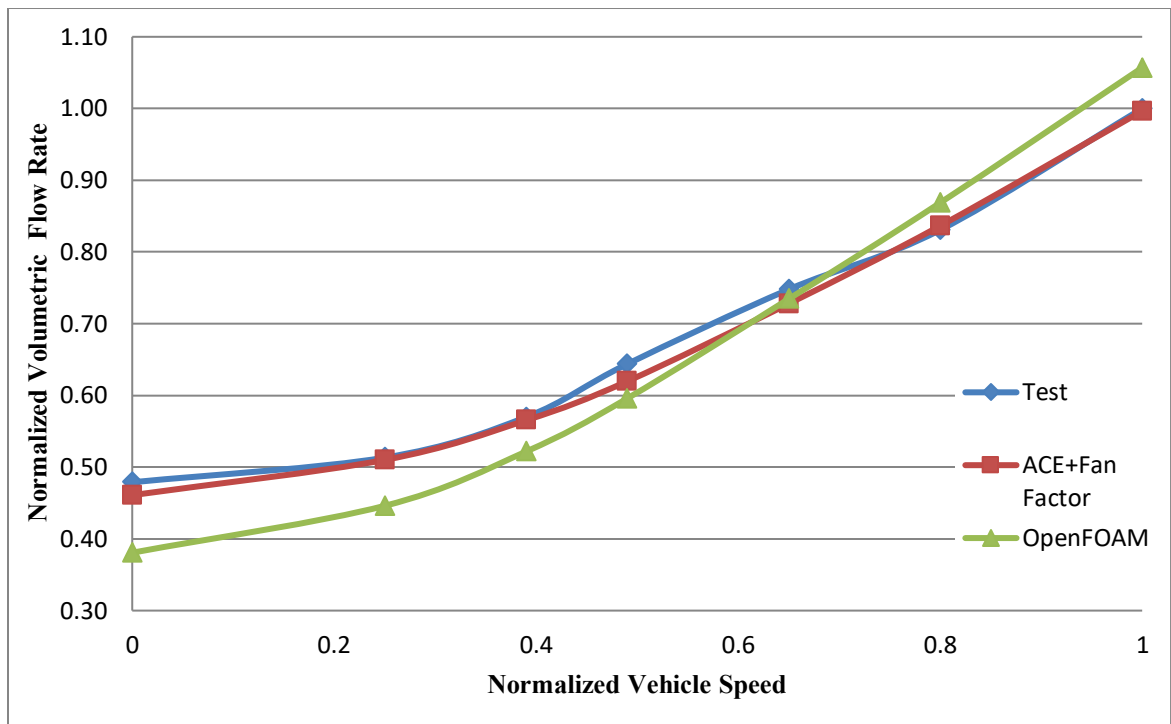


Figure 4.9: Comparisons among OpenFOAM, Test and ACE+ simulation results

Vehicle Speed	Flow Rate Test	Flow Rate ACE+	ACE+ Error%	Flow Rate OpenFOAM	OpenFOAM Error%
0	0.48	0.46	3.74%	0.38	20.51%
0.25	0.51	0.51	0.62%	0.45	13.09%
0.39	0.57	0.57	0.78%	0.52	8.42%
0.49	0.64	0.62	3.74%	0.60	7.46%
0.65	0.75	0.73	2.66%	0.73	1.78%
0.8	0.83	0.84	-0.68%	0.87	-4.55%
1	1.00	1.00	0.34%	1.06	-5.69%

Table 4.4: Simulation results and percentage errors

A cut plane in front of TOC is extracted and the velocity in the x-axis distribution is shown in Figure 4.11. For a better understanding of the airflow, the actual geometry of the vehicle is listed in Figure 4.11 for comparison purpose. The front bumper and lower grill are hidden so that the AGS and heat exchangers are visible. The fan blade is placed behind the condenser (red) and radiator, but for a better comprehension of where the blade is located in terms of its coordinates in the z-axis and the actual geometry size in reference of the whole vehicle model, the blade is highlighted in the graph. The green rectangular area behind the top grill is the TOC. It is observed that the velocity in x-axis reaches the maximum at the top grill and AGS (behind the bottom grill) since these are the main inlets of the air that flows into the underhood compartment and it seems that the air that across the bottom grill and AGS obtains a higher x-axis velocity. The effects of the heat exchangers on the airflow pattern are not obvious yet since the cut plane is extracted before the air flows through TOC. From the vector glyph, it shows that after the airflow goes through the top grill, it intends to drift downward to the middle since on the side the heat exchanger seals block the passage towards further left and right side.

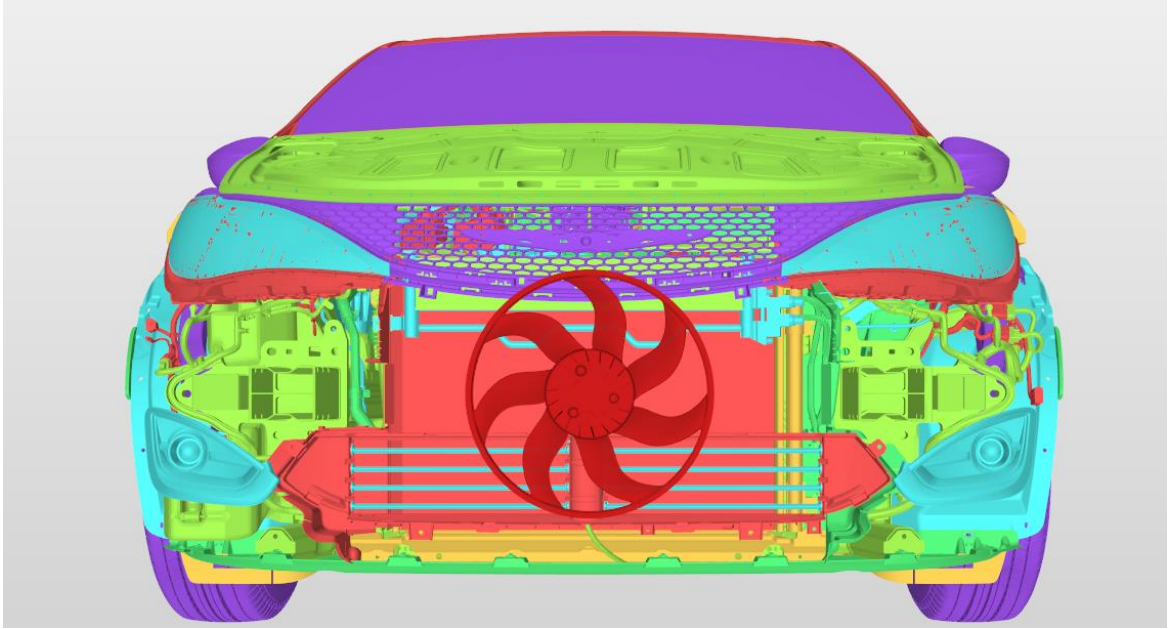


Figure 4.10: Front-end vehicle configuration

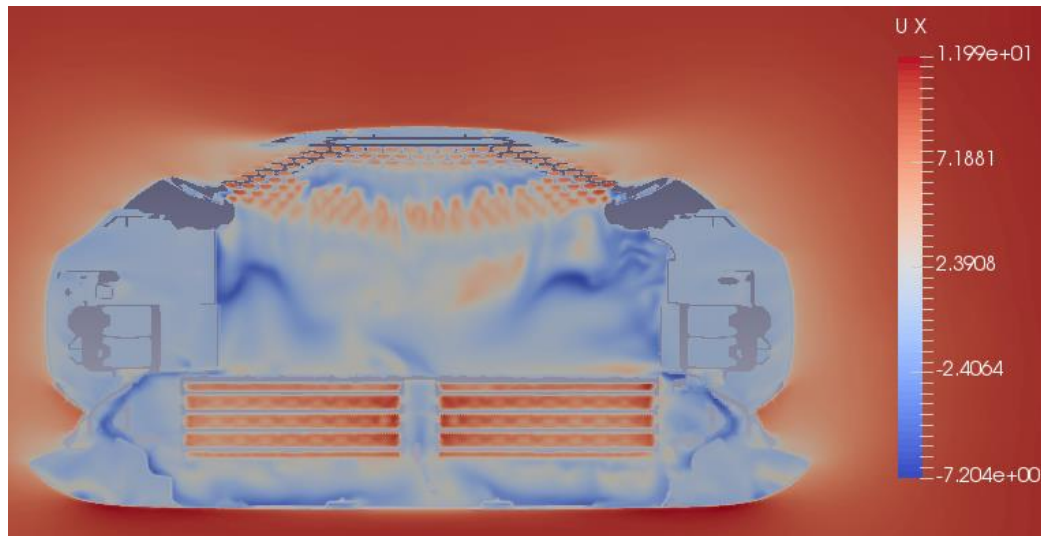


Figure 4.11: Velocity in x-axis direction distribution at a cut plane in front of TOC

Figure 4.12 to 4.15 are the pressure distribution at four cut planes that are placed in front of TOC, condenser, radiator, and fan correspondingly. Figure 4.12 shows that the maximum pressure occurs at the top grill and since the airflow has not passed TOC yet, so it does not show any obvious effects from TOC. After the airflow passes TOC, the pressure dropped approximately 60 Pascals and it becomes the region with the lowest

pressure in the underhood compartment. The maximum pressure region remains at the areas that are behind the top grill and bottom grill.

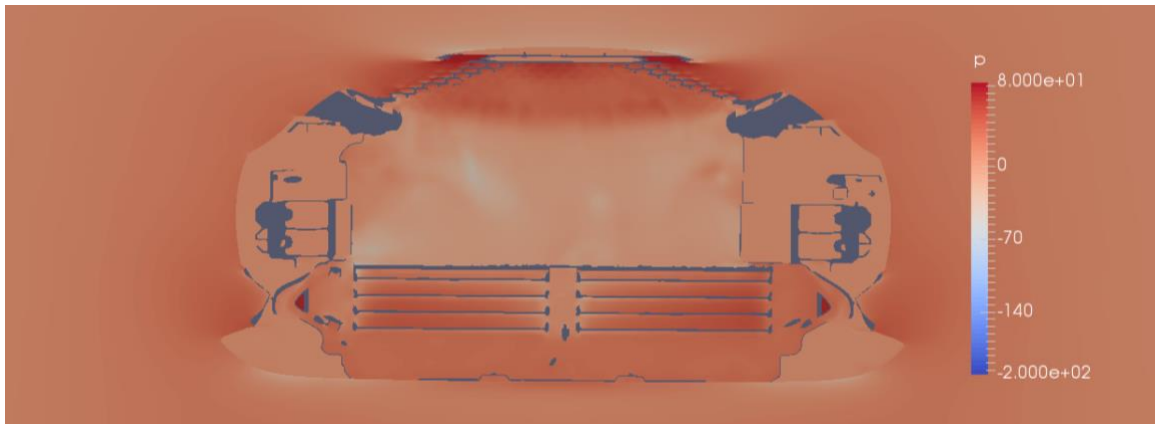


Figure 4.12: Pressure distribution at a cut plain in front of TOC

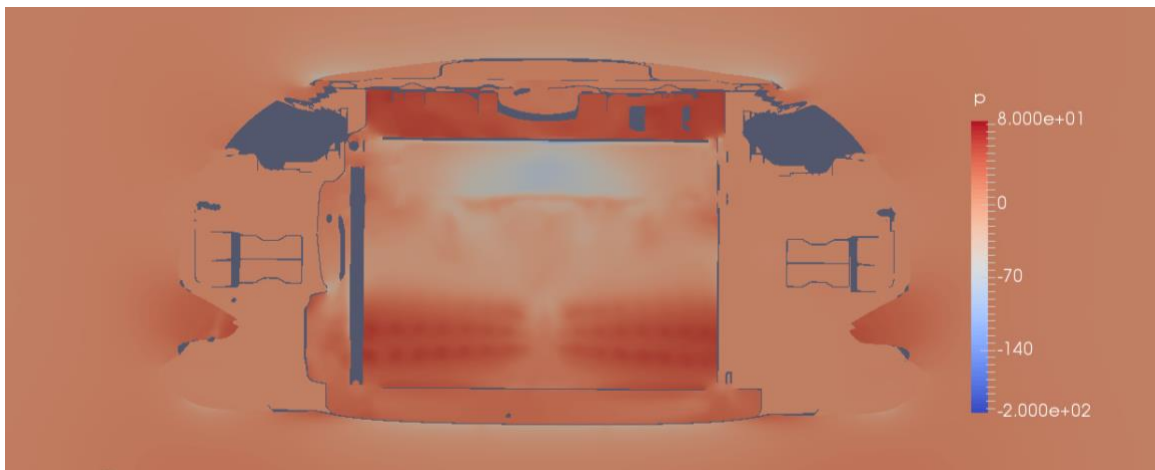


Figure 4.13: Pressure distribution at a cut plane between TOC and condenser

The pressure distribution changes significantly after the airflow passes through the condenser since it is observed that the field started to be greatly affected by the fan system. The pressure drop across the condenser is around 60 Pascals and the pressure distribution can be seen with a relatively clear pattern of the fan blades, where the minimum pressure occurs. The fan blade shaped pressure distribution pattern becomes more obvious at the cut plane between the radiator and the fan system where the pressure drop across the radiator achieves approximately 100 Pascals. The pressure in the middle of the fan does not reach a very low value due to the stationary hub obstruction.

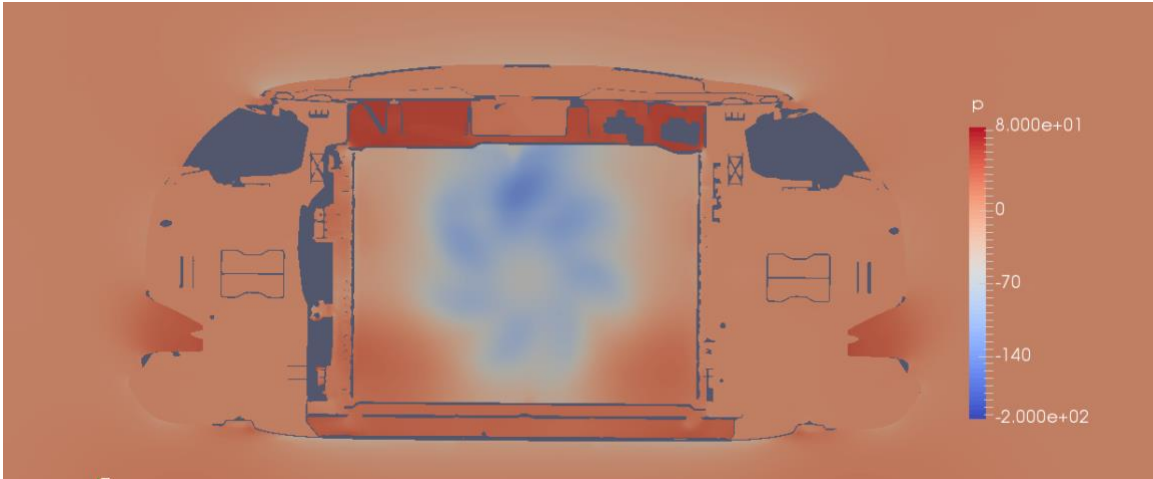


Figure 4.14: Pressure distribution at a cut plane between condenser and radiator

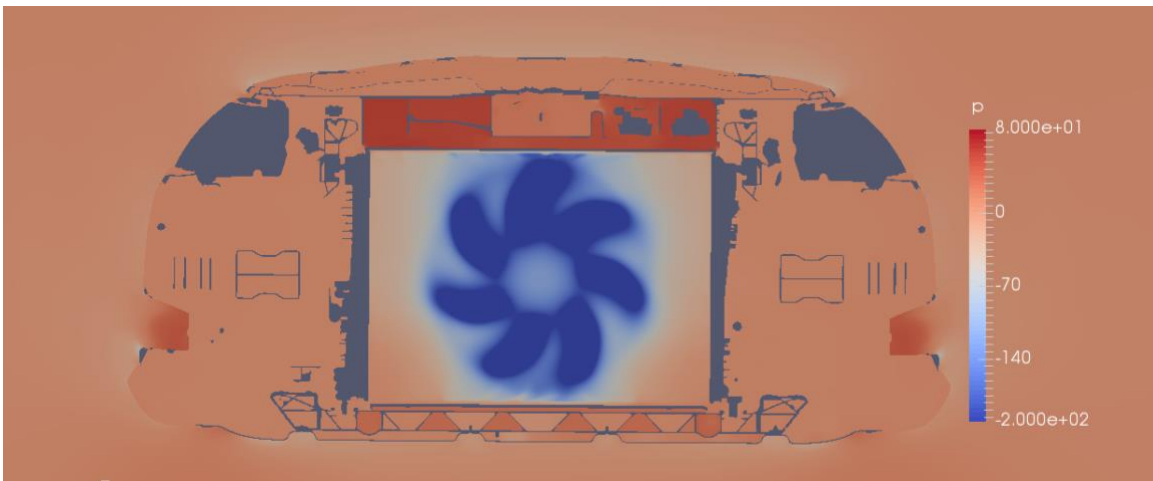


Figure 4.15: Pressure distribution at a cut plane between radiator and the fan

A cut plane in the y-axis located at the middle of the vehicle is extracted. The background color represents the pressure distribution and the vector arrows represent the airflow velocity. It can be observed that the pressure decreases after passing through heat exchangers then the minimum pressure in the underhood compartment occurs in the vicinity of fan blades. The maximum airflow velocity takes place after the airflow exits from the fan and creates swirls before blocking by the engine.

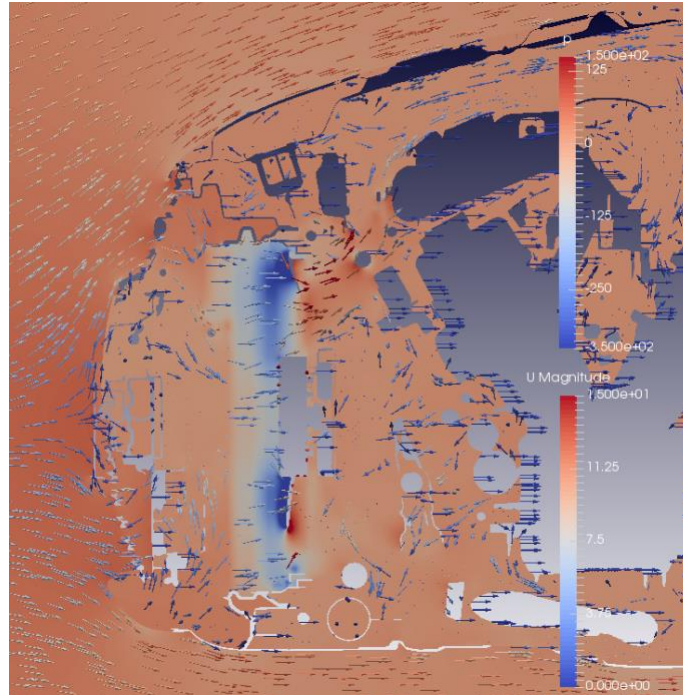


Figure 4.16: Velocity distribution in y-axis

The pressure drop and volumetric flow rate across each heat exchanger are also plotted as shown below.

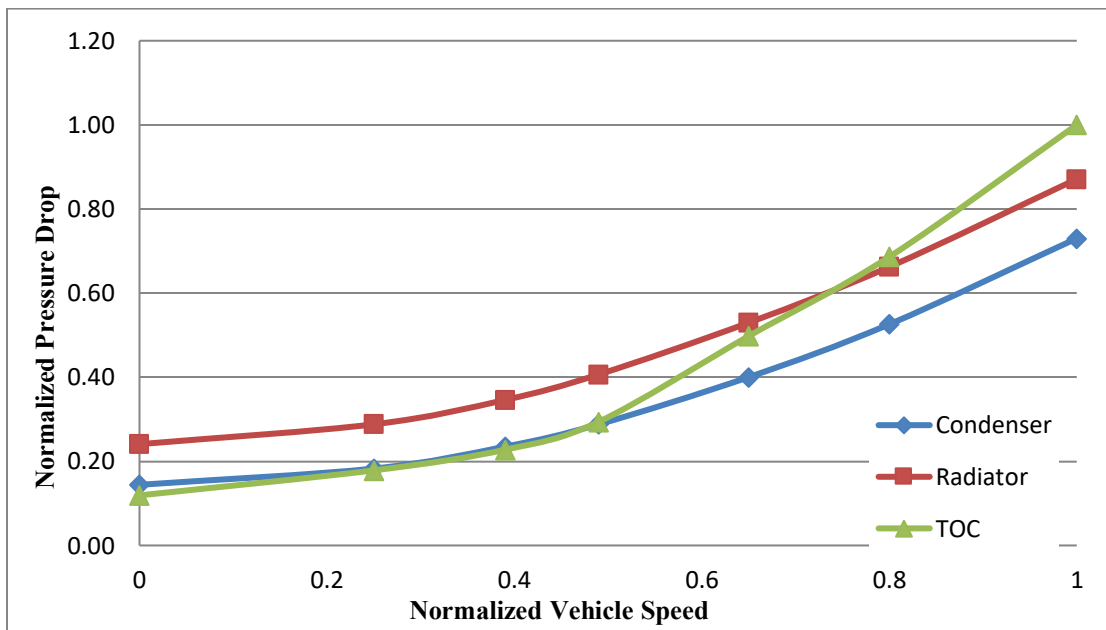


Figure 4.17: Pressure drop across condenser, TOC and radiator

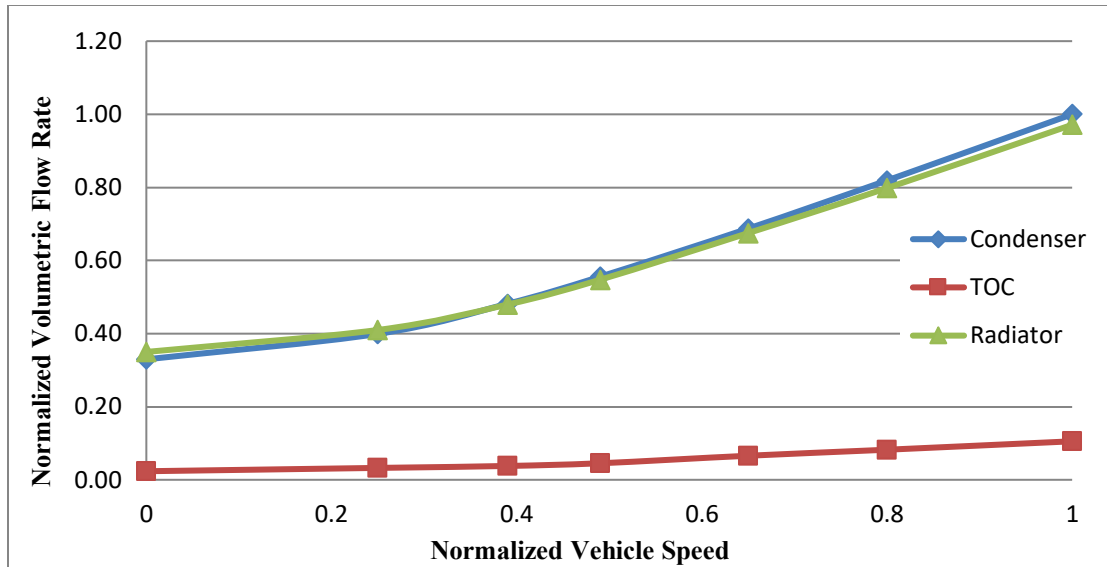


Figure 4.18: Volumetric flow rate across condenser, TOC and radiator

The purpose of this section is to study the influence of the MRF domain on full vehicle simulation. However, because of the compact structure in the underhood compartment, the radiator is right behind in front of the fan, therefore there is a very strict limitation on the modification of the MRF domain. Similar to the test bench model, due to the geometry of the shroud, the MRF model is not able to be extended radially in order to avoid interfering with the shroud. As shown in Figure 4.19, the MRF domain is extended 6mm in  $x+$  direction before it interferes with the front of the shroud and extended backward ( $x-$ ) 9mm before touching the radiator geometry. The results show that the change of the MRF domain has a very small influence on the pressure rise or volumetric flow rate across the heat exchangers in full vehicle simulations. The possible reason could be due to the highly irregular flow patterns in the engine bay, which has a much stronger influence comparing to the effect of modifying the MRF domain. The effect of the MRF domain could be strengthened if the modification of the MRF domain is bigger.

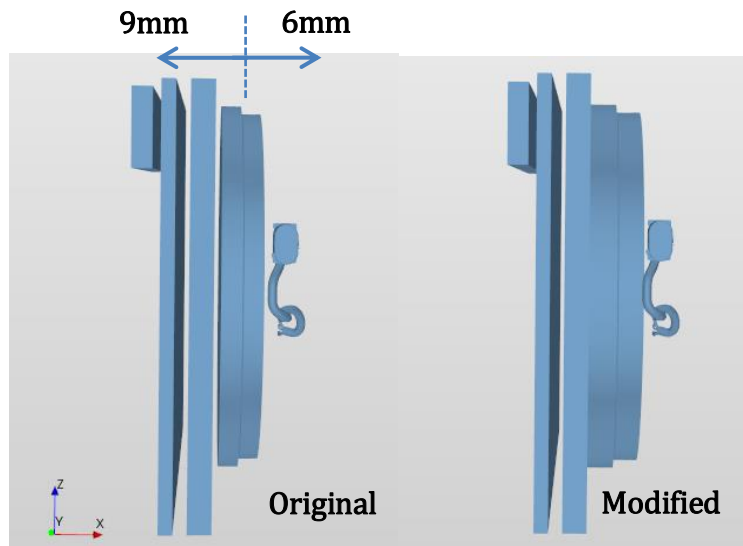


Figure 4.19: Geometry of original MRF domain and modified MRF domain

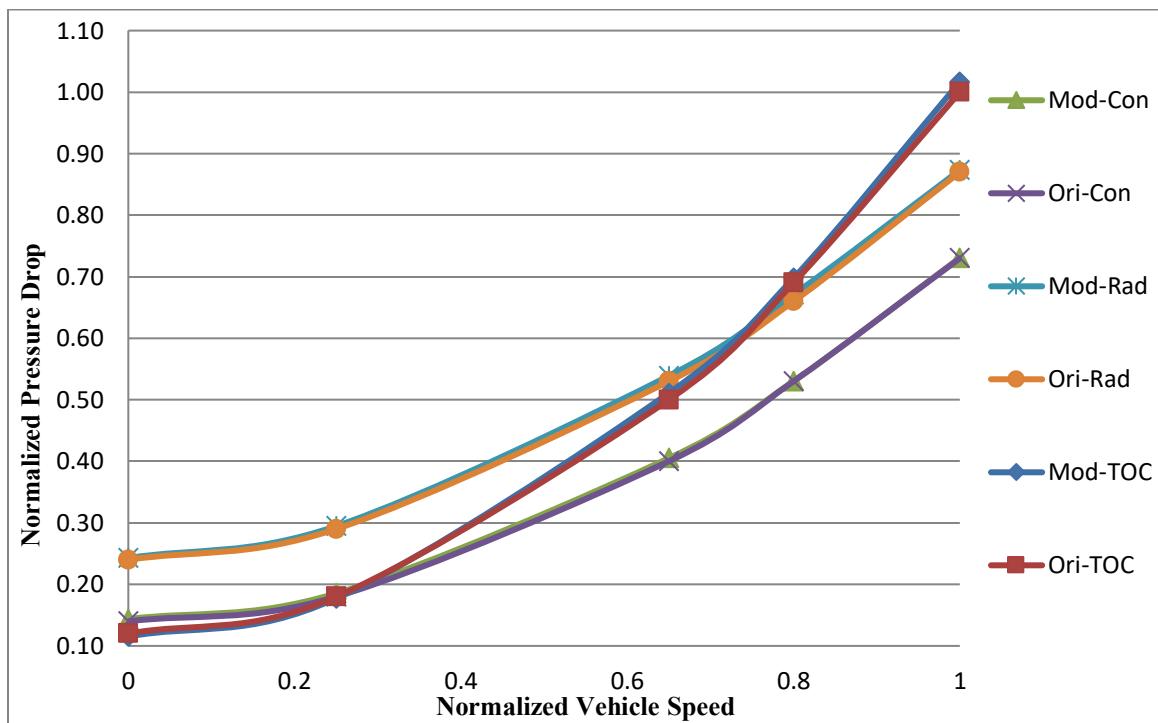


Figure 4.20: Pressure drop comparisons between original MRF domain and modified MRF domain across each heat exchanger

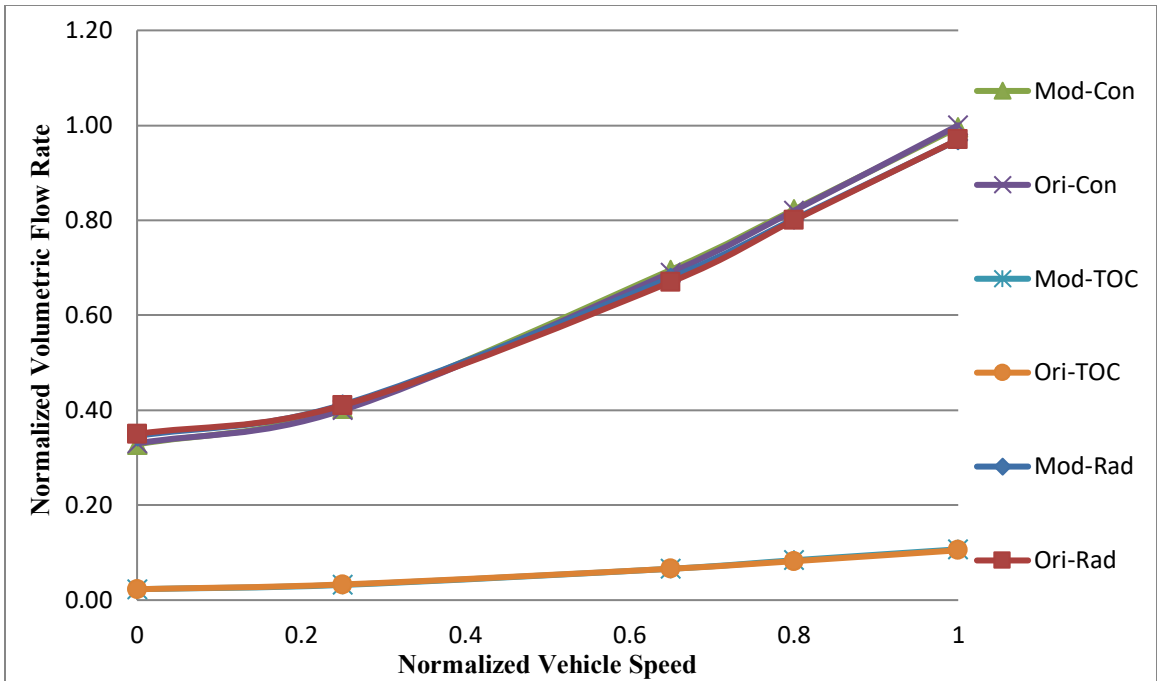


Figure 4.21: Volumetric flow rate comparisons between original MRF domain and modified MRF domain across each heat exchanger

## CHAPTER 5 ACTUATOR DISK MODEL

### 5.1 Background

In Chapter 3, one of the most popular industrial fan modeling technique MRF was investigated. It requires relatively lower computational effort than sliding mesh method since the MRF model is operated at steady-state instead of transient. However, the mesh generation for the fan blade still involves a significant effort in regard to the mesh quality and computation time. Actuator Disk model eliminates the actual fan geometry therefore largely reduces the computational effort on detailed mesh generation and simulating the actual detailed flow pattern in the vicinity of the fan system. An additional input however is required for setting up the Actuator Disk model, which is the fan test data for defining the fan curve and it will be explained in detail in the following section. Therefore, this chapter is dedicated to study the usage of Actuator Disk technique in OpenFOAM and investigate the accuracy level of its simulation results comparing to experimental data and the MRF method.

Actuator Disk model simplifies the fan blades geometry to a disk with very thin thickness, where in this project specifically, the thickness of the disk is chosen to be the same as the thickness of the actual fan blades and the diameter of the disk is modeled as the same dimension of the fan blades as well. The main principle behind Actuator Disk model is Bernoulli equation as shown below.

$$\Delta P = \frac{1}{2}\rho(U_d^2 - U_u^2) \quad (5.1)$$

where  $U_u$  and  $U_d$  represent the velocity at upstream and downstream respectfully, and  $\Delta P$  refers to the pressure difference.

In OpenFOAM, there are a few actuation disk model techniques that are available such as actuation disk source, constant thrust actuation disk source, and radial actuation disk source. Among the options, the thruster Actuator Disk source is selected for this project which is the most optimal for the test bench application.

## 5.2 Simulation Setup

The Actuator Disk geometry as mentioned previously is modeled as a cell zone. The procedure to establish a geometry as a cell zone is the same as mentioned in MRF modeling. In order to assign the cell zone as an Actuator Disk, an equation source model type “*thrustActuationDiskSource*” has to be included in the caseSetupDict file under ‘fvoptions’. This source computes the pressure rise and the circumferential velocity across the thruster. The pressure rise is modeled by adding axial momentum and it is calculated as in Equation (5.2).

$$\Delta P = L(a_0 + a_1 U_n + a_2 U_n^2 + \dots) \quad (5.2)$$

Where L represents the radially varying load coefficient and  $U_n$  refers to the velocity in the axial direction.

The circumferential velocity jump is calculated as below,

$$\Delta U_c = \omega \sin(\alpha) (n \times r) \quad (5.3)$$

Where  $\omega$  refers to the rotational velocity,  $\alpha$  represents the blade angle and n means the unit axial direction.

Then, a few coefficients need to be defined by the user and they are explained as below.

**Point1 (0.014 0.0 0.0); Point2 (0.0606 0.0 0.0)**

These two points define the axis of fan rotation. For this project, the coordinates are using the maximum and minimum point in the x-axis direction of the center of the Actuator Disk geometry.

**F List <scalar> n (a<sub>0</sub> a<sub>1</sub> a<sub>2</sub> ..)**

These parameters are defined using the polynomial that describes the correlation between the pressure rise and the airflow velocity. Ideally, the pressure rise data should be the change of pressure across the fan blades only. However, during the experiment, the shroud was included in the tunnel as well. Since we do not have the experimental data for the pressure rise across the fan blades, the pressure drop of the airflow that caused by the

testing facility (tunnel geometry, shroud geometry etc.) are estimated by CFD approach. Using the same geometry provided previously (tunnel, inlet, outlet, shroud etc.), without the Actuator Disk Model, simulations are done at each operating points and the pressure drop at each case is recorded. Then, by subtracting the test data with the pressure drop from simulations, the pure pressure rise only resulted from the fan blades are produced. The new correlation between the pressure rise and airflow velocity are plotted as shown in Figure 5.1, and the equation becomes,

$$\Delta P = -0.1484U^3 + 1.7091U^2 - 9.3452U + 181.4 \quad (5.4)$$

Therefore, the parameter above is added into the caseSetupDict as “F List <scalar> 4 (181.4 -9.3452 1.7091 -0.1484).

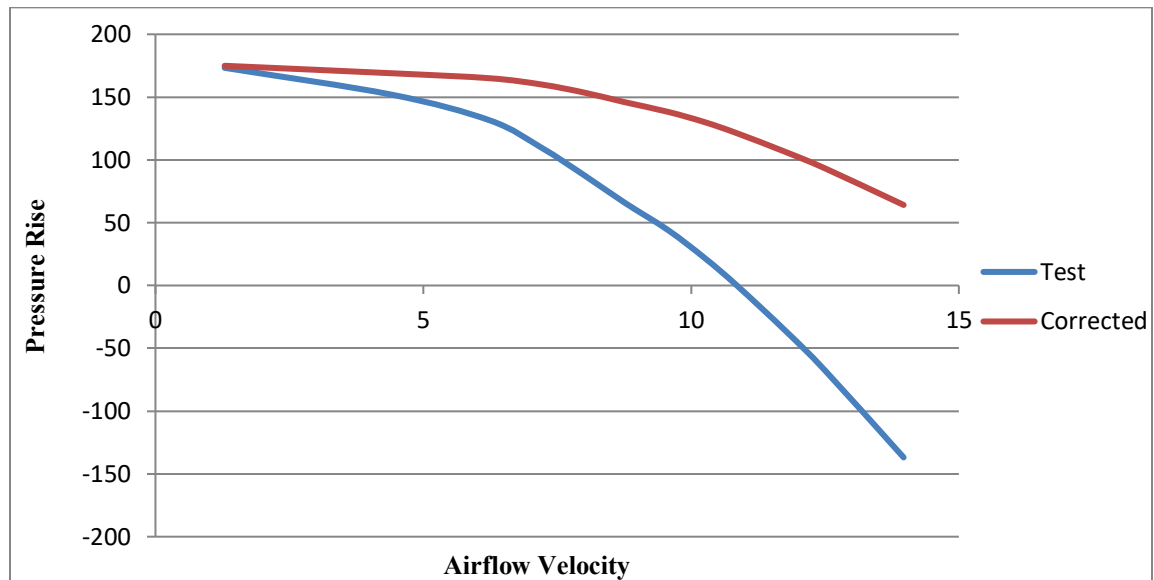


Figure 5.1: Correlation between pressure rise and airflow velocity for isolated fan blades

### alphaProfile

Alpha profile describes the blade angle  $\alpha$  as a function of its radial position in regard to the radius of the fan. The blade angle is a required parameter to calculate the circumferential velocity jump as shown in Equation (5.2). When the swirl is not considered and the pressure rise is the only concern, the alpha profile can be set up as (0 0; 1 0), which means the blade angle is 0 throughout the blade.

### loadProfile

Load profile defines a load value from 0 to 1 as a function of corresponding radial location with respect to the entire blade ( $r/R$ ). It is used to calculate the jump in axial momentum. When the swirl is not considered and the main purpose of the simulation is to study the pressure rise, the load profile is defined as (0 1; 1 1).

The mesh size for each of the components and the volume refinement regions are listed as below in Table 5.1

Patch Name	Minimum Refinement Level	Maximum Refinement Level	Cell Size (m)
Actuator Disk	4		0.019
Shroud	7	7	0.002
Hub	7	7	0.002
Motor	7	7	0.002
Tunnel	4	4	0.019
Inlet	4	4	0.019
Outlet	4	4	0.019
Cylinder_S	6		0.005
Cylinder_L	5		0.009
Sphere	2		0.075

Table 5.1: Mesh size of all components in Actuator Disk Model

The boundary conditions remain the same as the MRF model as summarised in Table 5.2.

Components	Boundary Conditions
Inlet	Inlet- Volumetric Flow Rate
Outlet	Outlet- Fixed Pressure
Tunnel, shroud, hub, motor	No-slip Solid Wall
Actuator Disk	Cell zone- Actuator Disk Source

Table 5.2: Boundary conditions of all components in Actuator Disk Model

The relevant solver settings remain the same as well and are summarised as below:

- Incompressible; SIMPLE Solver; Steady State; Segregated;
- RANS; Standard k- $\epsilon$  turbulence model; No energy equations;
- 3000 iterations; Velocity limiter: 120m/s;
- Monitoring functions: Surface report (a few cut planes placed at upstream and downstream to measure averaged pressure); Volume report;

### 5.3 Results & Discussions

With the mesh settings mentioned in the last section, the total mesh cells generated for Actuator Disk Model is approximately 9 million. The simulations were conducted at ten operating points, and the pressure rise at each operating points are plotted in Figure 5.2 along with the data from experiments and MRF. As shown in Figure 5.2, the simulation results of the Actuator Disk Model are very accurate and consistent when the volumetric flow rate is above a certain threshold. The trend of Actuator Disk pressure rise plot complies with the trend of MRF, but it does not underpredicts the pressure rise as much as MRF method. The results from the Actuator Disk Model appear to be very promising since the pressure rise is defined directly using the correlation extracted from calculations. However, the pressure drop data that was caused by the fan shroud and tunnel geometry were not obtained from experimental results. Hence, the pressure drops are not one hundred percent reliable, and the simulation error from the pressure drop could therefore lead to the inaccuracy of the correlation between pressure rise and airflow rate of isolated fan blades. This could be part of the reason why the Actuator Disk simulation results do not agree with the test data completely.

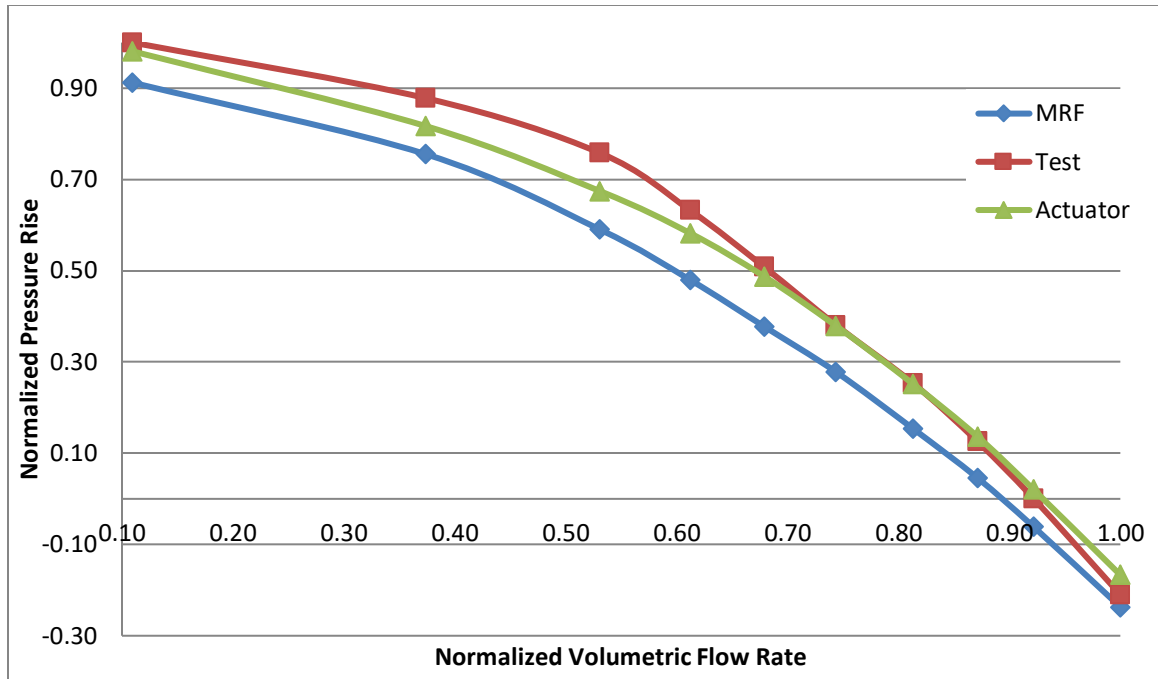


Figure 5.2: Correlation between pressure rise and volumetric flow rate of MRF, Actuator Disk Model and experimental data

	1	2	3	4	5	6	7	8	9	10
Actuator Disk	0.98	0.82	0.67	0.58	0.49	0.38	0.25	0.14	0.02	-0.17
Test	1	0.88	0.76	0.63	0.51	0.38	0.25	0.13	0.00	-0.21
MRF	0.91	0.76	0.59	0.48	0.38	0.28	0.15	0.05	-0.06	-0.24

Table 5.3: Pressure rise results from Actuator Disk Model

To observe and compare the pressure distribution across the fan between MRF and Actuator Disk simulations, a cut plane is extracted from both models in x-y plane across the middle of the blade. In the Actuator Disk Model, the pressure rise pattern near the blades is significantly different from the MRF model. The pressures at the points with same x coordinate in the Actuator Disk zone increase evenly throughout the surface from upstream to downstream since the pressure rise across the fan is calculated by adding axial momentum and all elements that cross through the Actuator Disk undergo an equal amount of pressure increment. The pressure distribution in the MRF model however is not linear and experiences a pressure jump after the airflow goes over the blade. The pressure distribution depends largely on the blade geometry where the minimum pressure occurs behind the blade and the maximum pressure occurs downstream of the blade.

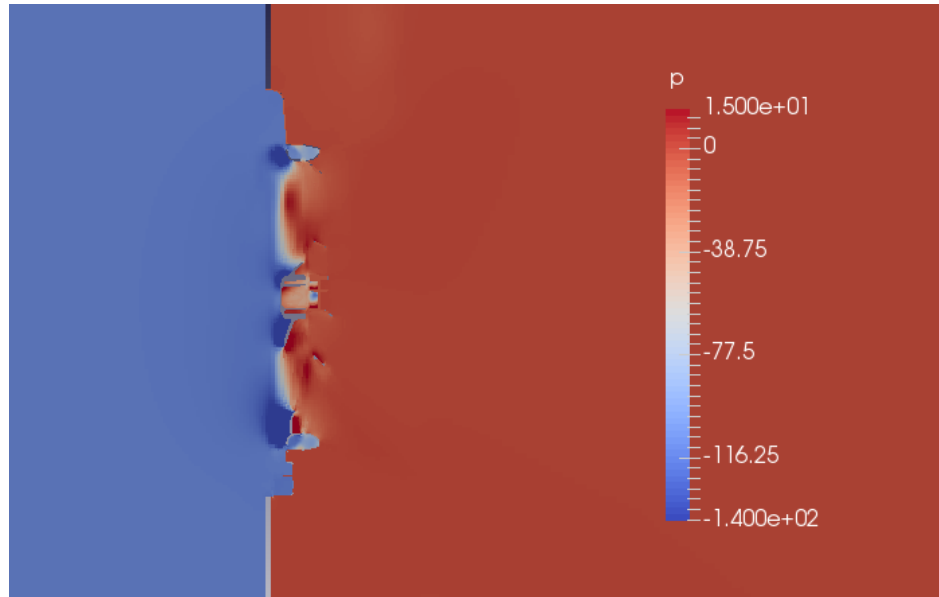


Figure 5.3: Pressure distribution across the fan of MRF model

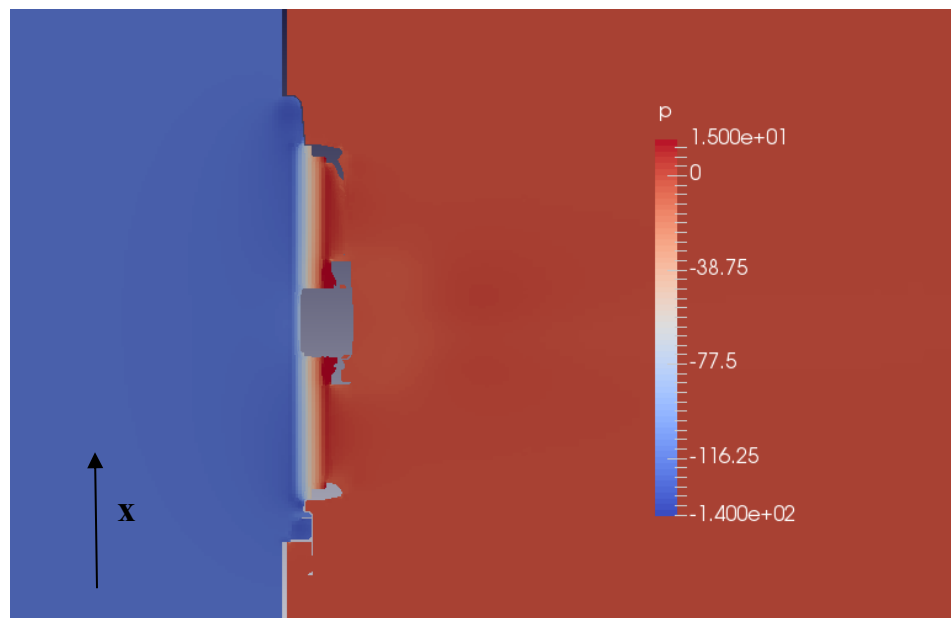


Figure 5.4: Pressure distribution across the fan of Actuator Disk Model

Similar to the pressure distribution, the velocity pattern in the Actuator Disk Model again is linear and evenly distributed along the domain. The velocity vectors show that the airflow maintains a relatively high velocity along the straight path downstream of the fan towards the outlet. In the MRF model, the velocity distribution appears to be highly irregular downstream of the fan, and the velocity near the fan is much larger comparing to the velocity that is near the Actuator Disk zone.

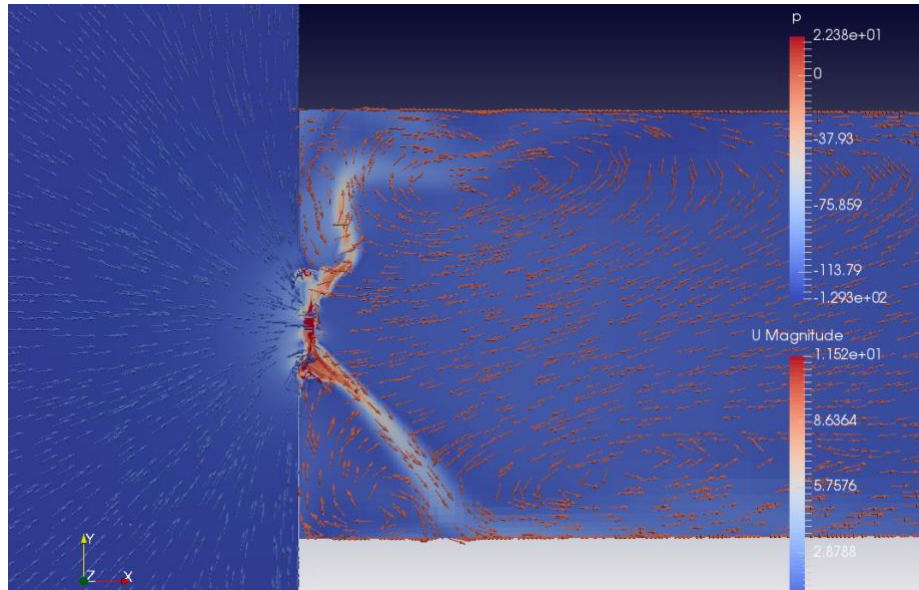


Figure 5.5: Velocity distribution across the fan in MRF model

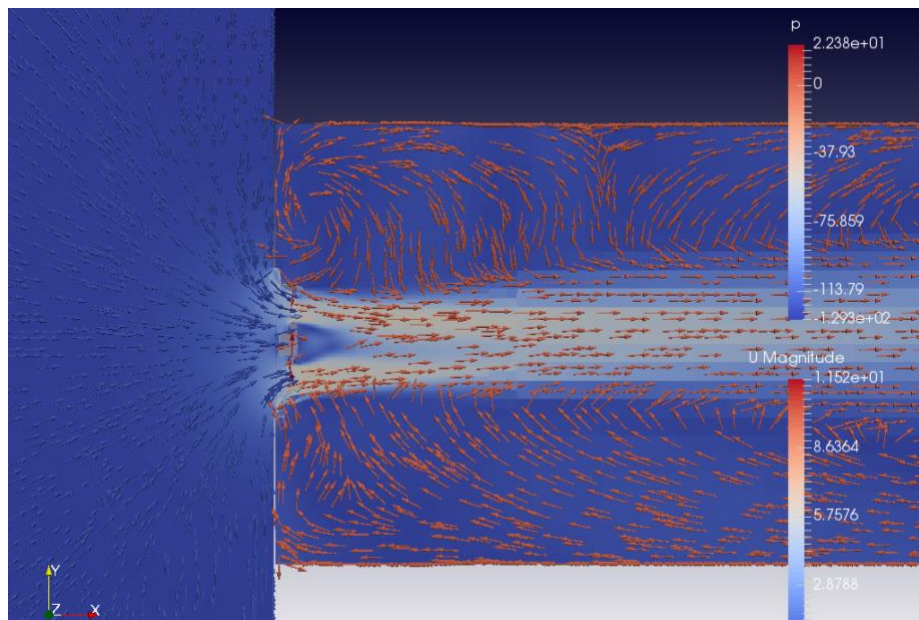


Figure 5.6: Velocity distribution across the fan in Actuator Disk Model

Velocity properties are extracted on a cut plane 25mm downstream of the fan in both MRF and Actuator Disk models. The velocity magnitude of MRF model appears to be twice as much as in Actuator Disk Model and the velocity distribution in MRF model obtains a much higher irregularity. The maximum velocity occurs mainly around the blade tips while in Actuator Disk the entire Actuator Disk region has a high velocity and seems to be relatively evenly distributed excludes the hub region. The velocity

distribution in Actuator Disk Model appears to be ‘sliced’ which is caused by the obstruction of the shroud geometry. Axial velocity characteristics of both models are shown in Figure 5.9 and 5.10. It appears in Actuator Disk Model, the axial velocity is the dominant velocity component which has a magnitude of 6.29m/s out of a total velocity magnitude of 6.47m/s. In Figure 5.11 and 5.12, it shows in Actuator Disk Model the tangential velocity is only 2.17m/s. In the MRF model, the tangential velocity and axial velocity are 9.39m/s and 8.15m/s respectively out of a total velocity magnitude of 11.44 m/s. MRF model has a much higher tangential velocity than in Actuator Disk.

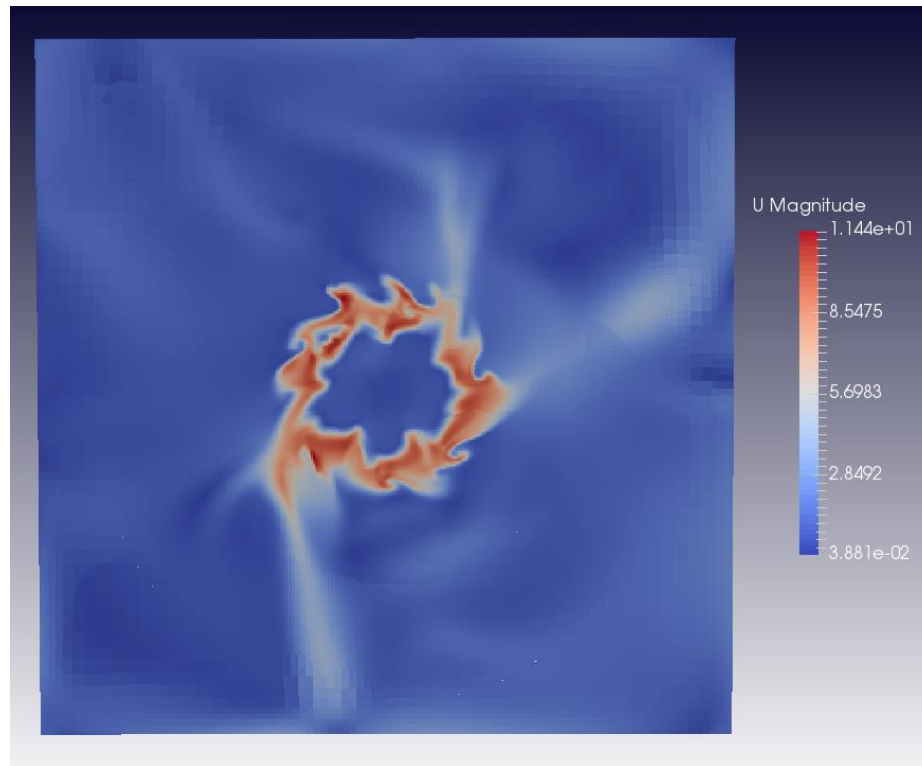


Figure 5.7: Velocity distribution (Magnitude) on a cut plane 25mm downstream of the fan in MRF model

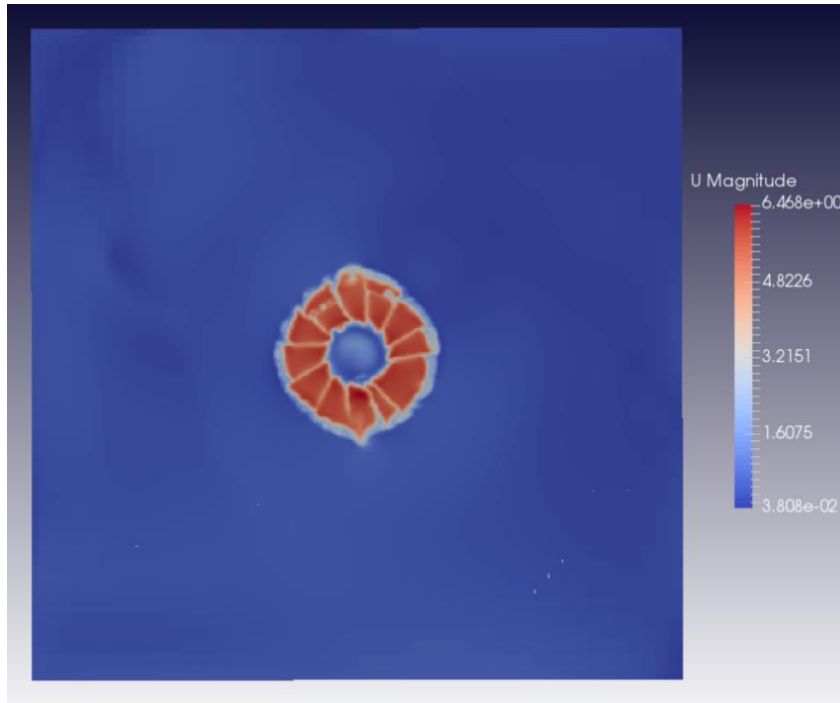


Figure 5.8: Velocity distribution (Magnitude) on a cut plane 25mm downstream of the fan in Actuator Disk Model

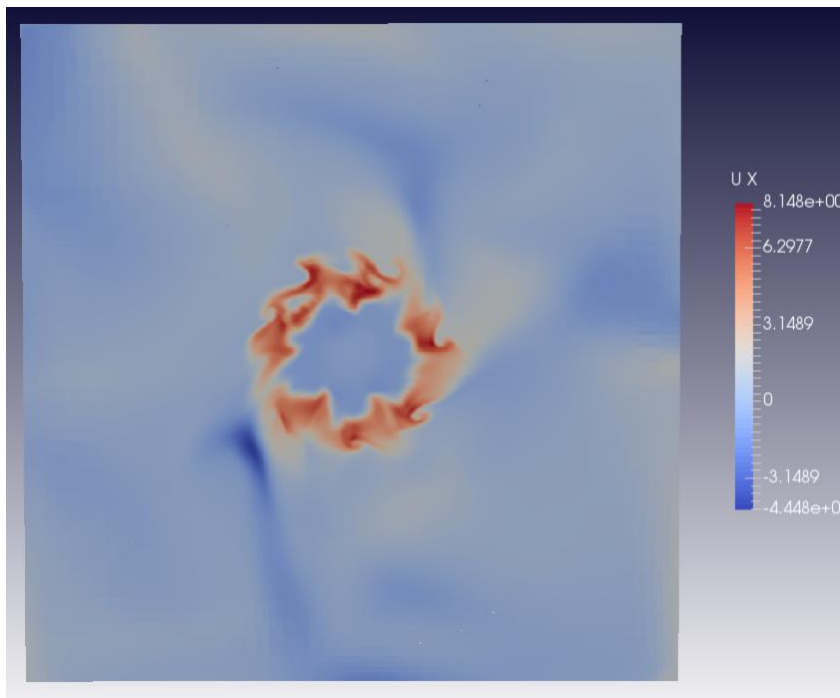


Figure 5.9: Axial velocity characteristics on a cut plane 25mm downstream of the fan in MRF model

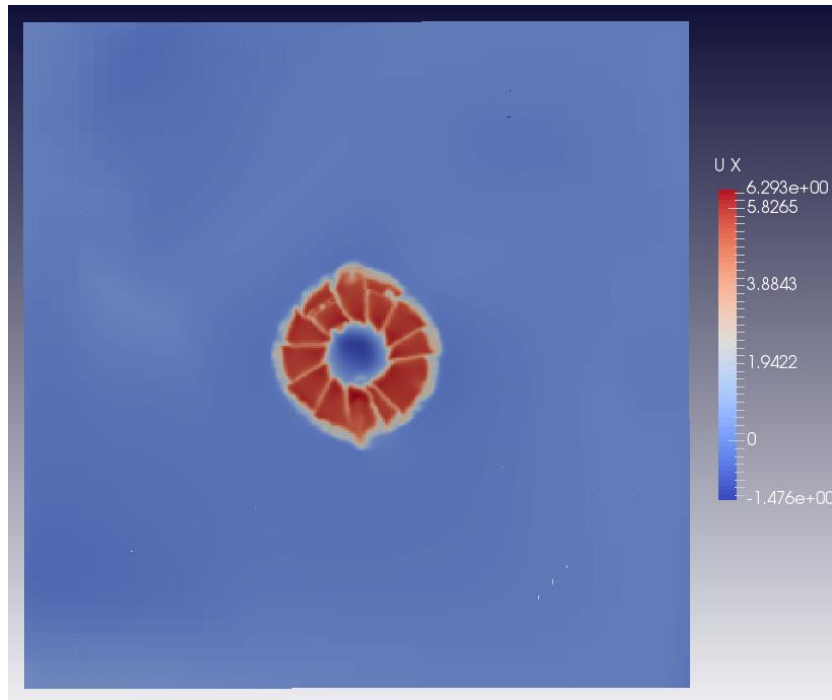


Figure 5.10: Axial velocity characteristics on a cut plane 25mm downstream of the fan in Actuator Disk Model

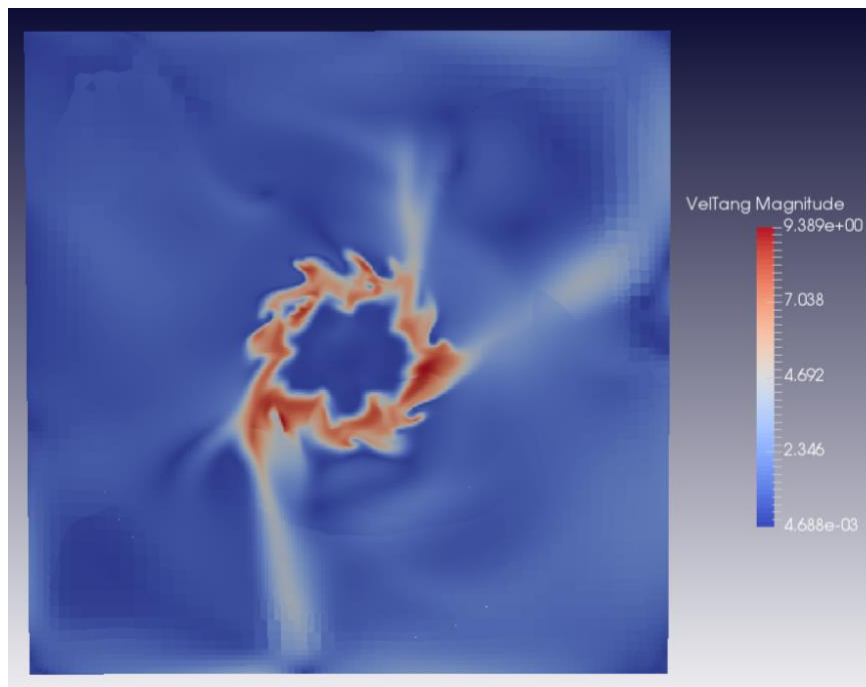


Figure 5.11: Tangential velocity distribution on a cut plane 25mm downstream of the fan in MRF model

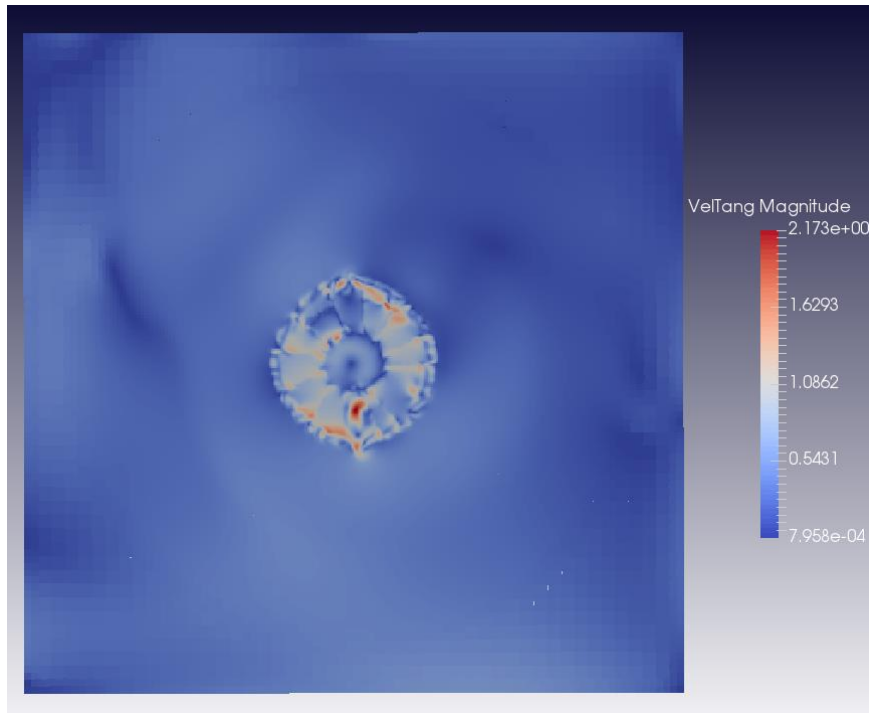


Figure 5.12: Tangential velocity distribution on a cut plane 25mm downstream of the fan in Actuator Disk Model

## CHAPTER 6 CONCLUSIONS AND FUTURE WORK

### 6.1 Conclusions

From the simulation results mentioned above and in regard to the objectives of this project, some conclusions can be drawn and listed as below:

- With the same model setup for an isolated fan simulation using MRF technique, OpenFOAM appears to have a very promising capability in solving the pressure rise, which proved to be more accurate than Star-CCM+ and ACE+. The correlation between the pressure rise and the volumetric flow rate is consistent with the experimental data but underestimates the pressure rise.
- The domain of MRF geometry has a great influence on the pressure rise across the fan; a larger MRF domain increases the accuracy of the simulation results.
- The influence of upstream boundary condition (slip or no-slip wall) on simulation results appears to be negligible.
- The dimension of upstream geometry appears to have little effect on the pressure rise. When the inlet velocity increases, a smaller upstream volume predicts a more accurate pressure rise.
- When MRF technique is applied in a full vehicle simulation, comparing to ACE+ results with fan factor, OpenFOAM has a less consistent simulation results which underpredicts the pressure rise at low airflow rate.
- When the MRF domain is expanded in a full vehicle simulation, it improves the results but by a very small amount which can be neglected. (Due to the compact geometry near the fan in the underhood compartment, the study on the size of the MRF domain is very constrained. The change of the MRF domain can only be extended axially not more than 10mm)
- Actuator Disk Model in OpenFOAM gives an even more promising result than the MRF technique when the pressure rise is the main concern of the project. The velocity and pressure distribution and characteristics are very different from MRF model.

## 6.2 Future Work

During the investigation of the above models, some interesting questions are raised but were not able to be studied in this project due to the scope and limitation of this project. Some recommendations for future work are concluded as following.

- Since MRF requires a relatively accurate mesh generation which consumes a high computational costs, one can try to simplify the shroud geometry and hub etc. and investigate whether it affects the pressure rise.
- Full vehicle simulation can also be investigated using the Actuator Disk technique, and to further validate the capability of the Actuator Disk Model in OpenFOAM.
- During the communication with the technical support at ENGYS, it was mentioned that a modified version of thruster fvOption model will be released in the next Helyx version 3.1, which appears to be able to obtain a more promising result. A new feature called zonal averaging option is available, and it calculates the average velocity in the zone for creating pressure jump rather than at individual point. One can study and investigate the new Actuator Disk Model in OpenFOAM.
- When the boundary conditions are defined in full vehicle simulation other than idle condition, the three inlets are required to use the same velocity, where in the real physical test, the two small inlets are shut which therefore has 0 velocity. One can study the effect of boundary conditions by changing the velocity settings for the three inlets.

## REFERENCES/BIBLIOGRAPHY

- [1] Gullberg, P., Löfdahl, L., Nilsson, P., Adelman, S. (2009). A correction method for stationary fan CFD MRF models. 2009-01-0178, SAE International 2009.
- [2] Gullberg, P., Löfdahl, L., Nilsson, P., Adelman, S. (2009). An investigation and correction method of stationary fan CFD MRF simulations. 2009-01-3067, SAE International 2009.
- [3] Gullberg, P., Löfdahl, L., Nilsson, P. (2011). Fan modeling in CFD using MRF model for under hood purposes. AJK2011-23020, ASME-JSME-KSME Joint Fluids Engineering Conference 2011.
- [4] Barron, R.M., Sahili, A., Zogheib, B. (2013). 3-D modeling of axial fans. Applied Mathematics 632-651.
- [5] Bothe, F., Friebe, C., Heinrich, M., Schwarze, R. (2014). CFD-simulation of incompressible turbomachinery - a comparison of results from ANSYS Fluent and OpenFOAM. NO.GT2014-26338, ASME Turbo Expo 2014.
- [6] Jain, S., Deshpande, Y. (2012). CFD modeling of a radiator axial fan for air flow distribution. World Academy of Science, Engineering and Technology, Vol:6.
- [7] Kumawat, H. (2014). Modeling and simulation of axial fan using CFD. World Academy of Science, Engineering and Technology, Vol:8, No:11.
- [8] Tzanos, C., Chien, T. (2002). A simple fan model for underhood thermal management analysis. 2002-01-1025. SAE International 2002.
- [9] Yang, L. (2002). Use of experimental data to generate swirl velocity in the FLUENT Fan model.
- [10] Hirsch, C. (2007). *Numerical Computation of Internal and External Flows*. John Wiley & Sons Ltd. Burlington, MA.
- [11] Schlichting, H. (1979). *Boundary Layer Theory*, 7th ed, McGraw-Hill.
- [12] Mach number. (n.d.). In Wikipedia. Retrieved June 20<sup>th</sup>, 2018, from [https://en.wikipedia.org/wiki/Mach\\_number](https://en.wikipedia.org/wiki/Mach_number)
- [13] *Helix Kernel User Reference Guide*. ESI Group, 2013. London, United Kingdom.

- [14] Versteeg, H., Malalasekera, W. (1995). *An Introduction to Computational Fluid Dynamics, The Finite Volume Method*, 2nd ed. Pearson Education Ltd. Essex, England.
- [15] *CFD-ACE+ 2017.0 User Manual*. ESI Group, 2017.
- [16] *Fluent 6.3 User's Guide*. Fluent Inc.
- [17] *Elements Quick Start Guid*. Streamline Solutions LLC, 2016. Indianapolis, IN.
- [18] *HELYX Core User's Guide*. Streamline Solutions LLC, 2017. Indianapolis, IN.
- [19] *Equations for a Moving Reference Frame*. SAS IP, Inc.

## VITA AUCTORIS

NAME: Sitong Ye

PLACE OF BIRTH: Jilin, China

YEAR OF BIRTH: 1992

EDUCATION: Columbia International College, Hamilton, ON,  
2011

University of Windsor, B.Sc., Windsor, ON,  
2016

University of Windsor, M.Sc., Windsor, ON,  
2018

Politecnico di Torino, M.Sc., Torino, Italy,  
2018